UNIVERSITY OF OKLAHOMA

GRADUATE COLLEGE

HYSTERESIS AND DYNAMIC EFFECTS IN THE RELATIONSHIP BETWEEN CAPILLARY PRESSURE, SATURATION, AND AIR-WATER INTERFACIAL AREA IN POROUS MEDIA

A DISSERTATION

SUBMITTED TO THE GRADUATE FACULTY

in partial fulfillment of the requirements for the

degree of

Doctor of Philosophy

By

LIXIA CHEN

Norman, Oklahoma

2006

Downloaded from SHAREOK. Persistent Handle URL: https://hdl.handle.net/11244/1048

UMI Number: 3215291



UMI Microform 3215291

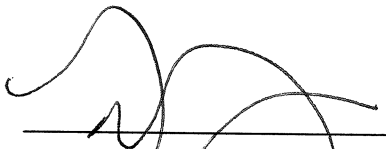
Copyright 2006 by ProQuest Information and Learning Company.
All rights reserved. This microform edition is protected against
unauthorized copying under Title 17, United States Code.

ProQuest Information and Learning Company
300 North Zeeb Road
P.O. Box 1346
Ann Arbor, MI 48106-1346

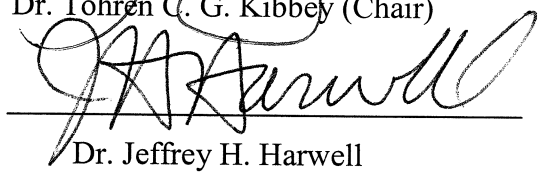
HYSTERESIS AND DYNAMIC EFFECTS IN THE RELATIONSHIP BETWEEN CAPILLARY PRESSURE, SATURATION, AND AIR-WATER INTERFACIAL AREA IN POROUS MEDIA

A DISSERTATION APPROVED FOR THE
SCHOOL OF CIVIL ENGINEERING AND ENVIRONMENTAL SCIENCE

BY



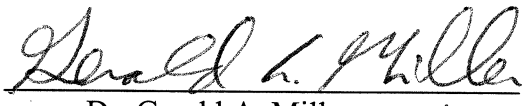
Dr. Tohren C. G. Kibbey (Chair)



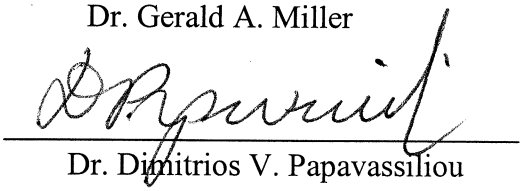
Dr. Jeffrey H. Harwell



Dr. Randall L. Kolar



Dr. Gerald A. Miller



Dr. Dimitrios V. Papavassiliou

© Copyright by LIXIA CHEN 2006
All Rights Reserved.

ACKNOWLEDGEMENTS

First of all, I must thank God, my creator, for His perfect plan and timing for me.

I cordially thank my advisor, Dr. Tohren C. G. Kibbey, for everything he did for me throughout my study. I am very grateful to him for the continuous confidence and trust he has shown in me over the last three years since before I joined his research group. I must also thank him for his numerous good ideas and constructive insights, for always being there to help, for his patience and time with my writing, and for financial support. His constant optimism and enthusiasm in research no matter results were good or bad deeply impressed me, and substantially influenced my attitude to both research and life.

I sincerely thank my doctoral committee, Drs. Jeffrey H. Harwell, Randall L. Kolar, Gerald A. Miller, and Dimitrios V. Papavassiliou, for their time and their interest in my research. Their comments and suggestions are most helpful and invaluable upon the completion of this dissertation.

A special thank is given to Dr. Nopawan Ratasuk. Without her friendship and understanding, it would be much harder for me to survive the early years in my PhD study. I must also thank her for encouraging me to make a decision that changed my life positively. I also thank my teacher, Dr. Rengao Song, and my friend, Dr. Yongsheng Chen, for helping and encouraging me to come to the US to pursue my PhD degree.

With a heart full of gratitude, I thank my mother, Shuying Wu, and my entire family back in China, for their never-faded love and encouragement throughout my life.

At last, but not at least, I thank my husband, Junjie Wu, and my daughter, Tiannan Wu, for their unconditional love that makes the stressful life more enjoyable. Without their constant support and understanding, I wouldn't be able to work over hours and my life as a PhD student would be years from completion.

TABLE OF CONTENTS

Acknowledgements ……iv

List of Figures …….. viii

List of Tables ……..…xiv

Abstract ……..xv

Chapter

1. Introduction ……....1

2. Measurement of Capillary Pressure-Saturation Relationships ……..…….5
2.1. Introduction ……..…...5
2.1.1. Capillary Pressure-Saturation Relationships of Porous Media …...5
2.1.2. Measurement of Hysteretic P_c-S Relationships ……...7
2.1.3. Objective……12
2.2. Description of the System.……13
2.3. Materials and Methods.……17
2.3.1. Materials……..17
2.3.2. Experimental Procedures……18
2.3.3. Measurement of Detailed Hysteretic P_c-S Relationships……19
2.4. Results and Discussion.……20
2.4.1. P_c-S Relationships of Sand Samples ……..21
2.4.2. P_c-S Relationships of Silt Samples……..25
2.5. Conclusions……30

3. Hysteresis in Dynamic Effects in Capillary Pressure-Saturation Relationships and Unsaturated Flow.……32
3.1. Introduction……32
3.1.1. Determination of Hydraulic Conductivity in Unsaturated Porous Media……...32
3.1.2. Determination of Dynamic Capillary Effects……..36
3.1.3. Objective……..37
3.2. Materials and Methods.……38
3.2.1. Materials……..38
3.2.2. Quantification of Dynamic Effects.……38
3.2.3. Experimental Measurement of Apparent Dynamic P_c-S Curves…44
3.2.4. Determination of the Pore Size Distribution Index (l)……...45
3.2.5. Determination of Apparent Dynamic Coefficient (t^*)……46
3.3. Results and Discussion……....47
3.3.1. Measured Apparent Dynamic and Predicted Static P_c-S curves ……47

3.3.2. Apparent Dynamic Coefficient (t^*) Calculated from P_c^{d*}-S curves ……52
3.3.3. Relative Permeability ……58
3.3.4. Hysteresis in Dynamic Capillary Effects ……64
3.4. Conclusions……67

4. Dependence of Dynamic Effects on Porous Media Properties……69
4.1. Introduction……69
4.2. Materials and Methods ……70
4.2.1. Materials ……70
4.2.2. Determination of Dynamic Coefficients……74
4.3. Results and Discussion……75
4.3.1. Primary Drainage Dynamic Coefficients of Different Porous Media……75
4.3.2. Main Imbibition Dynamic Coefficients of F-95 and F-110……85
4.3.3. Secondary Drainage Dynamic Coefficients of Different Porous Media……90
4.3.4. Estimation of Dynamic Capillary Coefficient (t) from Porous Media Properties ……98
4.4. Conclusions……104

5. Three Dimensional Capillary Pressure-Saturation-Interfacial Area (P_c-S-A) Relationships: Measurement and Hysteresis ……106
5.1. Introduction……106
5.1.1. Relationships between Interfacial Area and Saturation……108
5.1.2. Experimental Measurements of Interfacial Area……109
5.1.3. General Limitations of Current Experimental Techniques……112
5.1.4. Objectives ……114
5.2. Materials and Experimental Methods ……114
5.2.1. Materials ……114
5.2.2. Experimental Measurement of Interfacial Area ……116
5.3. Area Calculation ……120
5.3.1. Surface Excess at the Fluid-Fluid Interface……120
5.3.2. Air-Water Interfacial Tension Measurement ……121
5.3.3. UV Spectrum Fitting ……123
5.3.4. Calculation of Interfacial Area ……124
5.4. Results and Discussion ……126
5.4.1. Influence of the Rate of Pressure Change on the Measured Air-Water Interfacial Area ……126
5.4.2. Capillary Pressure, Saturation and Air-Water Interfacial Area Relationships Measured During Primary Drainage: Influence of SOBS Concentration ……128
5.4.3. Air-Water Interfacial Areas Measured for Different Porous Media during Primary Drainage ……132

5.4.4. Capillary Pressure, Saturation and Air-Water Interfacial Area Relationships: Influence of Drying/Wetting History……..134
5.4.5. Capillary Pressure, Saturation and Air-Water Interfacial Area Relationships: Influence of Surfactant-Induced Interfacial Tension Variations ……138
5.5. Conclusions……..142

6. Conclusions……..144
6.1. Conclusions ……144
6.1.1. Hysteresis in Dynamic Effects and the Influence of Porous Media Properties…….144
6.1.2. Hysteresis in the Measured Capillary Pressure-Saturation-Interfacial Area Relationships ……..146
6.2. Recommendations for Future Work ……148

References …….150

LIST OF FIGURES

Figure 2.1. A typical hysteretic capillary pressure-saturation (P_c-S) relationship……..6

Figure 2.2. Cut-away side view of the structure of the pressure cell used in the P_c-S device, with dimensions shown in cm (adapted from Salehzadeh and Demond [1999]) ……13

Figure 2.3. Experimental apparatus for the measurement of the P_c-S relationship. Six of the devices shown share a single gas cylinder and are operated in parallel……..….15

Figure 2.4. Measured slow dynamic (pseudo-static) gas-water P_c-S relationship for F-95 fine sand……..22

Figure 2.5. Measured slow dynamic (pseudo-static) gas-water P_c-S relationships for F-95 sand with scanning loops centered at high (A) and low (B) saturations…….23

Figure 2.6. Measured gas-water P_c-S relationships for F-110 ultra-fine sand. Lines correspond to slow dynamic (pseudo-static) measurements. Symbols correspond to two static primary drainage curves. Solid symbols indicate gas diffusion in static runs…..24

Figure 2.7. Measured slow dynamic (pseudo-static) gas-water P_c-S relationships for CRA 200-PAN silt. (A) Measured with Nanopure water, illustrating membrane clogging due to fines dispersion, and (B) measured with 0.01 M $CaCl_2$ solution to reduce fines ……27

Figure 2.8. Measured gas-water P_c-S relationships for SCS-250 (A), and SCS-125 (B). Lines in both figures correspond to slow dynamic (pseudo-static) measurements. Symbols in (A) correspond to two static primary drainage curves…….29

Figure 3.1. Brooks-Corey fit to the measured pseudo-static primary drainage P_c-S curve of F-95 sand. Gray symbols: measured curves; black lines: best fit results ……..45

Figure 3.2. Primary drainage P_c-S curves of F-95 sand. Solid black lines: apparent dynamic curves measured at different pressure rates(0.42, 0.21, 0.14, 0.105, 0.084, 0.07, 0.052 and 0.042 cm water per second from top to bottom curves, respectively); gray symbols: predicted static curve; dotted black lines: standard error of static P_c when predicted from linear regression at each saturation ……48

Figure 3.3. Main imbibition P_c-S curves of F-95 sand. Solid black lines: apparent dynamic imbibition curves measured at different pressure rates (0.035, 0.105, 0.117, 0.131, 0.15, 0.175, 0.21, 0.263, 0.35, 0.525, 1.05 cm water per second from top to bottom curves, respectively) with preceding drainage curves measured under constant pseudo-

static conditions; gray symbols: predicted static curve; dotted black lines: standard error of static P_c when predicted from linear regression at each saturation …….50

Figure 3.4. Secondary drainage P_c-S curves of F-95 sand. Solid black lines: apparent dynamic curves measured at different pressure rates (0.42, 0.21, 0.14, 0.105, 0.084, 0.07, 0.052 and 0.042 cm water per second from top to bottom curves, respectively); gray symbols: predicted static curve; dotted black lines: standard error of static P_c when predicted from linear regression at each saturation …….51

Figure 3.5. The relationship between apparent dynamic coefficient and water effective saturation for primary drainage of F-95 sand. Gray symbols: measured value; dotted black lines: standard error of the measured value from linear regression at each saturation; solid black line: power function fit result ……..53

Figure 3.6. The relationship between apparent dynamic coefficient and water effective saturation for main imbibition of F-95 sand. Gray symbols: measured value; dotted black lines: standard error of the measured value from linear regression at each saturation; solid black line: power function fit result ……54

Figure 3.7. The relationship between apparent dynamic coefficient and water effective saturation for secondary drainage of F-95 sand. Gray symbols: measured value; dotted black lines: standard error of the measured value from linear regression at each saturation; solid black line: power function fit result …….55

Figure 3.8. Comparison of the measured apparent dynamic coefficients for primary drainage, main imbibition and secondary drainage of F-95 sand ……..56

Figure 3.9. Water relative permeability of F-95 as a function of saturation. Dark gray: Brooks-Corey function; light gray: calculated at t = 0 for primary drainage ……59

Figure 3.10. Water relative permeability of F-95 as a function of saturation. Dark gray: Brooks-Corey function; light gray: calculated at t = 0 for main imbibition ……..61

Figure 3.11. Water relative permeability of F-95 as a function of saturation. Dark gray: Brooks-Corey function; light gray: calculated at t = 0 for secondary drainage …….62

Figure 3.12. Comparison of the $k_{rw}^{t=0}$ –S_e curves obtained for primary drainage (light gray circle), main imbibition (light gray triangle), and secondary drainage (dark gray square), along with Brooks-Corey k_{rw} function (black line)……63

Figure 3.13. Comparison of the relationships between dynamic capillary coefficient and water saturation estimated for primary (square) and secondary (circle) drainages of F-95 sand……..65

Figure 4.1. Brooks-Corey fit to the measured pseudo-static primary drainage P_c-S curves of different porous media. Gray symbols: measured curves; black lines: fit results. Data for F-95 are re-plotted from Figure 3.1 for comparison. Fit parameters in Brooks-Corey equation are listed in Table 4.1 ……..73

Figure 4.2. Primary drainage P_c-S curves of F-110 sand. Solid black lines: apparent dynamic curves measured at different pressure rates (0.42, 0.21, 0.084, 0.042, 0.0168, and 0.0084 cm water/sec from top to bottom curves, respectively); empty black square on each dynamic curve: lowest saturation used in calculation; dark gray symbols: predicted static curve; dotted black lines: standard error of the predicted static P_c from linear regression; light gray symbols: independently measured static P_c (re-plotted from Figure 2.6)……..76

Figure 4.3. Primary drainage P_c-S curves of SCS-250 silt. Solid black lines: apparent dynamic curves measured at different pressure rates (0.84, 0.21, 0.105, 0.088, 0.084, 0.070, 0.052 and 0.042 cm water/sec, respectively); dark gray symbols: predicted static curve; dotted black lines: standard error of the predicted static P_c from linear regression; light gray symbols: independently measured static P_c (re-plotted from Figure 2.8A) …….77

Figure 4.4. The relationship between apparent dynamic coefficient and water effective saturation for primary drainage of different porous media. Gray circles: measured values; solid black lines: power function fit results; dotted black lines: standard error of the measured value from linear regression at each saturation. For clarity, experimental data for F-110 is re-plotted in Fig. B along with power function fit and standard error….79

Figure 4.5. Water relative permeability of F-110 as a function of saturation. Dark gray: Brooks-Corey function; light gray: calculated at t = 0 for primary drainage ……..80

Figure 4.6. Water relative permeability of SCS-250 as a function of saturation. Dark gray: Brooks-Corey function; light gray: calculated at t = 0 for primary drainage ….81

Figure 4.7. Comparison of water relative permeability functions of different porous media. Lines: Brooks-Corey function; symbols: calculated at t = 0 for primary drainage; light gray: F-95 sand; dark gray: F-110 sand; black: SCS-250 silt. Note that Brooks-Corey functions for F-95 and F-110 overlay each other …….82

Figure 4.8. Comparison of dynamic capillary coefficients determined for F-95 (light gray), F-110 (dark gray) and SCS-250 (black) during primary drainage ……83

Figure 4.9. Main imbibition P_c-S curves of F-110 sand. Solid black lines: apparent dynamic imbibition curves measured at different pressure rates (0.035, 0.117, 0.131, 0.15, 0.175, 0.21, 0.263, 0.35, 1.05 cm water per second from top to bottom curves, respectively) with preceding drainage curves measured under constant pseudo-static conditions; gray symbols: predicted static curve; dotted black lines: standard error of static P_c when predicted from linear regression at each saturation…….86

Figure 4.10. The relationship between apparent dynamic coefficient and water effective saturation for main imbibition of F-95 and F-110 sands. Gray symbols: measured values; solid black line: power function fit result; dotted black lines: standard error of the measured dynamic coefficient from linear regression at each saturation……87

Figure 4.11. Comparison of water relative permeability functions of different porous media. Lines: Brooks-Corey function; symbols: calculated at t = 0 for main imbibition; light gray: F-95 sand; dark gray: F-110 sand. Note that Brooks-Corey functions for F-95 and F-110 overlay each other……..89

Figure 4.12. Secondary drainage P_c-S curves of F-110 sand. Solid black lines: apparent dynamic curves measured at different pressure rates (0.84, 0.21, 0.105, 0.088, 0.084, 0.070, 0.052 and 0.042 cm water/sec, respectively); dark gray symbols: predicted static curve; dotted black lines: standard error of the predicted static P_c from linear regression …….90

Figure 4.13. Secondary drainage P_c-S curves of SCS-250 silt. Solid black lines: apparent dynamic curves measured at different pressure rates (0.21, 0.14, 0.105, and 0.070 cm water/sec, respectively); dark gray symbols: predicted static curve; dotted black lines: standard error of the predicted static P_c from linear regression …….91

Figure 4.14. The relationship between apparent dynamic coefficient and water effective saturation for secondary drainage of different porous media. Gray symbols: measured values; solid black lines: power function fit results; dotted black lines: standard error of the measured dynamic coefficient from linear regression at each saturation ……92

Figure 4.15. Water relative permeability of F-110 sand as a function of saturation. Dark gray: Brooks-Corey function; light gray: calculated at t = 0 for secondary drainage …….94

Figure 4.16. Water relative permeability of SCS-250 silt as a function of saturation. Dark gray: Brooks-Corey function; light gray: calculated at t = 0 for secondary drainage …….94

Figure 4.17. Comparison of water relative permeability functions of different porous media. Lines: Brooks-Corey function; symbols: calculated at t = 0 for secondary drainage; light gray: F-95 sand; dark gray: F-110 sand; black: SCS-250 silt. Note that Brooks-Corey functions for F-95 and F-110 overlay each other ……..95

Figure 4.18. Comparison of dynamic capillary coefficients determined for F-95 (light gray), F-110 (dark gray), and SCS-250 (black) during secondary drainage……..97

Figure 4.19. Secondary drainage t^*-S_e curves of different porous media scaled to the Stauffer equation. Light gray: F-95 sand; dark gray: F-110 sand; black: SCS-250 silt ……101

Figure 4.20. The plot of $t^* \times K_{SAT}$ versus S_e showing the similar intercept of the curves for different porous media during a particular drainage or imbibition. The black dotted line in each figure shows the estimated intercept (B) applicable for different porous media during a particular drainage or imbibition. Light gray: F-95; dark gray: F-110; black: SCS-250……..……102

Figure 5.1. Proposed relationships between interfacial area (*A*) and water saturation (*S*) when water films adsorbed to grains are ignored (a) or considered (b)……108

Figure 5.2. Schematic diagram of the experimental apparatus used for the simultaneous measurement of capillary pressure (P_c), saturation (*S*), and air-water interfacial area (*A*). For organic liquid-water interfacial area measurements, an organic liquid reservoir is placed in line before the pressure cell…….117

Figure 5.3. Air-water interfacial tension (solid circle: experimental data; solid line: fit from the Szyszkowski equation) and surface excess (dashed line) of SOBS in 0.1 M NaCl solution as a function of SOBS activity……..122

Figure 5.4. Influence of the rate of pressure change on the interfacial area measured for F-110 sand during primary drainage at two different SOBS concentrations (50 and 500 mg/L)……127

Figure 5.5. Influence of SOBS concentration (A: 50; B: 100; C: 200; D: 400; and E: 500 mg/L) on P_c-*S* (a), *A*-*S* (b), and *A*-P_c (c) relationships of F-110 sand measured during primary drainage……..129

Figure 5.6. Air-water interfacial areas measured for different porous media during primary drainage……..133

Figure 5.7. P_c-*S*-*A* relationships of F-110 sand showing the influence of drying/wetting history under conditions of minimal interfacial tension variation (5 mN/m over the course of the experiment). A: primary drainage; B: main imbibition; C: secondary drainage; D: scanning imbibition; E: scanning drainage. Note that interfacial areas are only measured during drainage…….135

Figure 5.8. P_c-*S*-*A* relationships of F-110 sand corresponding to a 25 mN/m variation in interfacial tension during main imbibition. 0.1 M NaCl was used for primary drainage and 500 mg/L SOBS for main imbibition. A: primary drainage; B: main imbibition; C:

secondary drainage; D: scanning imbibition; E: scanning drainage. Note that interfacial areas are only measured during secondary and scanning drainages…….140

Figure 5.9. Effect of interfacial tension variations on *A*-*S* curves for secondary (A) and scanning (B) drainages. Solid lines: 5 mN/m variation; dashed lines: 25 mN/m variation ……..….141

LIST OF TABLES

Table 2.1. Properties of Soils and Water Wet Membranes and Run Conditions Used …18

Table 3.1. Parameters Used in Dynamic Coefficients Calculation for F-95 Sand ……...43

Table 4.1. Properties of Porous Media ……..71

Table 4.2. Comparison of Dynamic Capillary Coefficients Estimated from the Stauffer Equation and from the Described Experiments ……99

Table 4.3. Intercept (B) for the Plots of $t^* \times K_{SAT}$ versus S_e and t values Estimated from Equation (4.2) ……..……104

Table 5.1. Properties of Porous Media Used in Air-Water Interfacial Area Measurements …….115

Table 5.2. Comparison of Specific Surface Areas (cm^2/g) of Different Porous Media between the Values Estimated from Extrapolating *A-S* Curves and the Values Estimated from Log-Norman Fit to Grain Size Distributions……..133

ABSTRACT

This work experimentally examines two unsaturated phenomena of porous media that influence the transport and distribution of contaminants in the subsurface. The first is dynamic effects in the response of porous media to pressure changes. Dynamic effects discussed here include both relative permeability effects which control the speed of unsaturated flow, and dynamic capillary effects which influence the hysteretic capillary pressure-saturation (P_c-S) relationship under dynamic conditions. The second unsaturated phenomenon studied here is the influence of hysteretic P_c-S relationships on the magnitude of interfacial area (A) between two immiscible fluids, a critical parameter controlling contaminant distribution, transport and mass transfer in unsaturated environments.

The apparent dynamic coefficient (t^*), a measure of combined dynamic effects, was measured for various porous media ranging from sand to silt for different drying/wetting paths. Relative permeability (k_{rw}) and the dynamic capillary coefficient (t), which measure relative permeability effects and dynamic capillary effects, respectively, were calculated from t^* with the application of Darcy's law and Brooks-Corey equations for unsaturated flow. In general, it was found that t^*, t, and k_{rw} are hysteretic throughout the hysteretic P_c-S relationship, and vary as a function of saturation. It was further found that at a particular saturation, t^* and t of different porous media are inversely proportional to the saturated conductivity. Results also show that for each drainage or imbibition process, the unsaturated flow is dominated by relative

permeability effects at low saturations, and by dynamic capillary effects at high saturations.

Air-water interfacial areas (A) were measured for multiple drainages (primary, secondary, and scanning) using a newly developed method, along hysteretic P_c-S curves representing natural drying/wetting processes. The measurement was conducted under a condition with relatively constant interfacial tension throughout experiments, making use of an isomerically pure anionic surfactant as interfacial tracer. Langmuir and Gibbs adsorption equations were applied in area calculations. A 3D P_c-S-A relationship established for a fine sand shows a hysteretic nature, based on the observation that neither A is a unique function of P_c and S nor P_c is a unique function of S and A. It was also found that A increases monotonically with decreasing saturation, with higher A values observed for secondary and scanning drainages than primary drainage, and also for finer media than coarser media at a particular saturation. In an area measurement specifically designed to study the influence of surfactant-induced interfacial tension variations, approximately two times more interfacial area was observed for a 25 mN/m interfacial tension change, in comparison with a system with relatively constant interfacial tension. Environmental implications of the results found here are discussed.

Chapter 1

Introduction

The dynamic and static behaviors of fluids in unsaturated porous media have important practical implications for many applications. Both the redistribution of fluids under dynamic conditions and the formation of interfaces between fluids are important phenomena in understanding the behavior of contaminants in subsurface. These two phenomena form the basis of the research described here.

The first objective of this work is to study hysteresis in the relationship between capillary pressure (P_c), saturation (S) and air-water interfacial area (A) in unsaturated porous media. The fluid-fluid interface in porous media not only plays an important role in many physical and chemical processes, such as multiphase flow, dissolution, volatilization, interfacial adsorption and accumulation [Miller, *et al*., 1990; Imhoff, *et al*., 1993; Brusseau, *et al*., 1997; Bradford and Leij, 1997; Kim *et al*., 1998], but also determines the feasibility of technologies to remediate nonaqueous phase liquid (NAPL)–contamination in the subsurface, such as soil vapor extraction [Kneafsey and Hunt, 2004; Hoeg, *et al*., 2004] and pump and treat [Rubin, *et al*., 2004] methods. Air-water interface in the unsaturated zone can retard the transport of surface–active contaminants, such as organic compounds, colloids and microbes [Kim *et al*., 1998; Wan and Wilson, 1994; Sim and Chrysikopoulos, 2000]. It is widely recognized that the quantitative determination of interfacial areas is critical in understanding contaminant distribution, transport and mass transfer among immiscible phases. However, before experimental techniques started to become available in the 1990s, the estimation of interfacial areas

relied on model simulations [Gvirtzman and Roberts, 1991; Cary, 1994; Reeves and Celia, 1996; Bradford and Leij, 1997].

Interfacial area is known to be a function of saturation, but the interfacial area–saturation relationship is not expected to be unique, since numerous distributions and configurations of pore water could correspond to a particular saturation. Instead, the dependence of interfacial area on saturation is complicated by the well-known hysteresis in the capillary pressure-saturation (P_c-S) relationship, one of the fundamental hydraulic properties of porous media controlling multiphase and unsaturated flow in the subsurface. Based on a thermodynamic definition, Hassanizadeh and Gray [1993] proposed that besides saturation (S), interfacial area (A) between wetting and non-wetting phases is another important independent variable determining the magnitude of capillary pressure (P_c), and the hysteresis observed in the P_c-S curve is only a projection of a unique three-dimensional P_c-S-A surface. As such, whether the P_c-S-A relationship is hysteretic or not is of theoretical interest to better understand behaviors of environmental processes associated with fluid-fluid interfaces, and it is also the driving question of the research described here.

To date, the hysteresis in P_c-S-A relationships has been investigated using pore network modeling, showing the unique dependence of interfacial area on capillary pressure and saturation, while non-unique dependence of capillary pressure on saturation and interfacial area [Reeves and Celia, 1996; Held and Celia, 2001]. More recently, researchers have found a non-hysteretic P_c-S-A relationship for a nitrogen-decane system in 2D micro-model, finding that any one of the three parameters is a unique function of the other two [Cheng, *et al*., 2004]. However, due to practical difficulties in the

laboratory, experimental evidence showing the hysteresis or non-hysteresis of P_c-S-A relationships of natural porous media has not been reported. As such, this research will use a newly developed technique to experimentally study the hysteresis in P_c-S-A relationships in the air-water system of natural porous media. The research will focus on measuring the air-water interfacial area generated from multiple drainage processes involved in hysteretic P_c-S relationships for an ultra fine sand.

The second objective of this research is to study hysteresis in the dynamic response of porous media to drainage and imbibition. When dynamic pressure changes occur, the movement of fluids and formation of interface in a porous medium may depend on both the rate of saturation change and the drying/wetting history. Two main effects control the dynamic response of porous media to pressure change in unsaturated flow. The first is the effect of relative permeability (or unsaturated conductivity). The second is the effect of capillary pressure rate dependence (known as dynamic capillary effect). The measurement and modeling analysis of hydraulic conductivities of porous media have been the subject of numerous studies for a long time [e.g. Brooks and Corey, 1966; Klute and Dirksen, 1986; Eching, *et al*., 1994; Butters and Duchateau, 2002]. It is widely known that the hydraulic conductivity is a nonlinear function of saturation, but whether the conductivity is hysteretic or not during drainage and imbibition remains unclear. For the dynamic capillary pressure effects, a parameter called the dynamic capillary coefficient (t) has been developed to describe the speed of saturation change in response to capillary pressure change. The dynamic capillary coefficient has been proposed to be a function of saturation, and to have a hysteretic nature [Hassanizadeh, *et al*., 2002]. Recent modeling analyses have shown the necessity to include dynamic

capillary effects to better understand multiphase and unsaturated flow [*e.g*. Beliaev, 2003; O'Carroll *et al*., 2005]. However, to date, experimental work determining the quantitative dependence of the dynamic capillary coefficient, t, on saturation and the possible hysteretic nature of t itself has not been reported. As such, the work described here will study the hysteresis of dynamic effects, including both relative permeability and dynamic capillary effects, in the P_c-S relationships of porous media. Dynamic effects will be experimentally determined as a function of saturation during drainage and imbibition for various porous media in air-water system. Results from this work will provide a new and valuable insight in evaluating the influence of the dynamic change of environmental conditions on unsaturated and transient flow behavior of a wide range of natural porous media.

Chapter 2

Measurement of Capillary Pressure-Saturation Relationships

2.1. INTRODUCTION

2.1.1. *Capillary Pressure-Saturation Relationships of Porous Media*

The capillary pressure-saturation (P_c-S) relationship, also known as the capillary pressure function or water retention function, is one of the fundamental hydraulic properties of porous media controlling multiphase and unsaturated flow in the subsurface. Capillary pressure (P_c) is a function of the pore size distribution of the porous material, the interfacial tension (g) across wetting and non-wetting phases, and the contact angle (q) between the fluid/fluid interface and porous material surface. At equilibrium, P_c is defined as the pressure difference between the wetting phase (P_w) and non-wetting phase (P_n) in a porous medium.

In a porous medium, capillary pressure is a hysteretic function of saturation (S), where saturation is defined as the ratio of wetting phase volume (V_w) relative to total void volume (V_v) in the medium (*i.e.*, $S = V_w/V_v$). A typical P_c-S relationship of a porous medium initially saturated with water ($S = 1$) is shown in Figure 2.1. Hysteresis in the P_c-S relationship means that at a given capillary pressure, a porous medium being drained has a higher saturation than the same medium undergoing imbibition. Many factors are believed to be responsible for hysteresis in the P_c-S relationship, including contact angle hysteresis, pore geometry, and pore surface roughness [Bear, 1972; Morrow, 1976; Anderson, 1987]. As shown in Figure 1, as P_c is gradually increased from zero, the

observed behavior follows the primary drainage curve until the residual wetting phase saturation (S_{wr}) is reached. If P_c is then decreased again to zero, the observed behavior follows the main imbibition curve until the natural wetting phase saturation (S_{nwr}) is obtained. The natural wetting phase saturation is typically in the range of 0.8 to 0.9 due to the existence of entrapped non-wetting phase [Klute, 1986]. Scanning curves define points bounded by the primary drainage and main imbibition curves, and can be obtained by reversing the applied capillary pressure at any point along the P_c-S relationship. Secondary drainage and main imbibition together is often referred to as the main hysteresis loop.

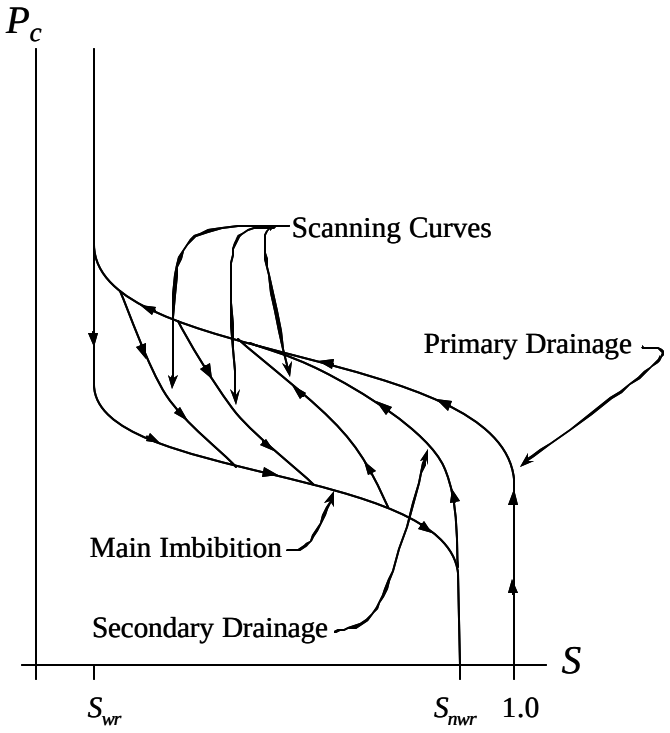


Figure 2.1. A typical hysteretic capillary pressure-saturation (P_c-S) relationship.

2.1.2. *Measurement of Hysteretic P_c-S Relationships*

Numerous techniques have been designed and used to measure P_c-S relationships of porous media, but few have been used for measurements beyond primary drainage and/or main imbibition. As such, the availability of detailed hysteretic experimental data is very limited. There are three main challenges involved in the design of a practical P_c-S measurement device for hysteretic measurements: 1. The device must be able to accurately measure saturation at each applied capillary pressure without requiring samples to be disturbed or sacrificed; 2. the capillary barriers used in the device must be able to keep each phase (wetting, non-wetting) from crossing the opposite phase boundary of the sample, while supporting the porous medium under the applied capillary pressures; and 3. the device must be able to complete measurements on a reasonable time scale.

Static Measurements. In static P_c-S measurements, the saturation of each data point is determined after the porous medium is fully equilibrated at the applied capillary pressure. Methods designed for P_c-S measurement generally fall into two groups: suction methods and pressure methods.

In suction methods, which are among the oldest methods, wet soil is open to the air (at atmospheric pressure) and a negative gauge pressure (suction) is applied to soil water. Using suction methods, P_c-S relationships can be measured by tensiometers or suction plates. Tensiometers directly determine the negative pore-water pressure by measuring suction the porous medium applies across a water-wet capillary barrier on fluid contained within the tensiometer [Richards, 1928; Miller, 1951; Leonard and Low,

1962; Corey and Brooks, 1975; Fredlund and Rahardjo, 1993]. In tensiometer-based methods, water content is usually determined by weight, producing a single P_c-S data point for each measurement. In suction plate methods, water pressure is controlled by an applied vacuum [Gardner, *et al*., 1922; Richards, 1928; Leamer and Shaw, 1941; Richards and Weaver, 1944; Jamison and Reed, 1949; Puri, 1949; Morrow and Harris, 1965; White, *et al*., 1972; Su and Brooks, 1980]. Suction plate methods can be used to measure a series of P_c-S data points by successively adjusting the soil water pressure. Water saturation at each pressure can be determined by weight loss from drying the soil or by tracking the amount of water pulled out of soil due to suction.

One limitation associated with suction methods is that the absolute pressure of the wetting phase cannot be lower than its vapor pressure, or cavitation will occur [Klute 1986]. In addition, regardless of the fluids used, suction methods cannot be used for capillary pressures higher than 1 atm (101 kPa; 1030 cm water), because that would require a negative absolute pressure in the wetting phase.

Pressure methods avoid these problems by raising the non-wetting phase pressure, allowing for greater differences in pressure between phases without cavitation. In pressure methods, pressure is applied to the non-wetting phase while the wetting phase is typically kept at or near atmospheric pressure. Compared to suction methods, which directly measure the negative wetting phase pressure, pressure methods translate both the wetting and non-wetting phase pressures to higher values, preventing cavitation (since the absolute pressure in the wetting phase does not have to be reduced). As such, pressure methods are also called axis translation methods [Fredlund and Rahardjo, 1993]. In pressure methods, the maximum capillary pressure that can be applied to the system is

determined by the air entry pressure of the water-wet capillary barrier, which prevents air from leaving the porous medium through the water-wet boundary.

Cells used for P_c-S measurement with pressure methods typically consist of a soil chamber and two caps holding the chamber tightly at the top and bottom. High gas pressure is usually introduced into the sample from the top (or side) of the chamber, and bulk water is connected to soil water through a fully saturated capillary barrier at the bottom (or opposite side) of the chamber. Based on modified ultrafiltration equipment [Woodruff, 1940], Richards and his colleagues designed pressure cells specifically for working with soil that could be applied to capillary pressures as high as 16 atm (1621 kPa). The cells made use of cellophane membranes [Richards, 1941; Reitemeier and Richards, 1944] or porous ceramic plates [Richards and Fireman, 1943; Richards and Weaver, 1944] as water-wet gas phase capillary barriers. One major advance in pressure methods since the earliest designs has been the application of membranes with higher water permeability [Elrick and Bowman, 1964], or higher air diffusion resistance [Coleman and Marsh, 1961]. With the use of cellulose membranes, Coleman and Marsh [1961] constructed pressure cells that could be operated up to 1460 atm (1.5×10^5 kPa). However, gas diffusion through capillary barriers was a common problem with applications at high pressure. Although techniques were developed to remove bubbles forming from gas passing through membranes or porous plates to avoid gas accumulation [Richards and Fireman, 1943; Tanner and Elrick 1958; Coleman and Marsh, 1961], the continuity between soil water and bulk water in the measuring system can be compromised, and imbibition may be impeded due to the blockage of the water supply. In addition, the accumulation of gas under the capillary barrier introduces errors in

measuring liquid volume drained out or imbibed into soil, and water saturation must be determined by weighing the sample once equilibrated at each applied pressure.

Because opening cells and taking samples during experiments for weighing can disturb the hydraulic contact between testing material and capillary barrier, Reginato and van Bavel [1962] developed a weighable pressure cell, known as the Tempe cell. The Tempe cell makes use of a porous plate as a gas phase capillary barrier that can be operated between 0 to 1 atm (101 kPa). The Tempe cell is widely used by current researchers [Fredlund and Rahardjo, 1993; Powers and Tamblin, 1995; Lord *et al*., 1997; She and Sleep, 1998] and a number of models are commercially available. During measurement with a Tempe cell, the cell must be detached from the system and weighed after it is equilibrated at each applied pressure. Water content is then calculated by weight change at each step combined with either known original saturation of sample before experiment, or residual saturation measured by drying the sample after the highest capillary pressure is applied. A complication with the Tempe cell is that repeated disconnections may be needed to determine the achievement of equilibrium, so air bubbles can be introduced into the system below the porous plate.

The pressure cell developed by Klute [1986] is another device that has been widely used and modified by researchers to meet specific needs (e.g. [Demond and Roberts, 1991; Fredlund and Rahardjo, 1993]). The apparatus, which is also called a pressure plate extractor, is designed to analyze multiple soil samples at the same time at capillary pressure up to 15 atm (1520 kPa) with the use of an appropriate porous ceramic plate. Water saturation is measured by weight when equilibration is presumably achieved

at each applied pressure (samples are weighed, and then dried and re-weighed to determine water content.)

More recently, researchers have modified pressure cells by adding a hydrophobic wetting phase capillary barrier, which is permeable to gas or organic liquid but impermeable to water, between the porous medium and the pressurized bulk non-wetting phase [Powers and Tamblin, 1995; She and Sleep, 1998; Salehzadeh and Demond, 1999]. With this modification, the porous medium fully occupies the soil chamber with a known volume, and tightly contacts the non-wetting phase capillary barrier under the soil. The application of a hydrophobic membrane is especially important to study the wetting process (imbibition), because it allows more accurate saturation measurements by preventing wetting phase from flooding the porous medium and pooling above it.

One general disadvantage of static measurements is the long duration required for experiments. The equilibration time at each applied pressure depends on the conductivities of both soil and non-wetting phase capillary barrier in use, and the height of sample [Reginato and van Bavel, 1962; Klute, 1986]. For a system using porous ceramic plate with 1 bar air-entry pressure as capillary barrier and working with a sand sample of 3 cm high and 50 to 500 μm grain size, it can take at least 24 hours to equilibrate at each increased/decreased capillary pressure step [Reginato and van Bavel, 1962; Desai, *et al*., 1992; Demond, *et al*., 1994; She and Sleep, 1998]. As a result, a complete primary drainage and main imbibition loop may take as long as 2 to 4 months to complete for a sand sample; a silt or other material with low conductivity could take much longer. Long experimental durations limit the amount of data that can be collected,

reduce reproducibility, and worsen the effects of the diffusion of the non-wetting phase through the capillary barrier.

Dynamic Measurements. Compared with static equilibrium methods, relatively few methods have been reported for making dynamic measurements of P_c-S relationships. In dynamic methods, the approach is to increase or decrease the capillary pressure at a predetermined rate (either stepwise or continuous) without waiting for equilibration between steps, as required with the existing methods for static measurements. This approach has the advantage of allowing drainage and imbibition curves to be measured rapidly [Topp, *et al*., 1967; Perroux, *et al*., 1982], with the disadvantage that it will not necessarily give a result that matches the true P_c-S relationship determined under static conditions if the rate of capillary pressure change is too great for the porous medium to drain/imbibe or the sensors to respond [Topp, *et al*., 1967; Rogers and Klute, 1971; Smiles, *et al*., 1971; Vachaud, *et al*., 1972; Wildenschild, *et al*., 2001]. If sufficiently slow rates are used for a particular porous medium, however, it is possible for dynamic methods to produce an exact match for the true P_c-S relationship.

2.1.3. *Objective*

The objective of the work described in this chapter was to develop an automated method for rapid measurement of the true hysteretic P_c-S relationships in unconsolidated porous media. The method is designed around a membrane-based pressure cell, and makes use of computer control and data acquisition to allow large quantities of data to be collected rapidly. The system can be operated in either static or dynamic modes, and is

capable of collecting data for detailed hysteretic P_c-S relationships, including scanning curves, in less than 20 hours for materials ranging from sands to silts. The device has been tested for capillary pressures up to 1000 cm water (98 kPa).

2.2. DESCRIPTION OF THE SYSTEM

The pressure cell used in this study shares the same design as the membrane-based cell developed (and described in detail) by Salehzadeh and Demond [1999]. The cell has a sample chamber with a 2.54 cm inner diameter a 1.27 cm height. The detailed structure of the cell is shown in Figure 2.2. The end caps of the cell hold capillary barrier

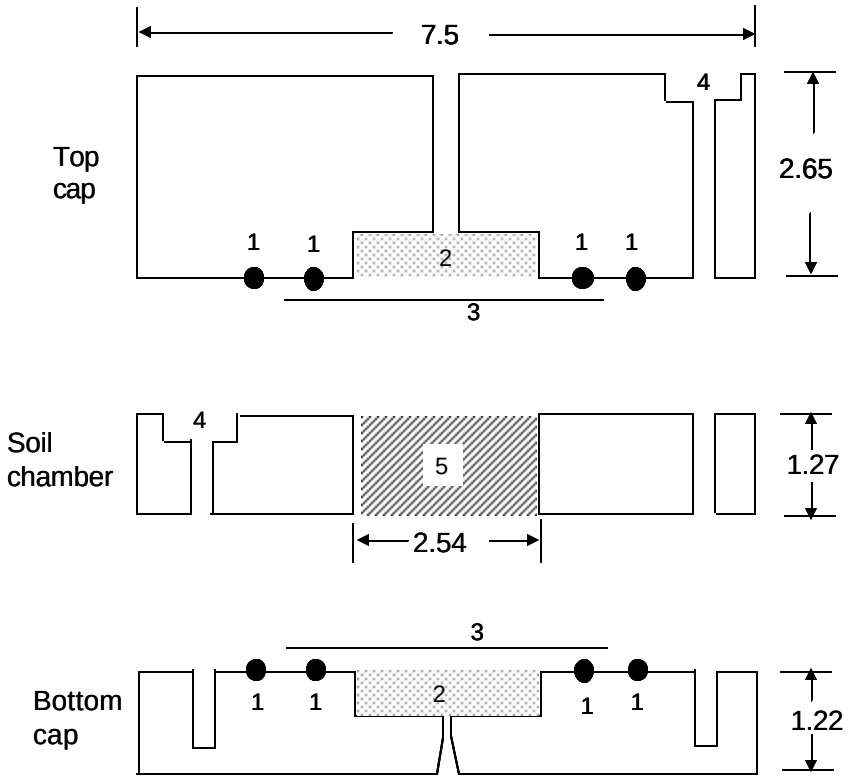


Figure 2.2. Cut-away side view of the structure of the pressure cell used in the P_c-S device, with dimensions shown in cm (adapted from Salehzadeh and Demond [1999]).

membranes in place, supported by porous stainless steel plates (20 µm pore size and 1.6 mm thickness, purchased from Mott Corp., Farmington, CT), and sealed by two O-rings at each end. One difference between the cell used in this research and the one described by Salehzadeh and Demond [1999] is in membrane selection. While Salehzadeh and Demond [1999] used 0.45 µm nylon water-wet membranes, here a wide range of pore sizes, specifically selected for the porous medium, is used. In addition, the polyvinylidene fluoride (PVDF) hydrophobic membrane used by Salehzadeh and Demond [1999] is replaced with Teflon membranes, because the PVDF membranes tended to leak after multiple drainage/imbibition cycles, especially in air/water systems. Details of specific membranes used are given in the **Materials and Methods** section.

The setup of the device is shown in Figure 2.3. Nylon tubing (6.5 mm OD × 4.5 mm ID × 3 m long) is connected to the top end of the cell to introduce the gas phase to the system. A computer-controlled 0-15 psi (0-103 kPa) servo pressure regulator (type 3110, Marsh Bellofram Corp., Newell, WV) connected to a high purity nitrogen cylinder adjusts the pressure of the gas phase applied to the pressure cell. Gas pressure is monitored with a 0-15 psi (0-103 kPa) pressure transducer (model PX181-015G5V, Omega Engineering Inc., Stamford, CT). The bottom of the cell is connected to a tee connector through grey PEEK tubing (1.6 mm OD × 1.0 mm ID, Alltech Assoc., Deerfield, IL) with a shut off valve (P-721, Upchurch Scientific, Oak Harbor, WA) to prevent water flow during initial setup. As shown in Figure 2.3, the top end of the tee is connected to a glass capillary tube (6 mm OD × 2 mm ID) which collects the wetting fluid leaving the cell during the drainage, and serves as a wetting phase reservoir during imbibition. The use of a vertical glass tube is a major modification of the device from the

one described by Salehzadeh and Demond [1999], who used a horizontal tube. The use of a vertical glass tube allows the volume of wetting fluid leaving the cell to be measured by tracking hydrostatic pressure with a high-accuracy pressure transducer (model PX 2300, Omega Engineering Inc., Stamford, CT) connected to the horizontal end of the tee (Figure 2.3). Given the inner diameter of the glass tube and the density of the wetting fluid, hydrostatic pressure changes in the glass tube can be used to determine the volume of water that has left the cell (Glass tube volumes must be measured in advance to account for diameter variability between batches of glass tubes.)

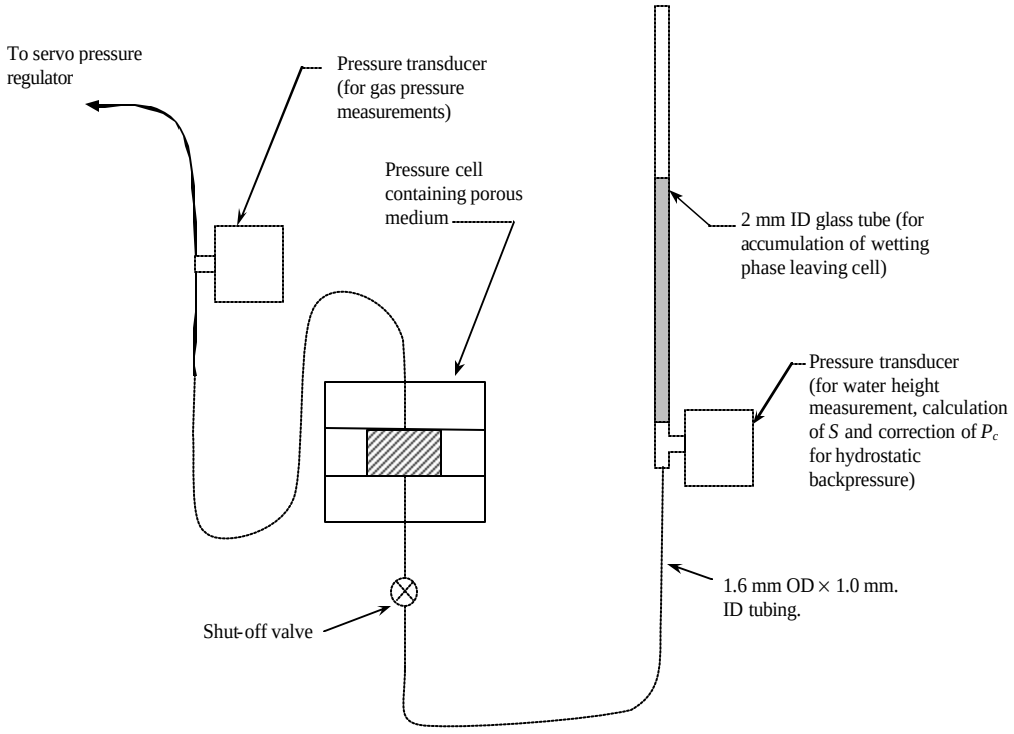


Figure 2.3. Experimental apparatus for the measurement of the P_c-S relationship. Six of the devices shown share a single gas cylinder and are operated in parallel.

Computer control of the servo pressure regulator is achieved with a Measurement Computing (Middleboro, MA) PCI-DDA08/12 8-channel D/A board. Data acquisition is achieved with a Measurement Computing PCI-DAS6034 16-channel A/D board. System control and data acquisition are conducted using custom-designed software based on the Measurement Computing Universal Library. The software was written for Windows XP using Microsoft Visual C++ with the Microsoft Foundation Classes. For all results presented here, data were smoothed during data collection by averaging 500 samples per input value at a rate of 6250 samples per second per channel (0.08 seconds per input value). Because the averaging period was much shorter than the time scale of saturation changes within the cell (seconds to minutes), the procedure reduced high frequency data acquisition system noise without distorting measured data.

The device used in this research comprises six individual systems as described above, with shared parallel computer control and acquisition, and a shared nitrogen cylinder. The parallel nature of the device allows experiments with up to six different porous media or replicate experiments to be run simultaneously. As experiments are conducted, gas pressure applied to each cell is increased or decreased individually through a pre-programmed series of steps. At each step, capillary pressure and saturation are calculated automatically, and the P_c-S curve is plotted. Although this research focuses on gas/liquid measurements, the system is also compatible with liquid/liquid applications if a vapor trap and a reservoir of non-wetting liquid are added between the servo pressure regulator and pressure cell (*e. g*. [Salehzadeh and Demond, 1999]).

2.3. MATERIALS AND METHODS

2.3.1. *Materials*

Gas-water P_c-S relationships have been measured for five different unconsolidated porous media ranging from fine sands to silts. Four of the media were received from U. S. Silica (Berkeley Springs, WV): two Ottawa foundry fine sands F-95 and F-110, and two ground silicas (crushed silicas in the silt size range) SIL-CO-SIL 250 (SCS-250) and SIL-CO-SIL 125 (SCS-125). The fifth porous medium used in this research, referred to as CRA 200-PAN in the following text, is the fraction finer than 200 mesh of a local soil from the alluvial channel of the Canadian River in Norman, Oklahoma. CRA 200-PAN is predominantly composed of quartz with approximately one third of the grains exhibiting moderate iron oxide coatings. The physical properties of these unconsolidated porous media are listed in Table 2.1. High purity nitrogen was used as non-wetting phase for all the porous media used here. Nanopure water (Nanopure Infinity, Barnstead International, Dubuque, Iowa) was used as wetting phase for sands. For silts, 0.01 M $CaCl_2$ was added to the wetting phase (0.01 M concentration) to decrease the double layer thickness around the ultra fine grains, and to consequently reduce dispersion of fines and clogging of the non-wetting phase capillary barrier.

Hydrophilic nylon membranes with various pore sizes (Osmonics Inc., Minnetonka, MN) and 0.22 µm hydrophobic Teflon membranes from the same company were used as capillary barriers for the non-wetting and wetting phases, respectively. The appropriate pore size of nylon membrane ranging from 0.1 to 20 µm was chosen depending on the type of porous media (Table 2.1), which determines the capillary

pressure needed to reach the residual saturation. The largest pore size satisfying the needed capillary pressure was used in this research to provide the most rapid response possible. Water permeability of each nylon membrane is listed in Table 2.1.

Table 2.1. Properties of Porous Media and Water Wet Membranes and Run Conditions Used.

Medium	Type[a]	Mean grain size, d_{50} [b]	Porosity [c]	Water wet capillary barrier			Displacement pressure, p^d ($cm\ H_2O$) [e]	Pressure rate, dP_n/dt ($cm\ H_2O/s$) [f]
				Pore size (μm)	Water conductivity (cm/s) [d]	Thickness (μm)		
F-95	Fine sand	140 μm	0.349 ± 0.007	20	3.344×10^{-4}	97	64	0.071
F-110	Ultra fine sand	120 μm	0.362 ± 0.006	20	3.344×10^{-4}	97	71	0.042
CRA 200-PAN	Silt	<75 μm	0.392 ± 0.021	5	7.881×10^{-5}	100	206	0.044
SCS-250	Silt	45 μm	0.413 ± 0.019	0.45	7.813×10^{-6}	122	248	0.070
SCS-125	Silt	<45 μm (d_{79} = 45 μm)	0.422 ± 0.006	0.1	1.076×10^{-6}	113	400	0.087

a: Based on the classification frequently used by sedimentologists. Source: Friedman and Sanders [1978].
b: Data provided by US Silica for all materials except CRA 200-PAN.
c: The error range is from duplicate measurements.
d: Data provided by manufacturer: Osmonics Inc.
e: Obtained from a Brooks-Corey fit to primary drainage data.
f: Rates used for slow dynamic (pseudo-static) runs shown in Figures 2.4-2.8.

2.3.2. *Experimental Procedures*

Each porous material is individually packed in the pressure cell. Before being used, each sand or silt is rinsed with wetting solution several times to reduce fines which can

clog membranes. A stainless steel porous disc pre-saturated with wetting phase is placed in the bottom cap of the cell, and one fully-wet nylon membrane with appropriate pore size (Table 2.1) is placed on the disc. The sample chamber is then fastened to the bottom cap carefully to avoid air bubbles between membrane and porous disc, and wetting phase is added to the chamber to a depth of approximately 3 mm. Porous material soaked in wetting phase is then gradually packed into the chamber. During packing, the sample in the cell is stirred and the cell is tapped against the bench frequently, and the excess water or $CaCl_2$ solution is wiped away. According to Oliviera *et al*. [1996], this kind of wet-packing procedure results in a denser and more uniform packing compared to other dry or wet packing techniques.

After packing, a second hydrophilic membrane is placed on top of the porous material, and the top cap, with a saturated porous disc in it, is fastened to the chamber. The cell is then saturated by pumping 10-15 pore volumes of wetting phase at a flow rate of 1 mL/min through the cell using a syringe pump (model KDS 230, KD scientific Inc., Holliston, MA). After saturation is finished, the valve is closed, and the top membrane is replaced with a Teflon membrane. The gas phase tubing is connected to the top of the cell and the valve is opened prior to the start of the experiment.

2.3.3. *Measurement of Detailed Hysteretic P_c-S Relationships*

Detailed P_c-S relationships (which include multiple scanning curves) presented in here were measured using a slow dynamic (pseudo-static) technique, where pressures were adjusted and saturation measured continuously (pressure ramps were discretized in steps with 3 to 12 second durations, depending on the length of the run and the amount of

desired data). The rate of ramps was determined for all cases through preliminary experiments to be fast enough to provide detailed information within the desired time, and slow enough to ensure that the measured dynamic P_c-S relationships would closely match measurements made using static equilibrium methods. Preliminary experiments involved conducting partial dynamic runs at various pressure rates, and selecting the largest rate below which further change in measured relationships was not observed. The decision to use a dynamic approach was based in part on an observation that the rapid pressure jumps between steps in static methods often caused flow problems after several drainage/imbibition cycles, causing bubbles to come out of solution and become trapped in tubing. The more gradual pressure and flow changes of the dynamic approach were much less likely to cause this problem, increasing the amount of data that could be collected. Rates of pressure change (dP_n/dt) used for each porous medium in the measurement of detailed hysteretic P_c-S relationships are given in Table 2.1, along with other run conditions. To demonstrate the validity of the measured slow dynamic P_c-S relationships, static P_c-S curves were produced for two selected materials (F-110 and SCS-250) with the same automated device operated in a static mode.

2.4. RESULTS AND DISCUSSION

Five kinds of porous media were used for detailed study of gas-water P_c-S relationships. The results are illustrated in Figures 2.4 to 2.8. Experiments start from fully saturated media (S = 1), so the measurement sequence of drainage/imbibition cycles shown in each figure is from outer loop to inner loop, with drainage being measured first in each loop.

Besides the primary drainage and main imbibition loop, between 3 and 14 scanning loops were completed for each soil. Experience with the system showed that reproducible P_c-S relationships could be achieved if total run times were kept less than 24 hours to minimize the effects of diffusion of gas across the water-wet membrane and formation of bubbles, particularly when higher pressures were used. Although the effects of gas bubbles on volume measurements were minimal even after 24 hours for slow dynamic-mode runs, the bubbles tended to become trapped in tubing junctions after multiple cycles, eventually blocking imbibition. For this reason, the number of loops possible for a given porous medium is dependent on the permeability of the medium, with sands allowing more loops to be completed in a 24 hour period than silts.

2.4.1. *P_c-S Relationships of Sand Samples*

Detailed gas-water P_c-S relationships of F-95 fine sand under different run conditions are shown in Figures 2.4 and 2.5. In Figure 2.4, the run has been designed so scanning curves are centered approximately half way between the residual and natural wetting phase saturations (S_{wr} and $S_{nwr,}$ respectively). F-95 is the coarsest material used in the detailed P_c-S study. As a result, among all the porous media presented, it was possible to complete the most loops for F-95 within the shortest time: a total of 15 loops were completed within 13.0 hours. The time needed to complete both primary drainage and main imbibition was approximately 1.6 hours.

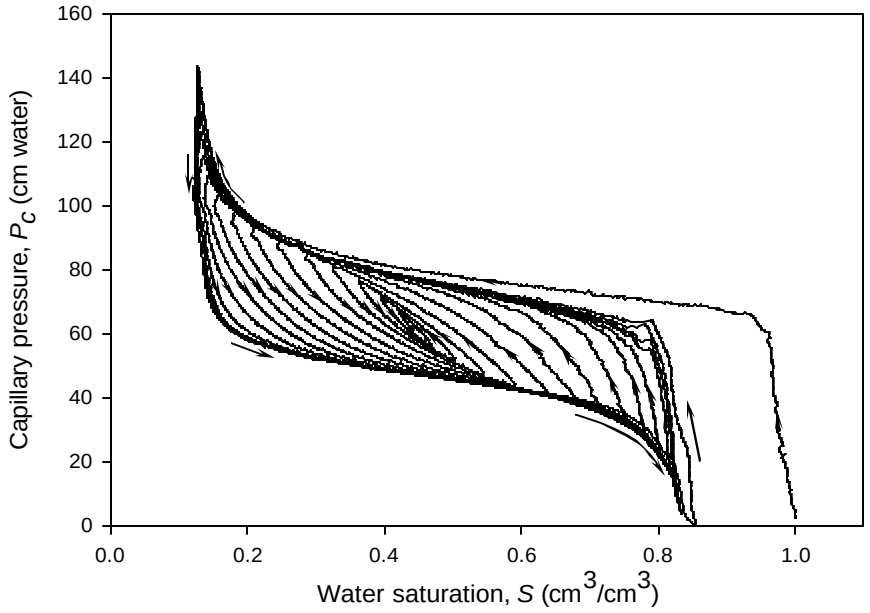


Figure 2.4. Measured slow dynamic (pseudo-static) gas-water P_c-S relationship for F-95 fine sand.

Figures 2.5A and 2.5B illustrate P_c-S relationships for F-95 sand with scanning loops centered at high and low saturations respectively. As these figures illustrate, it is possible to use the device to measure response of a soil to any pre-programmed drainage/imbibition history, capturing any combination of the infinite number of scanning curves possible for a system. Also, the similarity of three different P_c-S curves (Figures 2.4 and 2.5) in measured displacement pressure (the capillary pressure plateau in the primary drainage curve) and residual water saturation demonstrates the excellent reproducibility of the device.

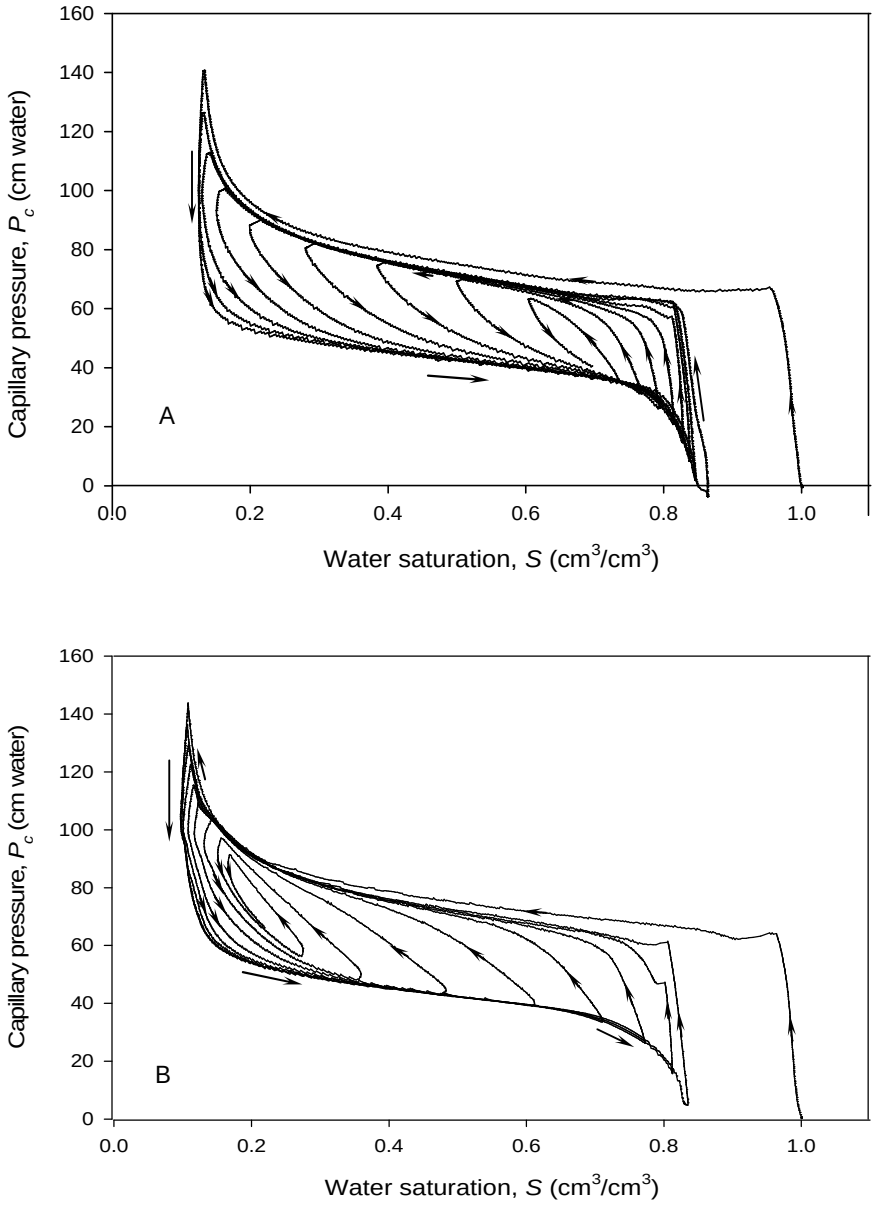


Figure 2.5. Measured slow dynamic (pseudo-static) gas-water P_c-S relationships for F-95 sand with scanning loops centered at high (A) and low (B) saturations.

The detailed P_c-S relationship of F-110 fine sand is plotted in Figure 2.6, with both static (symbols) and dynamic (lines) runs shown. For F-110, which is finer than F-95, the displacement pressure obtained from a fit to the Brooks-Corey equation [Brooks and Corey, 1966] is 71 cm water (7.0 kPa) in comparison with 64 cm water (6.3 kPa) for F-95 (Table 1). Due to the lower permeability of F-110, approximately 3.3 hours was required for F-110 to complete the loop of primary drainage and main imbibition (in comparison with 1.6 hours for F-95), and 14.8 hours were needed to finish a total of 8 loops.

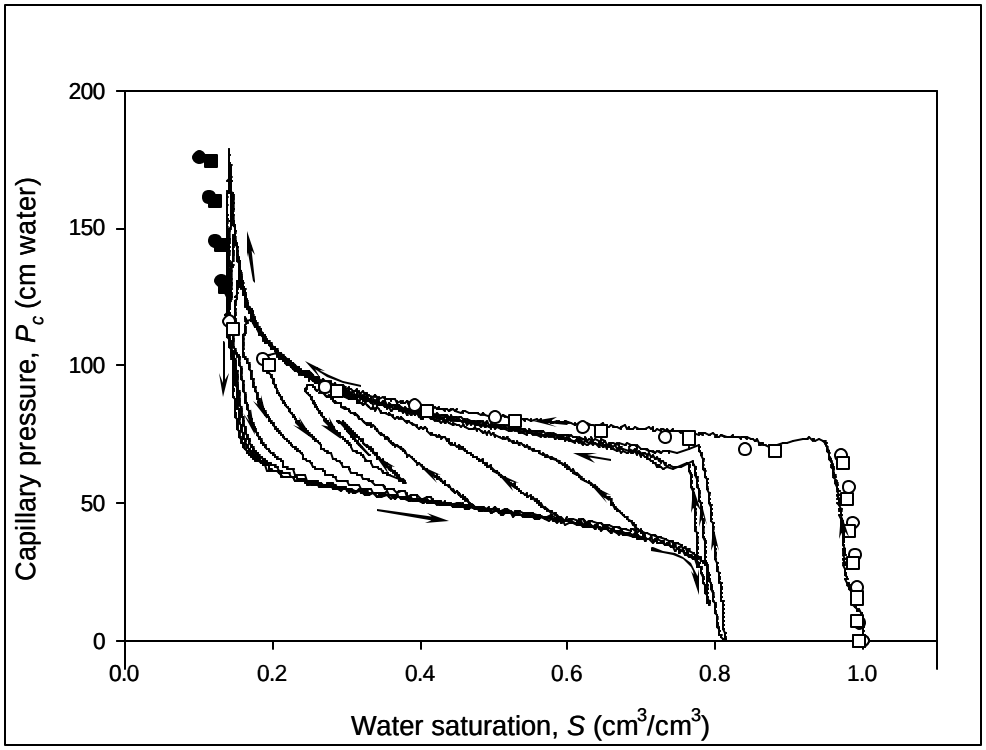


Figure 2.6. Measured gas-water P_c-S relationships for F-110 ultra-fine sand. Lines correspond to slow dynamic (pseudo-static) measurements. Symbols correspond to two static primary drainage curves. Solid symbols indicate gas diffusion in static runs.

Comparison of the static and slow dynamic results in Figure 2.6 shows that the slow dynamic runs closely match the static runs for the condition used. Only at the lowest saturation values ($S < 0.15$) is a difference noted, with the static runs showing slightly lower saturation for given capillary pressures. The main source of the difference is gas diffusion through the water-wet capillary barrier, which was observed near residual water saturation in static experiments, causing the under-measurement of water saturation. Static measurements exhibiting diffusion effects are denoted by solid symbols in Figure 2.6. (In reality, the solid symbols are not true static values, in that measured saturation continues to drift due to gas diffusion; if capillary pressure is held at those values, measured (apparent) saturation will eventually become negative as the volume of gas accumulating below the capillary barrier continues to increase.) The occurrence of air diffusion near residual water saturation in static experiments highlights a further advantage of slow dynamic (pseudo-static) runs, in that slow dynamic conditions can often allow membranes to be used at much higher capillary pressures than is possible with static runs. Gas diffusion through water wet membranes is a function of both the capillary pressure (the driving force for gas to cross the membrane) and saturation (the fraction of the membrane in contact with the gas phase), with higher capillary pressure and lower saturation likely to produce more rapid gas diffusion. Any technique that can reduce the time spent under those conditions can increase the number of scanning loops that can be measured as well as the maximum operating pressure.

2.4.2. *P_c-S Relationships of Silt Samples*

Air-water P_c-S relationships of three silts are shown in Figures 2.7 and 2.8. Silts have much smaller grain sizes than sands, and as such require higher pressures for

drainage. Because of the low permeabilities of many silts, complete drainage or imbibition can be expected to take considerably longer than for sands. However, for the materials tested, it was found that rates of pressure change similar to those used with the sands could produce reasonable results. The reason for this is that even at the same rate, the much higher pressures required for drainage of the silts mean that each complete drainage or imbibition will take much longer for the silts. For example, as listed in Table 2.1, the pressure changing rate, dP_n/dt, for silt SCS-250 (0.070 cm water per sec) is almost the same as that for sand F-95 (0.071 cm water per sec). But the maximum applied gas phase pressure was 844 cm water for SCS-250, compared to 211 cm water for F-95. The difference in applied pressure and the similarity in rates of pressure change means that to finish the same drainage/imbibition process, a SCS-250 measurement will take approximately four times as long as an F-95 measurement.

Note that although the method is applicable to many materials that require capillary pressures as high as 1000 cm water (98 kPa), it can not necessarily be applied to all materials in this category. The major consideration is permeability of the material (when both fully and partially saturated). Some silts with substantial clay content may not be able to drain rapidly enough to complete drainage and imbibition cycles within the time required to minimize bubble formation. Future work will examine methods of increasing the feasible run-time for these types of materials. One possible approach would be to include an in-line membrane degasser (of the type commonly used in high performance liquid chromatography applications) below the pressure cell to remove any bubbles that have formed.

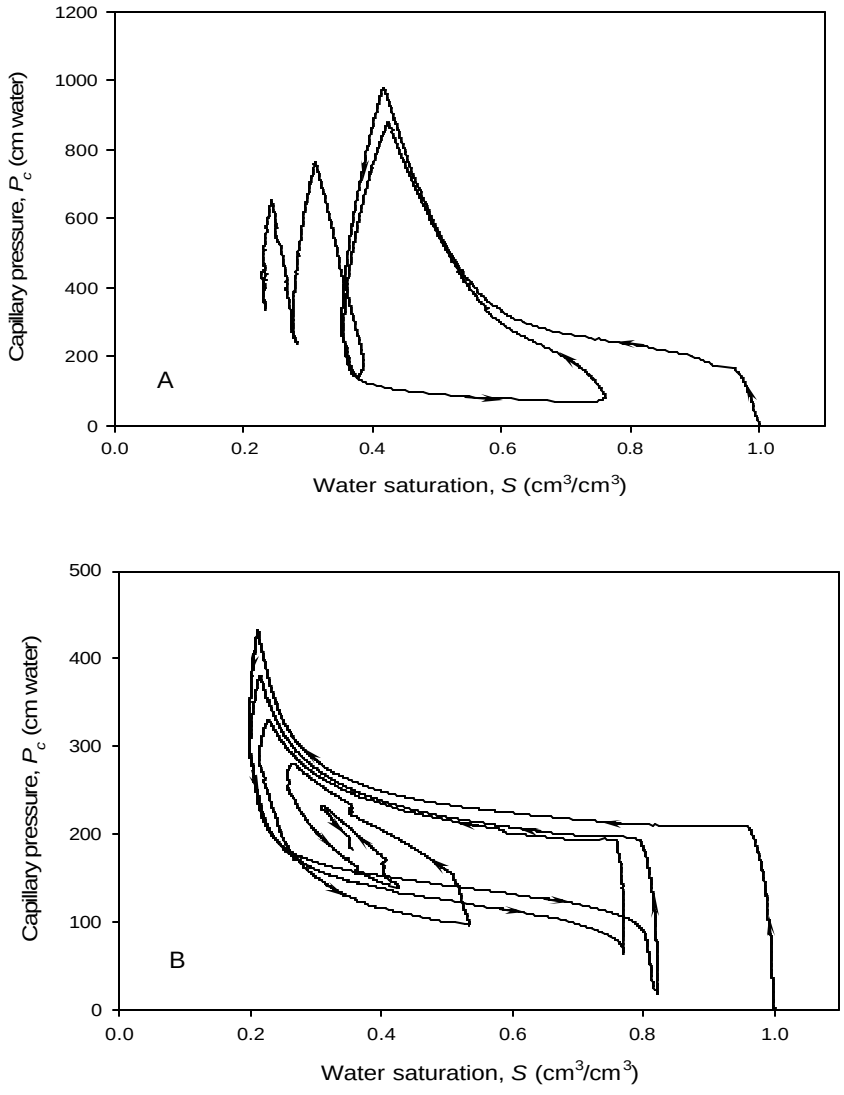


Figure 2.7. Measured slow dynamic (pseudo-static) gas-water P_c-S relationships for CRA 200-PAN silt. (A) Measured with Nanopure water, illustrating membrane clogging due to fines dispersion, and (B) measured with 0.01 M $CaCl_2$ solution to reduce clogging due to fines.

An additional problem with fine-grained materials, such as silts, is the potential for dispersion of fines which can clog membranes. Figure 2.7A illustrates the effects of fines dispersion on the P_c-S relationship for CRA 200-PAN silt measured using Nanopure

water as the wetting phase. Although drainage begins as expected, drainage slows considerably below a saturation of approximately 0.6, and the P_c-S curve becomes very steep, as drainage is unable to keep up with increasing capillary pressure. The effects of clogging can also be noted in the continued drainage during the start of each imbibition cycle, indicating that the system is far from static equilibrium conditions. Upon completion of the experiment, a reddish discoloration was visible on the water-wet membrane beneath the soil (CRA 200-PAN is reddish in color due to iron oxide coatings.) Problems of clogging would also be expected to influence traditional techniques by significantly lengthening equilibration times.

One mechanism to reduce the dispersion of fines is to include a multivalent ion with the wetting phase to reduce the double layer around soil surfaces. (If tap water were used in place of Nanopure water, this would be less of a concern, although added multivalent ions may still be needed for many materials.) Figure 2.7B shows the results of adding 0.01 M $CaCl_2$ to the wetting solution. In this case, a total of 5 loops were completed within 18.7 hours for CRA 200-PAN silt, and 6.4 hours were needed to finish the primary drainage and main imbibition curves. Note that the P_c-S relationship is much improved for this low permeability material with the addition of $CaCl_2$.

Figure 2.8 shows hysteretic P_c-S relationships for two silts with even higher Brooks-Corey displacement pressures than the CRA 200-PAN: SCS-250 and SCS-125 (Table 2.1). In both cases, 4 drying/wetting cycles were completed within 15.3 hours, and 6.3 hours were required to finish the primary drainage/main imbibition loop. The resulting P_c-S relationships are detailed and very usable, although still somewhat noisier than those measured for sands.

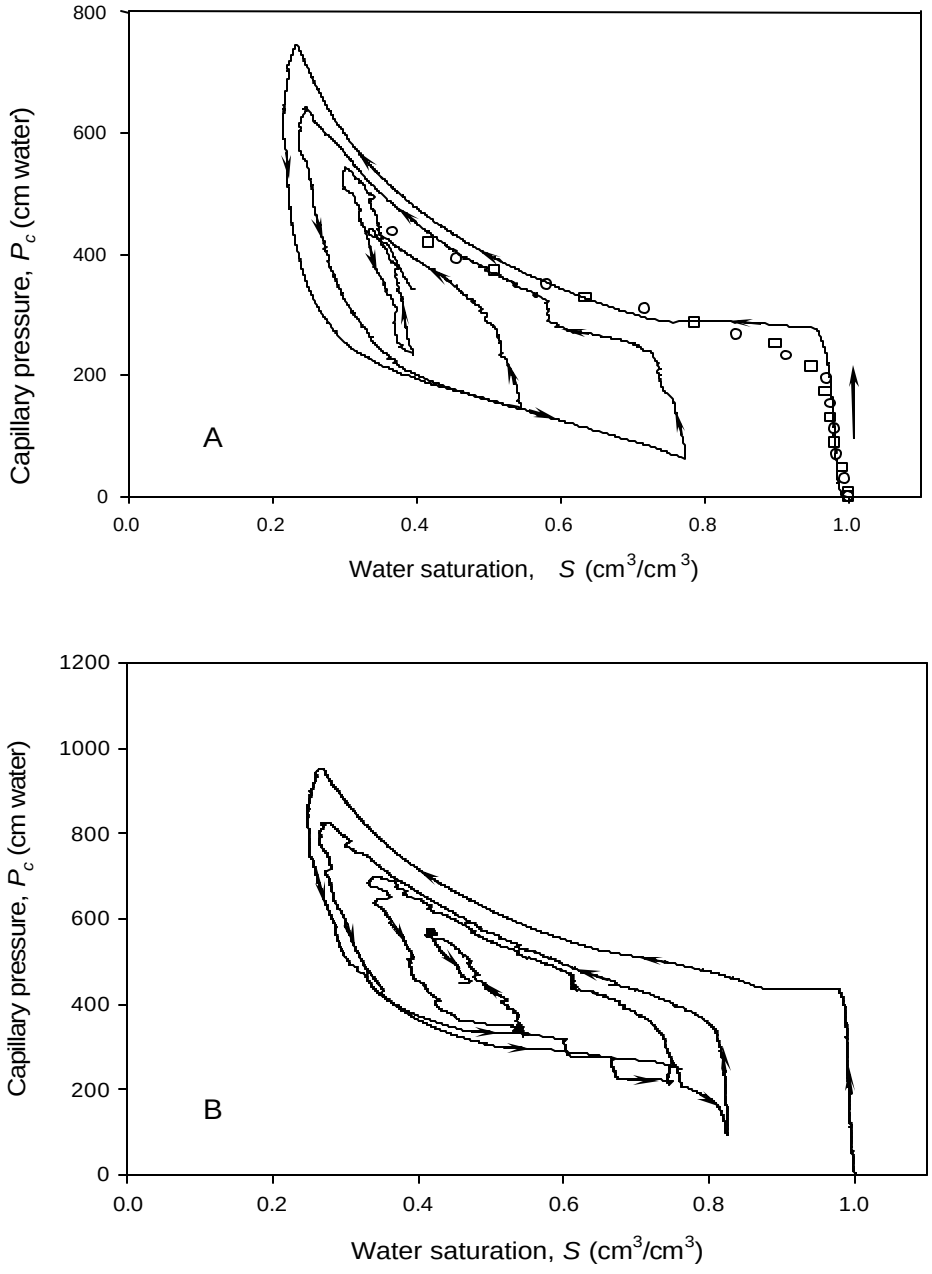


Figure 2.8. Measured gas-water P_c-S relationships for SCS-250 (A), and SCS-125 (B). Lines in both figures correspond to slow dynamic (pseudo-static) measurements. Symbols in (A) correspond to two static primary drainage curves.

For comparison, static equilibrium primary drainage measurements were made for SCS-250 using the same device (symbols in Figure 2.8A). The shown static curves were only measured to a water saturation of 0.36 due to gas diffusion below that saturation. In general, the static and slow dynamic P_c-S curves are in very good agreement, although the use of a slow dynamic (pseudo-static) mode allows considerably more-detailed runs to be made.

Although the P_c-S relationships measured for silts (Figures 2.7 and 2.8) are clearly not as good as those measured for sands (Figures 2.3 to 2.5), they still provide considerable detail. Perhaps most important, to the authors' knowledge, hysteretic P_c-S relationships for silts have not previously been reported, and would be extremely difficult to measure using other existing techniques where prohibitively long equilibration times are needed.

2.5. CONCLUSIONS

An automated laboratory apparatus was developed to rapidly measure two-phase (gas-liquid or liquid-liquid) hysteretic P_c-S relationships. The device can be operated under both static and dynamic conditions, making it well-suited to study the detailed P_c-S characteristics and dynamic effects of various porous media.

In this chapter, the detailed hysteretic P_c-S curves of various materials were measured under slow dynamic (pseudo-static) conditions and were found to agree well with static data obtained using the same device. The use of slow dynamic conditions

minimizes problems associated with gas diffusion, allowing more detailed measurements to be conducted.

Major advantages of the device over conventional methods are: 1) its ability to measure detailed hysteretic P_c-S relationships for materials as fine as silts and for capillary pressures as high as approximately 1000 cm water (98 kPa), and 2) its ability to make rapid, detailed measurements of dynamic effects in porous media.

Chapter 3

Hysteresis in Dynamic Effects in Capillary Pressure-Saturation Relationships and Unsaturated Flow

3.1. INTRODUCTION

When pressure changes (wetting, nonwetting or both phases) occur in an unsaturated environment, the movement of fluids and the modification of the fluid-fluid interface in a porous medium may depend on both the rate of saturation change and the drying/wetting history. The dynamic response of porous media to pressure changes is basically controlled by two parameters: relative permeability and dynamic capillary pressure effects. These parameters are discussed in the following sections. In the work presented here, dynamic effects are defined to include the effects of both relative permeability effects and dynamic capillary effects on porous medium response.

3.1.1. *Determination of Hydraulic Conductivity in Unsaturated Porous Media*

For a long time, the measurement and modeling analysis of hydraulic conductivities of porous media have been the subject of numerous studies from various scientific disciplines [e.g. Brooks and Corey, 1966; Klute and Dirksen, 1986; Eching, *et al*., 1994; Butters and Duchateau, 2002], since the hydraulic conductivity has a broad application in many areas, including hydrology, geology, soil science, agriculture, environmental engineering, and petroleum engineering. In general, methods used to determine the magnitude of hydraulic conductivity can be divided into two groups: direct measurement and indirect estimation.

Traditional techniques for direct measurement of hydraulic conductivities at different saturations involve steady-state experiments [e.g. Klute and Dirksen, 1986; Dirksen, 1990]. Steady-state experiments are time-consuming and elaborate. Recently researchers have started to develop faster alternative methods to determine unsaturated conductivity ($K_{(s)}$), mostly using transient outflow methods [e.g. Eching, et al., 1994; Wildenschild, *et al*., 1997; 2001; Butters and Duchateau, 2002]. In all cases, Darcy's law (Equation 3.1) is applied to determine $K_{(s)}$ values by measuring water flow rates (Q) at known water pressure head drops across the porous media (Dh).

$$Q = K_{(s)} A \frac{\Delta h}{L} \qquad (3.1)$$

where, A and L are the cross sectional area and the length along the flow direction of the porous media, respectively.

As an alternative to direct measurement, indirect methods estimate the hydraulic conductivity mainly based on porous media properties that are more easily found or measured, such as grain size distribution, porosity, bulk density, or P_c-S curve [e.g. Nimmo, 1999; Kravchenlo and Zhang, 1999; Timlin, *et al*., 1999; Jauhiainen and Karvonen, 1999]. Among the numerous models reported, those developed by Brooks and Corey [1966] and van Genuchten [1980] are most successful and most commonly applied by researchers in unsaturated flow studies [e.g. Eching and Hopmans, 1993; Wildenschild, *et al*., 2001; Belieav and Schotting, 2001; Butters and Duchateau, 2002]. Equation (3.2), deduced by integrating the Burdine's relative permeability equation [Brooks and Corey, 1966], describes Brooks-Corey function for estimating relative

permeability (k_{rw}). Relative permeability is defined as the ratio between unsaturated and saturated (K_{SAT}) conductivities ($K_{(s)} = K_{SAT} k_{rw}$).

$$k_{rw}^{BC} = S_e^{3+2/l} \tag{3.2}$$

$$S_e = \frac{S - S_{wr}}{1 - S_{wr}} \tag{3.2a}$$

where, the superscript *BC* represents Brooks-Corey, S_e is the effective water saturation, S_{wr} is the water residual saturation, λ is the pore size distribution index, with large values for well sorted media and small values for poorly sorted media. λ can be determined by fitting Brooks-Corey P_c-S equation (Equation 3.3) to the primary drainage P_c-S curve.

$$P_c = p^d / (S_e)^{1/l} \qquad \text{for } P_c \geq p^d \tag{3.3}$$

where, p^d is the displacement pressure. The applicability of Equations (3.2) and (3.3) has been verified for both consolidated and unconsolidated porous media [Brooks and Corey, 1966].

Recently there has been an increasing interest in the inverse estimation of unsaturated conductivity [e.g. Eching and Hopmans, 1993; Vogel, *et al*., 1999; Bohne, *et al*., 1999; Simunek, *et al*., 1999; Wildenschild, *et al*., 2001; Butters and Duchateau, 2002]. The method applies numerical modeling to simulate transient flow experiments by optimizing hydraulic parameters used to estimate hydraulic constitutive properties (such as P_c-S and $K_{(s)}$ curves). Although the application of inverse estimation is promising in studying the hydraulic properties of porous media, especially under conditions exhibiting nonequilibrium phenomena, concerns on the method arise, such as the accuracy of transit

flow experiments, the selection of which parameters to optimize and the non-uniqueness of optimization [Hopmans and Simunek, 1999].

With transient flow experiments, the dependence of unsaturated conductivity on the flow rate was investigated. Different results were reported by different researchers using different methods. Wildenschild *et al*. [2001] found a decreased conductivity at an increased flow rate using one- and multi-step outflow methods. In contrast, an increase in the conductivity with flow rate was reported by Schultze *et al*. [1999] using continuous outflow, and by Plagge *et al*. [1999] using one-step outflow and evaporation methods. Despite these different results, there are two common attributes in the studies mentioned above. First, the difference in the magnitude of conductivity as a function of saturation between different flow rates is usually within a factor of 3, which is within the regular error range associated with experimental measurements. Second, the difference diminishes when the flow rate is small enough.

Although different methods for determining hydraulic conductivity may provide different results, it is widely accepted that the unsaturated conductivity decreases nonlinearly with the decrease of saturation, and so does relative permeability since K_{SAT} is fixed for a given medium and fluid. However, since most, if not all, studies on hydraulic conductivity overlook the natural wetting/drying process, whether the conductivity function is hysteretic or not during draining and imbibing remains unclear. In a modeling analysis on the nonequilibrium effects in water-oil displacement, Barenblatt *et al*. [2003] proposed that relative permeability during imbibition should be higher than at equilibrium. However, supporting experimental evidence is missing.

3.1.2. *Determination of Dynamic Capillary Effects*

As mentioned in Chapter 2, when the capillary pressure-saturation (P_c-S) relationship is measured under dynamic conditions, the P_c-S curve obtained does not necessarily match the true P_c-S relationship determined under static conditions if the rate of capillary pressure change is too great for the porous medium to drain/imbibe or the sensors to respond. The value of capillary pressure measured at a particular saturation by dynamic methods may be larger in drainage and smaller in imbibition than the corresponding value of P_c determined with static methods, and the difference is expected to be proportional to the rate of saturation change. The dependence of dynamic capillary pressure on the rate of saturation change (Equation 3.4) is referred to as dynamic capillary effects [Hassanizadeh and Gray 1993; Hassanizadeh *et al*., 2002].

$$P_c^d - P_c^s = -t \frac{\partial S}{\partial t} \tag{3.4}$$

where P_c^d is the dynamic capillary pressure, which is the difference of average pressures measured in nonwetting and wetting phases (i.e., $P_n - P_w$), P_c^s is the static capillary pressure determined through static equilibrium measurements, and represents the equilibrium capillary pressure at a particular saturation for a given drying or wetting process, $\partial S/\partial t$ is the partial time derivative of wetting phase saturation, and t is the dynamic capillary coefficient, a measure of dynamic capillary effects. The dynamic capillary coefficient, t, has a nonnegative value, indicating the rate dependence of dynamic capillary pressure. Based on an analysis of literature data, Hassanizadeh *et al*. [2002] estimated t to be in the range of 3×10^2 to 5×10^5 cm·s (3×10^4 to 5×10^7 kg/(m·s))

for different types of sand. More recently, researchers have experimentally determined t of sand to be approximately $10^2 \sim 10^3$ cm·s ($10^4 \sim 10^5$ kg/(m·s)) during drainage [Manthey, *et al*., 2004; Oung, *et al*., 2005] (Oung *et al*. reported t in the range of 10 – 600 kg/(m·s); however they appear to have a units conversion error in their calculation of t. Based on the data in their paper, their t values should be three orders of magnitude higher.)

Although experimental evidence is limited, it has been suggested that t may be a function of saturation, and also may have a hysteretic nature [Beliaev and Hassanizadeh, 2001; Hassanizadeh *et al*., 2002]. O'Carroll *et al*. [2005] assumed t to be linearly related to water saturation when incorporating t into a multiphase flow simulator. Published computational results based on a two-phase flow simulator [Manthey *et al*., 2005], a pore network model [Gielen, *et al*., 2004], and bundle-of-tubes calculations [Celia, *et al.*, 2004] have all indicated a non-linear t-S relationship. Increasing numbers of modeling studies have begun to incorporate dynamic effects to better understand the multiphase flow phenomena [Beliaev and Schotting, 2001; Beliaev, 2003; O'Carroll *et al*., 2005]. However, experimental examination on the dependence of t on S and the possible hysteretic nature of t -S relationships present in different drying/wetting processes are still missing from the literature.

3.1.3. *Objective*

The objective of the work described in this chapter was to experimentally investigate the hysteresis of dynamic effects exhibited by a fine sand, when responding to dynamic pressure changes. The apparent dynamic coefficient (t^*), a parameter taking into

account both relative permeability (k_{rw}) and dynamic capillary coefficient (t) effects, was measured as a function of saturation for primary drainage, main imbibition, and secondary drainage, using the automated P_c-S device described in Chapter 2. The relative magnitudes of k_{rw} and t were calculated from t^* with the application of Darcy's law and Brooks-Corey equations. Implications of experimental results for dynamic unsaturated flow are discussed.

3.2. MATERIALS AND METHODS

3.2.1. *Materials*

The porous medium used in this research is fine sand F-95 received from U.S. Silica (Berkeley Springs, WV). F-95 has a mean grain size of 140 μm and a packed porosity of 0.349 (Table 2.1). Nitrogen gas and nanopure water (Nanopure Infinity, Barnstead International, Dubuque, Iowa) are used as non-wetting and wetting phases, respectively.

3.2.2. *Quantification of Dynamic Effects*

Measurements for this chapter were conducted with the P_c-S device described in Chapter 2. Because the device measures wetting phase pressure below the pressure cell, the pressure difference between non-wetting and wetting phases measured during dynamic runs (referred to here as apparent dynamic capillary pressure, P_c^{d*}) includes pressure gradients in the soil, across the plate and membrane, and along the tubing connecting the bottom of the cell and pressure transducer, in addition to the true dynamic

capillary pressure (P_c^d). Interpretation of the relative magnitudes of effects of t and k_{rw} requires quantifying the magnitude of these individual effects.

In general, one-dimensional unsaturated flow at any given saturation can be described by Darcy's law (Equation 3.1). During drainage, water flows downward in the cell. When water pressure inside the unsaturated porous medium is assumed to change linearly with the length of the cell (a reasonable assumption for a 1.27 cm high cell, where saturation is essentially uniform throughout), water pressure head drop (Dh) across the cell can be described as:

$$\Delta h = 2\left(P_w - P_{w,B}\right) \tag{3.5}$$

where, P_w is the water pressure at the middle of the sample, which is also the average water phase pressure needed in the calculation of dynamic capillary pressure (P_c^d), and $P_{w,B}$ is the water phase pressure at the bottom of the porous medium (*i.e.*, the top of the plate).

During measurements, the plate and membrane at the bottom of the cell and the tubing between the cell and the pressure transducer remain saturated. Applying Darcy's law gives:

$$P_{w,B} = P_{w,msrd} + \frac{QL_{p+m}}{K_{p+m}^e A} + \frac{QL_t}{K_t^e A_t} \tag{3.6}$$

where, $P_{w,msrd}$ is the measured water phase pressure during the dynamic run, Q is the flow rate at any given saturation of porous medium, L_{p+m} and K_{p+m}^e are the total thickness and effective saturated conductivity of plate and membrane, respectively, A is the cross

sectional area of the cell, L_t, K_t^e, and A_t are the length, effective saturated conductivity and cross sectional area of tubing, respectively.

The pressure difference between nonwetting and wetting phases measured in dynamic runs is referred to as apparent dynamic capillary pressure (P_c^{d*}):

$$P_c^{d*} = P_n - P_{w,msrd} \tag{3.7}$$

Combining Equations 3.5 to 3.7 and noting that $P_c^d = P_n - P_w$, the water pressure head drop across the sample can be described as:

$$\Delta h = 2\left(P_c^{d*} - P_c^d - \frac{QL_{p+m}}{K_{p+m}^e A} - \frac{QL_t}{K_t^e A_t} \right) \tag{3.8}$$

Darcy's law says: $\Delta h = \frac{QL}{K_{(s)}A}$ (3.9)

for drainage, $Q = -\frac{\partial S}{\partial t} nLA$ (3.10)

where n is the porosity. Equating Equations (3.8) and (3.9), substituting Equations (3.4) and (3.10), and noting that $A = 625A_t$ for the described device, Equation (3.11) is obtained:

$$P_c^{d*} - P_c^s = -\left(t + \frac{nL^2}{2K_{SAT}k_{rw}} + \frac{nL_{p+m}L}{K_{p+m}^e} + \frac{nL_tL}{K_t^e} \right)\frac{\partial S}{\partial t} \tag{3.11}$$

Note that the third and fourth terms in the parentheses in Equation (3.11) are constant throughout measurements for a given system. If we define a term of apparent

dynamic coefficient (t^*), corresponding to the measured apparent dynamic capillary pressure (P_c^{d*}), as:

$$t^* = t + \frac{nL^2}{2K_{SAT}k_{rw}} + m \tag{3.12}$$

$$m = \frac{nL_{p+m}L}{K_{p+m}^e} + \frac{nL_tL}{K_t^e} \tag{3.12a}$$

Equation (3.11) becomes:

$$P_c^{d*} - P_c^s = -t^* \frac{\partial S}{\partial t} \tag{3.13}$$

In this case, the newly proposed parameter, the apparent dynamic coefficient (t^*), includes both relative permeability effects and dynamic capillary effects. Note that Equation (3.13) has the same form as Equation (3.4). As such, t^* can be determined as the slope of the linear plot between P_c^{d*} and $\partial S/\partial t$ at any given saturation, and P_c^s is the intercept of the linear regression. These facts allow a continuous t^*–S relationship to be developed from a series of apparent dynamic P_c-S curves measured at different rates.

Re-arranging Equation (3.12), k_{rw} can be estimated for a known t :

$$k_{rw} = \frac{nL^2}{2K_{SAT}(t^* - t - m)} \tag{3.14}$$

The estimated k_{rw} can be compared with k_{rw}^{BC} calculated from the Brooks-Corey function (Equation 3.2). In addition, setting t = 0 in Equation (3.14) gives $k_{rw}^{t=0}$, where all

resistance to flow is considered due to the relative permeability effect. Differences between $k_{rw}^{t=0}$ and k_{rw}^{BC} may indicate the effects of dynamic capillary pressure.

With a known k_{rw} value, the dynamic capillary coefficient, t, can be calculated:

$$t = t^* - \frac{nL^2}{2K_{SAT}k_{rw}} - m \tag{3.15}$$

In the work reported here, k_{rw}^{BC} from Brooks-Corey function (Equation 3.2) is applied to estimate the contribution of t to t^*, where applicable. As such, the accuracy of the estimate depends on the accuracy of the Brooks-Corey relative permeability function model (Equation 3.2). Although it has previously been proposed that the dynamic k_{rw} might be different from statically measured, the difference was found to be minor even for a saturation rate at least three times faster than the fastest drainage applied here [Stauffer, 1978; Plagge, *et al*., 1999; Schultz, *et al*., 1999; Wildenschild, *et al*., 2001]. As such, k_{rw} can be considered constant (at a particular saturation) within the flow rates covered in this work.

Equations (3.5) through (3.14) are derived based on the drainage process, however it can be shown that the same equations (Equations 3.13 to 3.15) apply to imbibition. For imbibition, water flows upwards in the cell, so Equations (3.5), (3.6) and (3.10) are replaced by Equations (3.16), (3.17) and (3.18), respectively.

$$\Delta h = 2\left(P_{w,B} - P_w\right) \tag{3.16}$$

$$P_{w,B} = P_{w,msrd} - \frac{QL_{p+m}}{K_{p+m}^e A} - \frac{QL_t}{K_t^e A_t} \tag{3.17}$$

$$Q = \frac{\partial S}{\partial t} nLA \tag{3.18}$$

Following the same processes, the same equations as Equations (3.13) to (3.15) can be derived to calculate t^*, k_{rw} and t for imbibition.

All the parameters needed in calculation are listed in Table 3.1.

Table 3.1. Parameters used in dynamic coefficients calculation for F-95 sand.

Parameter		Value
Effective saturated conductivity of plate and membrane (20 μm pore size), K^e_{p+m} (cm/s) [a]		5.40×10^{-4}
Length of plate and membrane, L_{p+m} (cm)		0.184
Effective saturated conductivity of tubing K^e_t (cm/s) [b]		25.40
Length of plate and membrane, L_t (cm)		50
Saturated conductivity of F-95 sand, K_{SAT} (cm/s) [a]		2.22×10^{-3}
Length of the packed F-95 sand (cm), L (cm)		1.27
Porosity of F-95 sand, n		0.349
Pore size distribution index, λ [c]		6.15
Water residual saturation, S_{wr} [d]	Primary drainage	0.140
	Main imbibition	0.136
	Secondary drainage	0.141

Note: a: Measured using constant head method [Fetter, 2001].
b: Measured using falling head method [Fetter, 2001].
c: Obtained from fitting Brooks-Corey P_c-S equation (Eqn. 3.3) to the pseudo-static primary drainage curve.
d: The minimum water saturation of the slowest (pseudo-static) P_c-S curve for each drainage or imbibition (the ending saturation for drainage, and the beginning saturation for imbibition).

3.2.3. *Experimental Measurement of Apparent Dynamic P_c-S Curves*

Apparent dynamic P_c-S relationships were measured using the automated P_c-S device described in Chapter 2, with the same procedure, operation and capillary barrier selection. Different rates of the change of saturation (referred to as saturation rates for convenience) were achieved by adjusting the rates of the change of the applied gas phase pressure (dP_n/dt) (referred to as pressure rates for convenience). Methods to obtain apparent dynamic P_c-S curves for each of drying/wetting process studied here are briefly described below.

For primary drainage, each P_c^{d*}-S curve is obtained from a different fully-saturated sand sample, operated at a different pressure rate from each other. For main imbibition, all P_c^{d*}-S curves are from a single originally fully-saturated sand sample. Prior to each imbibition, the sand is first slowly drained to the same water residual saturation under the same pseudo-static conditions. Subsequent main imbibition P_c^{d*}-S curves with different rates of saturation change are obtained by decreasing the gas phase pressure from the maximum value to zero at different speeds. All P_c^{d*}-S curves for secondary drainage are also from a single sand sample. The fully-saturated sand is first drained to water residual saturation, and then imbibed to natural water residual saturation (*i.e.*, the water saturation reached at the end of the main imbibition, Figure 2.1), and then the secondary drainage is conducted. Subsequent secondary drainages with different pressure rates are conducted after imbibing the sand to the same natural water residual saturation starting point. For all drainage and imbibition processes studied here, the slowest P_c^{d*}-S curves were measured under pseudo-static conditions (dP_n/dt = 0.042 cm

water per second), where the flow rate was slow enough to eliminate the dynamic effects (*i.e*. to produce a dynamic P_c-S curve that matches static measurements, Chapter 2).

3.2.4. *Determination of the Pore Size Distribution Index (l)*

The pore size distribution index, λ, is determined by fitting Brooks-Corey P_c-S function (Equation 3.3) to the pseudo-static primary drainage P_c-S curve (Figure 3.1), using the S_{wr} value listed in Table 3.1. The values of l and p^d obtained from the fit are 6.15 and 59 cm water, respectively. The good agreement between the measured and the fit curves supports the use of Brooks-Corey functions in the work described here.

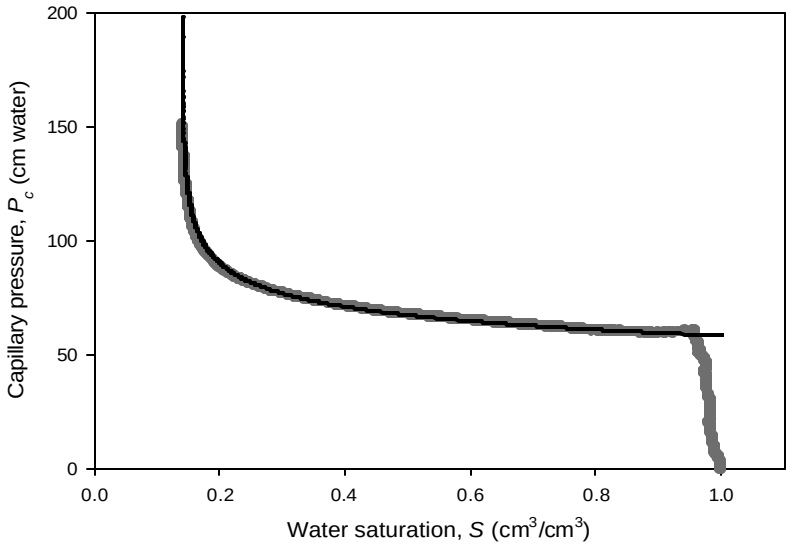


Figure 3.1. Brooks-Corey fit to the measured pseudo-static primary drainage P_c-S curve of F-95 sand. Gray symbols: measured curves; black lines: best fit results.

3.2.5. *Determination of the Apparent Dynamic Coefficient (t^*)*

For a drying or wetting process where the starting point is well-defined, such as the primary drainage, main imbibition or secondary drainage, static capillary pressure (P_c^s) at a given saturation is fixed. From Equation (3.13), it is apparent that the apparent dynamic coefficient (t^*) can be determined as the slope of a linear fit to the plot between the apparent dynamic capillary pressure (P_c^{d*}) and the saturation rate ($\partial S/\partial t$) (each P_c^{d*}-S curve contributes one pair of P_c^{d*} and $\partial S/\partial t$ at every saturation). The intercept of the linear fit at each saturation gives an estimate of the static capillary pressure, P_c^s. Regression calculations are conducted using a C++ program written specifically for this work. For each drainage or imbibition process studied here, between 1150 and 1720 data points were calculated for t^* within the reported saturation range. Spacing of data points is based on the slowest curves (for which the most data points exist). Values of P_c^{d*} are interpolated for faster curves, where values of saturation do not exactly match the slow curves.

In this research, data from the near-vertical regions of the P_c^{d*}-S curve (near complete saturation and residual saturation) were not considered in calculations because those regions, where subtle changes in saturation may correspond to large differences in capillary pressure, are more sensitive to slight differences in packing and subject to give substantial errors. Perhaps more important, it is apparent that Equations (3.4) and (3.13) can not be valid in near vertical regions of P_c-S curves, as different P_c^d or P_c^{d*} values will give the same $\partial S/\partial t$ (zero). This is evident in bad regression fits where the steep portions

of curves are included. In this research, for each P_c^{d*}-S curve, only the region with a slope (dP_c^{d*}/dS) less than arbitrarily-selected 500 cm water was used in regressions. As such, fewer dynamic curves may be used in calculations at low saturations for drainage, since fast curves may not finish at the same saturation as slow curves. In this research, at least seven apparent dynamic curves were used in regression at any reported saturation. For each experiment, the static capillary pressure, P_c^s, resulting from regression is only reported in the saturation range where correlation coefficients (r^2) are greater than 0.5 (r^2 values over ranges shown in figures were typically 0.7-0.9 for primary drainage measurements, which were based on different packed cells, and typically larger than 0.95 for imbibition and secondary drainage measurements, which were based on a single packed cell for each process). Further, the apparent dynamic coefficient, t^*, is only reported in the saturation region where the reported P_c^s values from regression are in good agreement with the measured pseudo-static P_c-S curve.

3.3. RESULTS AND DISCUSSION

3.3.1. *Measured Apparent Dynamic and Predicted Static P_c-S Curves*

Primary Drainage. Figure 3.2 shows eight primary drainage P_c^{d*}-S curves of F-95 sand, measured at pressure rates (dP_n/dt) ranging from 0.042 (slowest run) to 0.42 (fastest run) cm water per second. This rate range corresponds to time scales ranging from 83 to 8.3 minutes to finish each entire primary drainage shown in Figure 3.2. In general, the higher the applied dP_n/dt, the higher the observed apparent dynamic capillary pressure at a given saturation. Further, as dP_n/dt increases, the saturation at which curves become steep and appear to approach an apparent residual saturation increases. The static

capillary pressure, P_c^s, obtained as the intercept in the linear regression to determine t^* at each saturation, is also plotted in Figure 3.2 as a function of saturation. The result shows that the static capillary pressure is well predicted over most of the saturation range studied, except for the region where saturation is below 0.339.

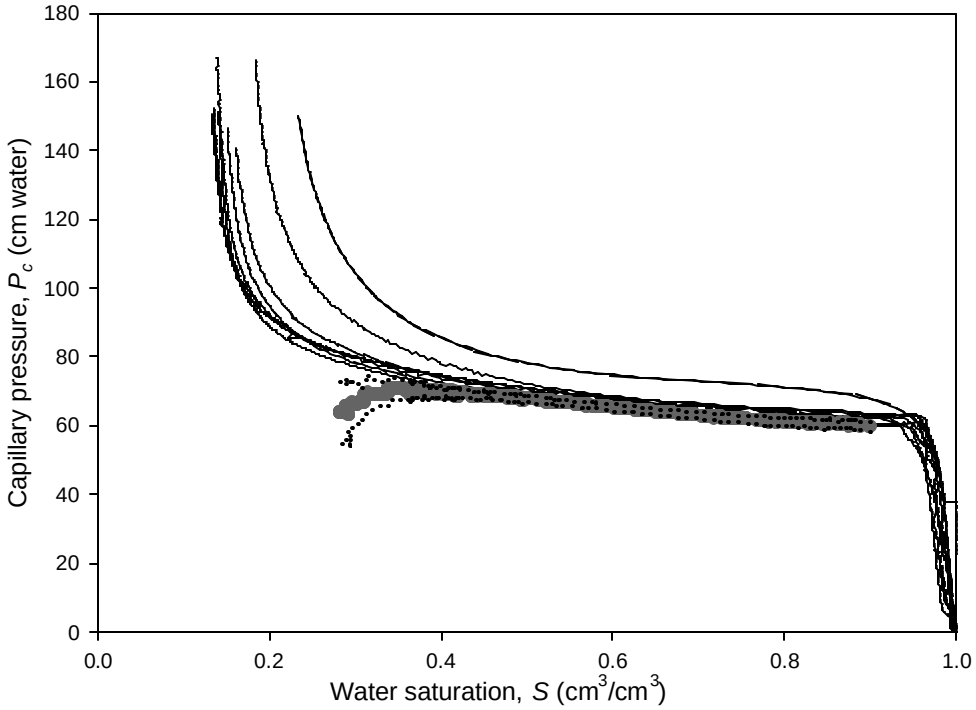


Figure 3.2. Primary drainage P_c-S curves of F-95 sand. Solid black lines: apparent dynamic curves measured at different pressure rates(0.42, 0.21, 0.14, 0.105, 0.084, 0.07, 0.052 and 0.042 cm water per second from top to bottom curves, respectively); gray symbols: predicted static curve; dotted black lines: standard error of static P_c when predicted from linear regression at each saturation.

Main Imbibition. A total of eleven main imbibition P_c^{d*}-S curves are shown in Figure 3.3, along with the corresponding preceding drainage curves. All preceding drainages were conducted under the same pseudo-static condition, where a dP_n/dt value of 0.035 cm water per second was applied as the pressure rate (100 minutes to finish each entire drainage curve), to ensure the sand was drained to the same water residual saturation prior to the start of each subsequent main imbibition process. To study dynamic effects in the imbibition process, imbibition P_c-S curves were measured at eleven different dP_n/dt values ranging from -0.035 to -1.05 cm water per second, corresponding to time scales of 100 to 3.3 minutes to complete the entire imbibition curve. There are two significant differences between the measured P_c^{d*}-S curves for primary drainage (Figure 3.2) and for main imbibition (Figure 3.3). First, while higher apparent dynamic capillary pressure was observed for the faster drainage, lower apparent dynamic capillary pressure was obtained for the faster imbibition at a given saturation. This is because the capillary pressure has to decrease to initiate imbibition, and when the decrease of capillary pressure is faster than the response of the system, lower capillary pressure will be observed at a given saturation. Second, while the water residual saturation reached at the end of primary drainage was dependent on the speed of the drainage (the faster the drainage, the higher the apparent water residual saturation (Figure 3.2)), all of the imbibition curves in Figure 3.3 finished at the same natural water residual saturation at the end of imbibition. This phenomenon indicates that the controlling forces driving drainage and imbibition may be different. The static main imbibition P_c-S curve predicted from regressions is also plotted in Figure 3.3, which illustrates that the static capillary pressure is well-predicted over the entire saturation range studied.

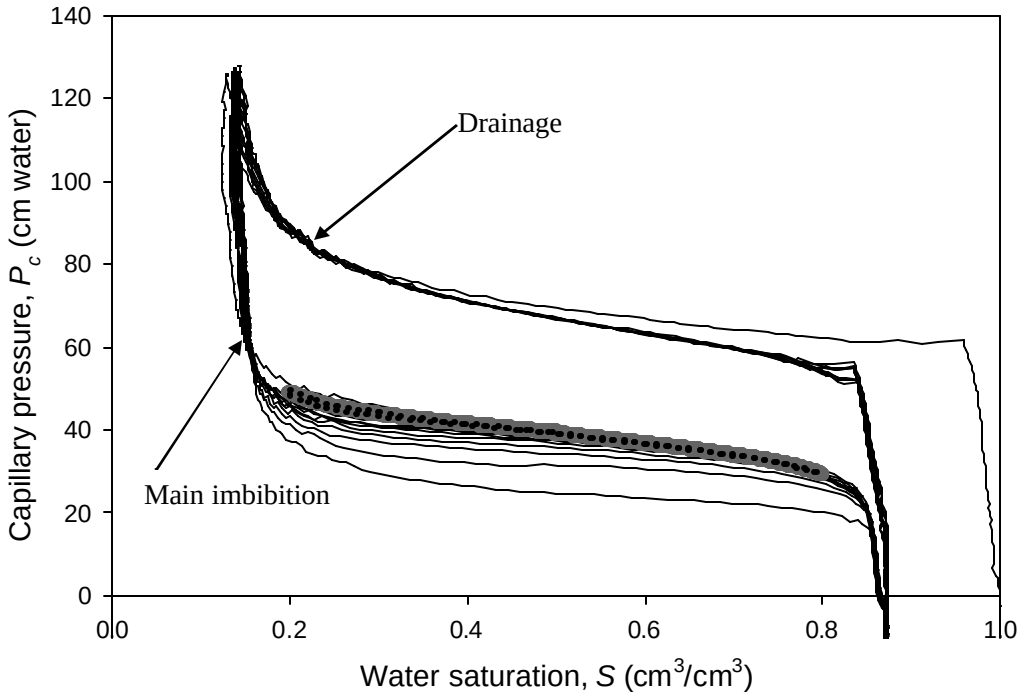


Figure 3.3. Main imbibition P_c-S curves of F-95 sand. Solid black lines: apparent dynamic imbibition curves measured at different pressure rates (0.035, 0.105, 0.117, 0.131, 0.15, 0.175, 0.21, 0.263, 0.35, 0.525, 1.05 cm water per second from top to bottom curves, respectively) with preceding drainage curves measured under constant pseudo-static conditions; gray symbols: predicted static curve; dotted black lines: standard error of static P_c when predicted from linear regression at each saturation.

Secondary Drainage. Figure 3.4 shows eight P_c^{d*}-S curves for F-95 secondary drainage used to study dynamic effects. These curves were measured under the same dynamic rates as the primary drainage (Figure 3.2), with dP_n/dt values ranging from 0.042 to 0.42 cm water per second. The static P_c-S curve resulting from regression is also plotted in Figure 3.4 along with dynamic curves. The result shows that the static capillary pressure is well predicted over most of the saturation range under study, except for the region where saturation is below 0.236.

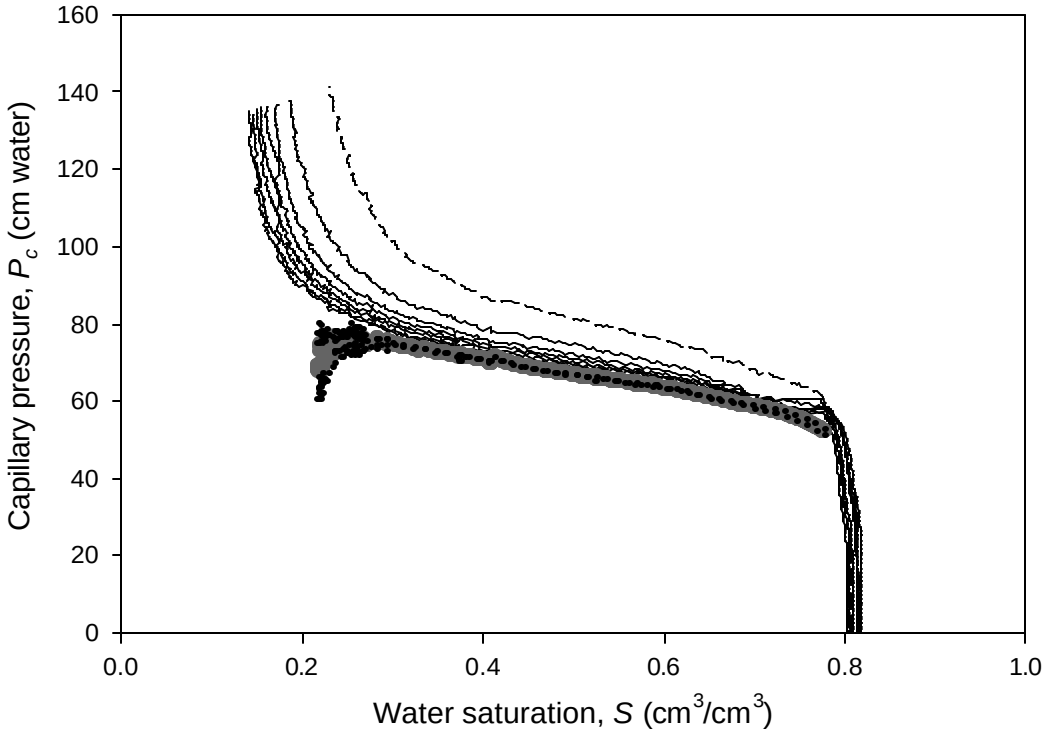


Figure 3.4. Secondary drainage P_c-S curves of F-95 sand. Solid black lines: apparent dynamic curves measured at different pressure rates (0.42, 0.21, 0.14, 0.105, 0.084, 0.07, 0.052 and 0.042 cm water per second from top to bottom curves, respectively); gray symbols: predicted static curve; dotted black lines: standard error of static P_c when predicted from linear regression at each saturation.

3.3.2. *Apparent Dynamic Coefficient (t^*) Calculated from P_c^{d*}-S Curves*

As indicated by Equation (3.13), the apparent dynamic coefficient, t^*, is determined as the slope of the linear regression between P_c^{d*} and $\partial S/\partial t$ at any given saturation. Figures 3.5, 3.6 and 3.7 show the regression results for primary drainage, main imbibition, and secondary drainage, respectively. Note that in the work described here, dynamic coefficients (including t^*, t, and k_{rw}) are determined as a function of water effective saturation (S_e) instead of actual water saturation (S) for convenience, because k_{rw}^{BC} is directly related to S_e (Equation 3.2). Water residual saturation (S_{wr}) values used in calculating S_e (Equation 3.2a) can be found in Table 3.1.

Primary Drainage. Figure 3.5 shows the t^*-S_e relationship for the primary drainage of F-95 sand. Note that Figure 3.5 only illustrates t^* values within the saturation range where the predicted P_c^s agrees well with the measured pseudo-static P_c-S curve (Figure 3.2) to ensure the reliability of the reported t^*. Two dotted lines above and below the experimental data represent the standard error of the calculated values from the linear regression. The standard error is relatively high for primary drainage, mostly due to the packing variations between individual samples used to measure the P_c^{d*}-S curves in Figure 3.2. In general, t^* increases as a power function with the decrease of effective saturation, with the value of t^* ranging from 1.5×10^3 to 1.0×10^4 cm·s (1.5×10^5 to 9.9×10^5 kg/(m·s)) within the studied saturation range.

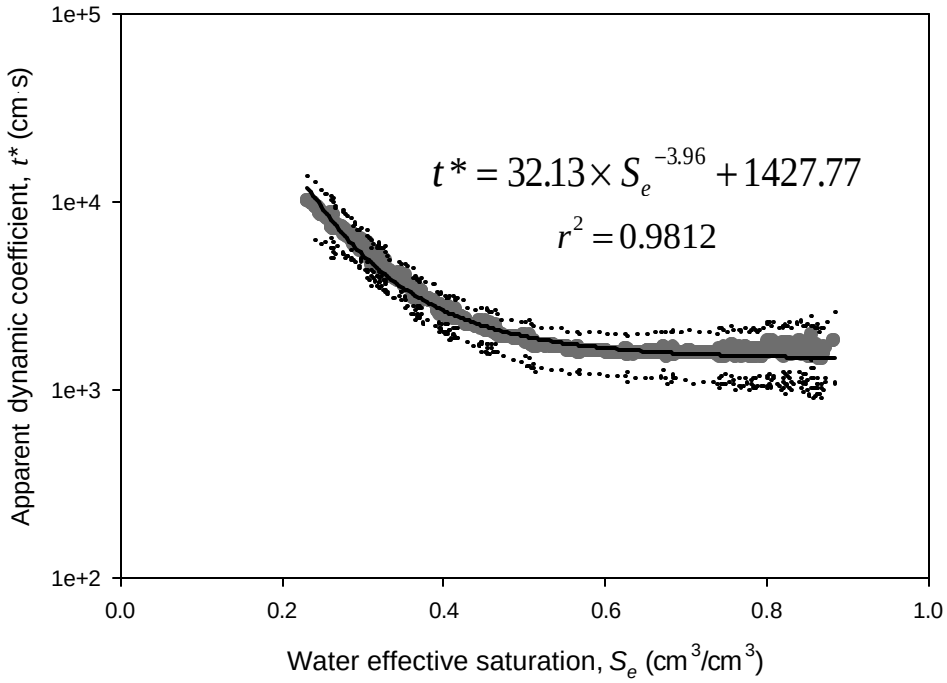


Figure 3.5. The relationship between apparent dynamic coefficient and water effective saturation for primary drainage of F-95 sand. Gray symbols: measured value; dotted black lines: standard error of the measured value from linear regression at each saturation; solid black line: power function fit result.

Main Imbibition. Figure 3.6 shows the t^*-S_e relationship determined for main imbibition of F-95 sand. Note that standard errors of main imbibition t^* values resulting from linear regression (represented by two dotted lines in Figure 3.6) are much smaller than standard errors of primary drainage t^* values (Figure 3.5). This is because measurements of P_c^{d*}-S curves used to calculate t^* for main imbibition were based on one single packed sample, which excludes errors from packing variations (packing variations are considered to be a major source of relatively high errors in primary drainage t^*). Over the saturation range covered in Figure 3.6, the magnitude of t^*

measured for main imbibition is between 7.9×10^2 and 2.5×10^3 cm·s (7.8×10^4 and 2.5×10^5 kg/(m·s)), which is much lower than t^* values for primary drainage. Similar to primary drainage, t^* for main imbibition also increases as a power function with the decrease of effective saturation over most of the studied saturation range. More detailed comparison between drainage and imbibition is given later in the **Hysteresis in t^*-S_e Relationships** section.

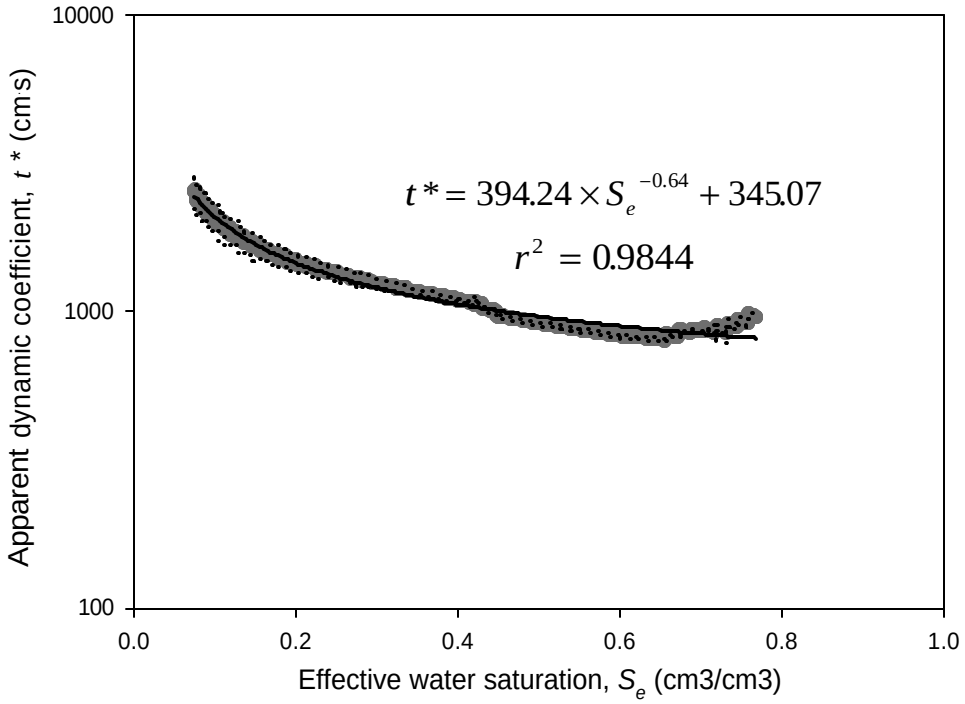


Figure 3.6. The relationship between apparent dynamic coefficient and water effective saturation for main imbibition of F-95 sand. Gray symbols: measured value; dotted black lines: standard error of the measured value from linear regression at each saturation; solid black line: power function fit result.

Secondary Drainage. Figure 3.7 shows the t^*-S_e relationship calculated for secondary drainage of F-95 sand, within the saturation range where P_c^s values were well predicted (Figure 3.4). Similar to what was observed for main imbibition (Figure 3.6), in most cases standard errors for secondary drainage t^* values (dotted lines in Figure 3.7) are small, because the measurements based on one single packed sample. The t^*-S_e relationship obtained for secondary drainage exhibits the same trend as that for primary drainage (Figure 3.5), and is well described by a three-parameter power function with a negative exponent,. Within the saturation range reported in Figure 3.7, t^* for secondary

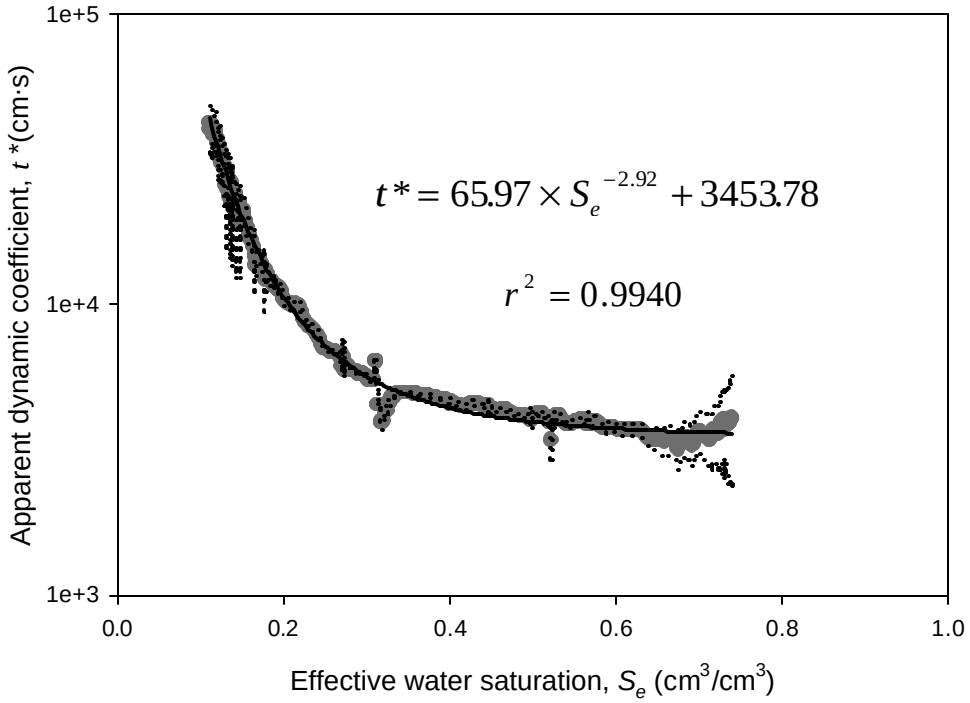


Figure 3.7. The relationship between apparent dynamic coefficient and water effective saturation for secondary drainage of F-95 sand. Gray symbols: measured value; dotted black lines: standard error of the measured value from linear regression at each saturation; solid black line: power function fit result.

drainage was determined to be in the range of 3.5×10^3 to 4.3×10^4 cm·s (3.4×10^5 to 4.2×10^6 kg/(m·s)), which is higher than that observed for both primary drainage (1.5×10^3 to 1.0×10^4 cm·s) and main imbibition (7.9×10^2 to 2.5×10^3 cm·s).

Hysteresis in t^*-S_e Relationships. To better illustrate the dependence of dynamic response of porous media on the drying/wetting history, the t^*-S_e relationships measured for primary drainage, main imbibition, and secondary drainage, are re-plotted together in Figure 3.8.

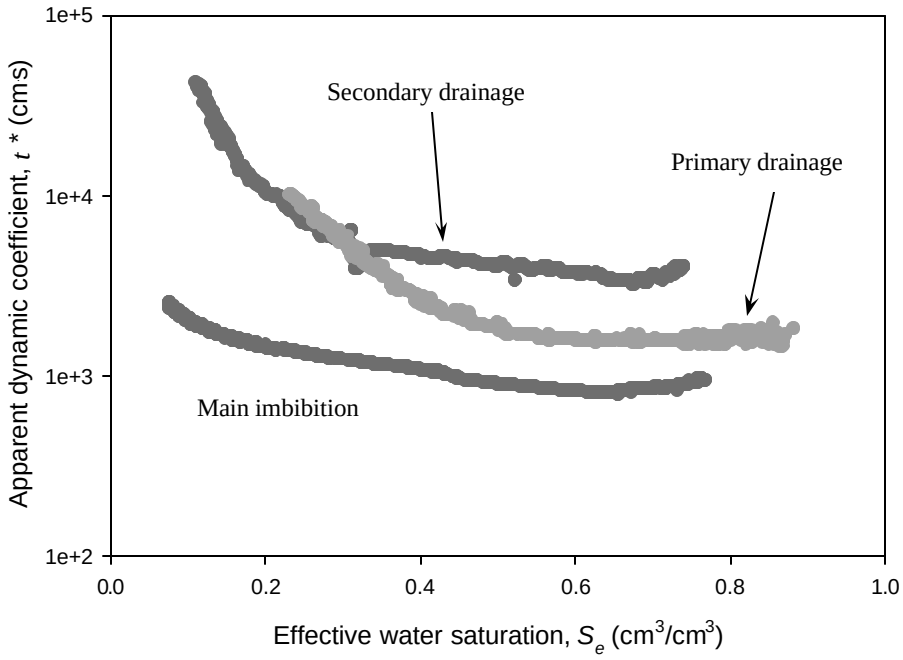


Figure 3.8. Comparison of the measured apparent dynamic coefficients for primary drainage, main imbibition and secondary drainage of F-95 sand.

Comparing the measured t^*-S_e curves for drainages and imbibition, both primary and secondary drainages exhibit greater t^* values than main imbibition, with a greater difference (up to more than one order of magnitude) observed at lower saturation. Specifically, t^* for main imbibition increases gradually as saturation decreases within the entire saturation range studied. In contrast, for primary and secondary drainages, the gradual increase of t^* with the decrease of saturation is only observed at high saturations, but not at low saturations, where the measured t^*-S_e curve is very steep. The difference in the overall slopes of t^*-S_e relationships for drainages and main imbibition determines the difference in the magnitude of the exponents in the power functions describing t^*-S_e relationships (-3.96 and -2.92 for primary and secondary drainages, respectively, versus -0.64 for main imbibition, Figures 3.5 to 3.7).

The hysteresis of apparent dynamic coefficients exhibited during drainage and imbibition implies that the response of porous media to dynamic pressure changes is controlled by different processes during drainage and imbibition. Drainage is forced by the applied non-wetting phase pressure, and the flow responding to the pressure change is basically controlled by the conductivity of the porous system. This is supported by the power functions describing t^*-S_e relationships observed for drainages, in which the absolute values of exponents (3.96 and 2.92 for primary and secondary drainages, respectively) are close to that found in Brooks-Corey k_{rw} function (Equation 3.2, $k_{rw}^{BC} = S_e^{3.33}$ for F-95 sand). In contrast, imbibition is a spontaneous process responding to the loss of applied external forces, and the internal capillarity controls the imbibition flow. It is very likely that inherent capillarity weakens the effect of water conductivity

(and also its dependence on saturation), producing relatively high flow rates over the entire imbibition and resulting in relatively low apparent dynamic coefficients. This is, at least in part, a possible reason causing hysteresis in dynamic effects between drainage and imbibition, particularly at low saturations.

Hysteresis in t^*-S_e relationships is also observed between the two hysteretic drainages studied in this research (Figure 3.8). With similar trends in t^*-S_e curves for primary and secondary drainages, secondary drainage exhibits higher t^* values at high saturations ($S_e > 0.3$). Assuming that relative permeability effects are generally same for the two drainages, the result implies that higher dynamic capillary effects maybe present in secondary than in primary drainage. This implication is supported by the higher dynamic capillary coefficient calculated for secondary drainage (see the **Section 3.3.4. *Hysteresis in Dynamic Capillary Effects***).

3.3.3. *Relative Permeability*

As indicated by Equation (3.12), t^*-S_e relationships illustrated in Figures 3.5 to 3.8 include both relative permeability effects and dynamic capillary effects. To separate the two effects, k_{rw} was calculated using Equation (3.14) by assuming dynamic capillary effects are not included in the observed t^*-S_e relationships (i.e. $t = 0$). The resulting $k_{rw}^{t=0}$-S_e relationships for primary drainage, main imbibition, and secondary drainage are shown in Figures 3.9 to 3.11, along with the k_{rw}^{BC}-S_e relationship obtained from Brooks-Corey k_{rw} function (Equation 3.2).

Primary Drainage. Figure 3.9 illustrates the $k_{rw}^{t=0}$-S_e and k_{rw}^{BC}-S_e relationships for primary drainage. Results show that when $S_e \leq 0.441$, the two k_{rw}-S_e curves match each other very well, indicating that P_c^{d*} and t^* measured at low saturations are mainly due to the relative permeability effects. At the region where $S_e > 0.441$, however, the $k_{rw}^{t=0}$-S_e curve is lower than k_{rw}^{BC}-S_e curve with a bigger difference observed at higher saturation. This implies that dynamic capillary effects take place at higher saturations during P_c^{d*}-S measurements.

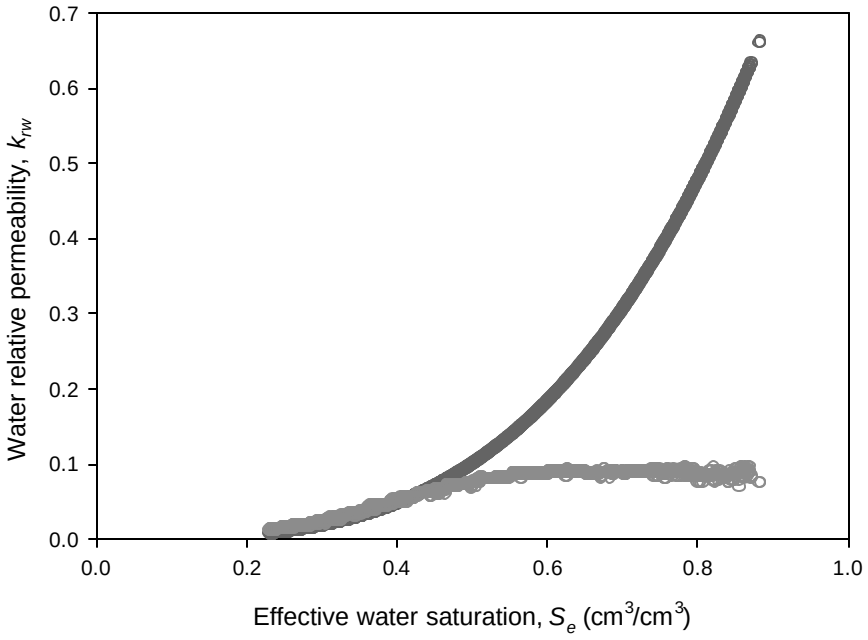


Figure 3.9. Water relative permeability of F-95 as a function of saturation. Dark gray: Brooks-Corey function; light gray: calculated at $\tau = 0$ for primary drainage.

Main Imbibition. Figure 3.10 illustrates the $k_{rw}^{t=0}$-S_e and k_{rw}^{BC}-S_e relationships obtained for main imbibition. Unlike the results for primary drainage (Figure 3.9), the $k_{rw}^{t=0}$-S_e curve obtained for main imbibition is higher than k_{rw}^{BC}-S_e curve within the most part of the studied saturation range ($S_e \leq 0.6$). Since t is a nonnegative coefficient, which means that the $k_{rw}^{t=0}$ value shown in Figure 3.10 is the minimum value could be obtained from t^* (Equation 3.14) at a given saturation, there are three implications from this observation. First, the imbibition flow is probably not controlled by the relative permeability measured under equilibrium, as represented by the Brooks-Corey k_{rw} function (Eqution 3.2). It is very likely that inherent capillarity controls the imbibition flow and overrides the low equilibrium unsaturated water conductivity, producing relatively high flow rates over the entire imbibition. Second, it is likely that the equilibrium relative permeability at a given saturation reached by imbibition is higher than that at the same saturation reached by drainage. Third, unlike the dynamic k_{rw} during primary drainage, which was found close to equilibrium value [Stauffer, 1978; Plagge, *et al*., 1999; Wildenschild, *et al*., 2001], the dynamic k_{rw} during imbibition may be significantly higher than the equilibrium value. This result is consistent with previous modeling work by Barenblatt, *et al*. [2003], who proposed that the relative wetting phase permeability during imbibition might be higher than that measured at equilibrium at any given saturation.

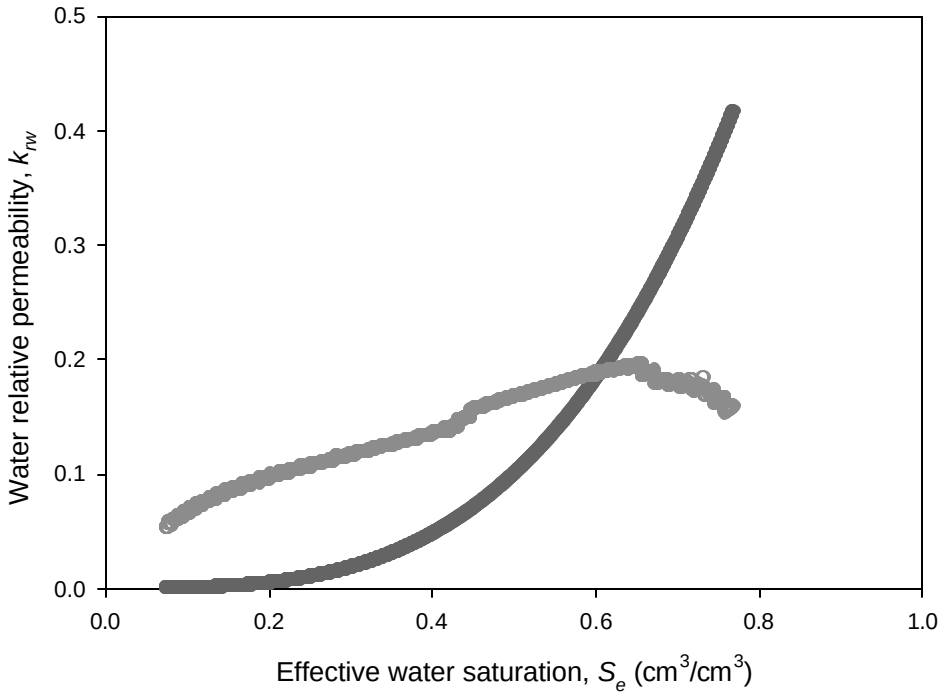


Figure 3.10. Water relative permeability of F-95 as a function of saturation. Dark gray: Brooks-Corey function; light gray: calculated at τ = 0 for main imbibition.

Secondary Drainage. Figure 3.11 plots the $k_{rw}^{t=0}$-S_e and k_{rw}^{BC}-S_e relationships for secondary drainage. Results show that when $S_e \leq 0.336$, the $k_{rw}^{t=0}$-S_e curve matches the k_{rw}^{BC}-S_e curve well, again indicating that drainage flow is mainly controlled by relative permeability at low saturations. Compared to the k_{rw}^{BC}-S_e curve, the lower k_{rw}^{BC}-S_e curve obtained at high saturations ($S_e > 0.336$) indicates that dynamic capillary effects also influence the flow at high saturations.

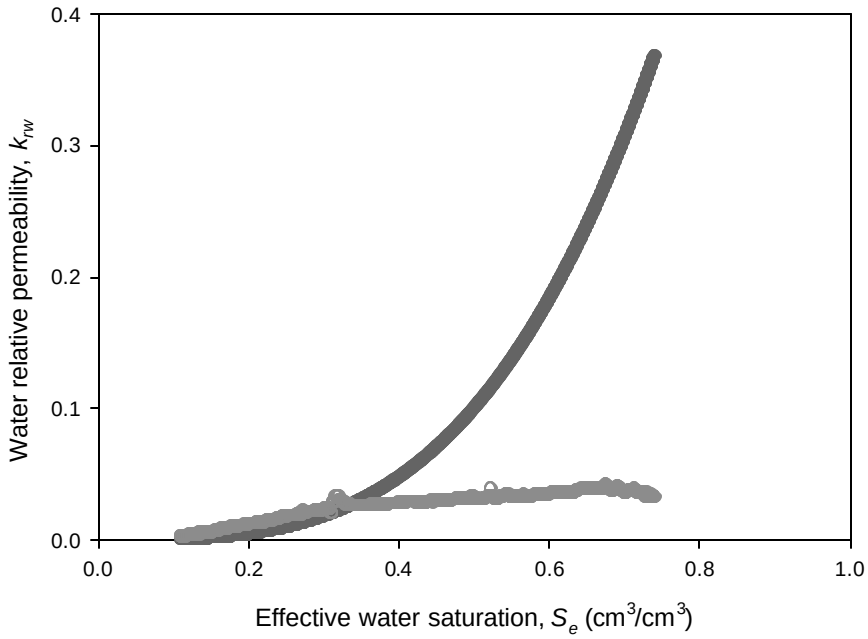


Figure 3.11. Water relative permeability of F-95 as a function of saturation. Dark gray: Brooks-Corey function; light gray: calculated at $\tau = 0$ for secondary drainage.

Hysteresis in $k_{rw}^{t=0}$-S_e Curve. Figure 3.12 re-plots the $k_{rw}^{t=0}$-S_e curves obtained for primary drainage, main imbibition, and secondary drainage along with k_{rw}^{BC}-S_e curve for comparison. Besides the significant difference between drainage and imbibition that has been discussed earlier in the **Main Imbibition** section, Figure 3.12 also shows a lower $k_{rw}^{t=0}$-S_e curve for secondary drainage than for primary drainage at high saturations, indicating that the dynamic capillary effects are higher during secondary than primary drainage. In addition, despite of the dramatic difference in the magnitude of $k_{rw}^{t=0}$ between imbibition and drainages, $k_{rw}^{t=0}$-S_e curve for main imbibition also tends to level off at high

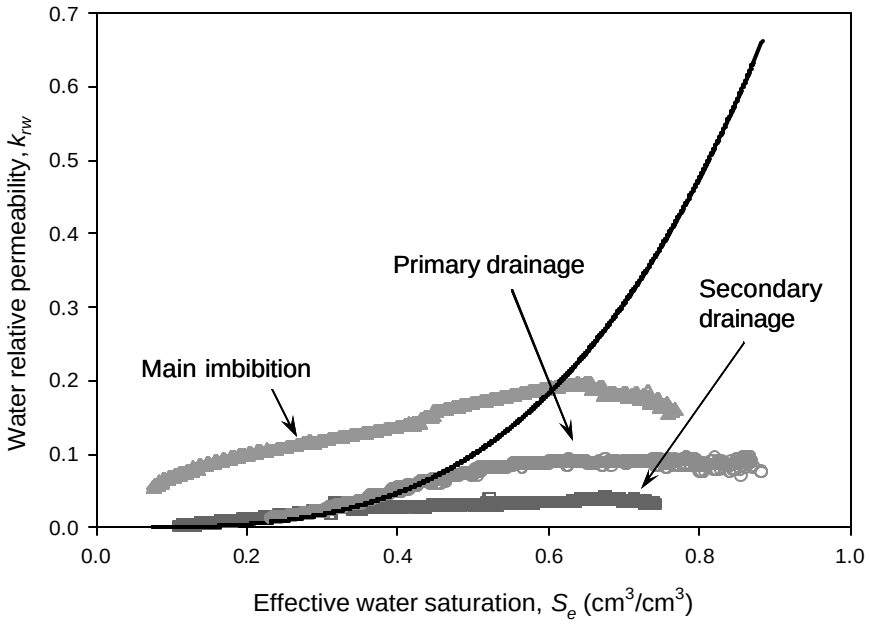


Figure 3.12. Comparison of the $k_{rw}^{t=0}$–S_e curves obtained for primary drainage (light gray circle), main imbibition (light gray triangle), and secondary drainage (dark gray square), along with Brooks-Corey k_{rw} function (black line).

saturations, like what is observed for drainages, suggesting that greater dynamic capillary effects exist at high saturations during imbibition also.

3.3.4. *Hysteresis in Dynamic Capillary Effects*

Results from the calculated $k_{rw}^{t=0}$-S_e curves have shown that dynamic capillary effects exist at high saturation at least for drainages. Dynamic capillary coefficients (t) of drainages can be estimated using Equation (3.15), applying k_{rw}^{BC} equation (Equation 3.2) for required k_{rw} values (Figure 3.13). Note that because $k_{rw}^{t=0}$ for imbibition is greater than k_{rw}^{BC}, t values for imbibition can not be calculated by this method. Also note that, the calculated t values are very sensitive to k_{rw} values, especially at low saturations where k_{rw} is very low. A large negative value may be calculated for t at the low saturation region where $k_{rw}^{t=0}$-S_e and k_{rw}^{BC}-S_e curves match well, when the k_{rw}^{BC}-S_e curve is slightly lower than $k_{rw}^{t=0}$-S_e curve at that region. As such, t values calculated for primary and secondary drainages are only reported in Figure 3.13 for the saturation region with $k_{rw}^{t=0}$-S_e curves lower than the k_{rw}^{BC}-S_e curve.

As shown in Figure 3.13, for both of primary and secondary drainages, t decreases non-linearly with effective saturation and approaches zero at low saturation. This observation is consistent with the earlier studies in which the dynamic primary drainage P_c-S curves were found to converge with the static one at low saturations [e.g., Smiles, *et al*., 1971; Vachaud and Thony, 1971]. More recently, Manthey *et al*. [2004]

reported decreased primary drainage t values with the decrease of saturation within saturation range of 0.75 to 0.60.

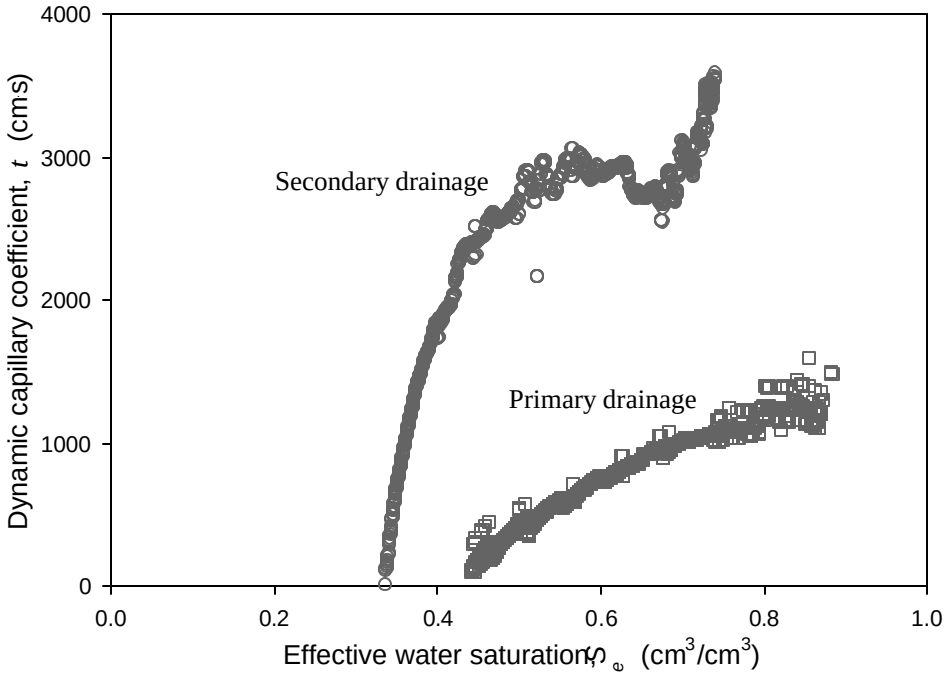


Figure 3.13. Comparison of the relationships between dynamic capillary coefficient and water saturation estimated for primary (square) and secondary (circle) drainages of F-95 sand.

Within the saturation range studied here, t for F-95 primary drainage is estimated to be in the range of 100 to 1500 cm·s (1.0×10^4 to 1.5×10^5 kg/(m·s)) (Figure 3.13), which is in agreement with the published range for sand samples, estimated by Hassanizadeh *et al*. [2002] from literature dynamic P_c-S curves and directly measured by Manthey *et al*.

[2004] and Oung, *et al*. [2005], as well as the values obtained from pore-scale network model [Gielen, *et al*., 2004] and a two-phase flow simulator [Manthey *et al*., 2005].

For secondary drainage, t values are observed to range from 100 to 3500 cm·s (1.0×10^4 to 3.4×10^5 kg/(m·s)) over the studied saturation range (Figure 3.13). At a given saturation covered here, t for secondary drainage is 3 to 20 times higher than t for primary drainage. This observation illustrates the strong hysteretic nature of dynamic capillary effects in P_c-S relationships, like P_c-S relationships themselves. The observed difference in the magnitude of t between primary and secondary drainages means that when the equilibrium between capillary pressure and saturation is disturbed in a given porous media system, the establishment of a new equilibrium will be faster during primary drainage than during secondary drainage when the same amount of disturbance occurs. The hysteresis of dynamic capillary effects observed between primary and secondary drainages may be due to the presence of gas phase prior to the start of secondary drainage, which influences flow conditions. This influence tends to decrease at low water saturations when gas phase becomes predominant in both drainages.

It should be noted that although t values increase with saturation within the studied saturation range, it does not necessarily mean that t keeps increasing beyond the studied saturation range to full saturation, due to the fact that dynamic capillary effects do not exist under saturated conditions. In fact, researchers have found an abrupt decrease of t at near saturation through experimental measurements [Manthey, *et al*., 2004] and modeling analyses [Manthey, *et al*., 2005].

3.4. CONCLUSIONS

In this chapter, the hysteresis of dynamic response of porous media to pressure changes was studied through a newly-developed parameter called the apparent dynamic coefficient (t^*), which is a combined measure of relative permeability effects (measured by relative permeability, k_{rw}) and dynamic capillary effects (measured by dynamic capillary coefficient, t). The apparent dynamic coefficient, t^*, was determined through the measurement of a series of apparent dynamic P_c-S relationships, in which the apparent dynamic P_c (P_c^{d*}) represents the pressure difference between nonwetting and wetting bulk phases. Darcy's Law and Brooks-Corey functions for unsaturated flow were applied to separate the individual contributions of t and k_{rw} to the measured t^*.

Results show strong hystersis in t^*-S_e relationships measured for primary and secondary drainages and main imbition, with the highest t^* values found for secondary drainage and the lowest t^* values for main imbibition. This observation indicates that with the same dynamic pressure change, the response of porous media for a new equilibrium is fastest during imbibition, and slowest during secondary drainage.

Study of k_{rw} shows that k_{rw}-S_e relationships for primary and secondary drainages are likely well described by the Brooks-Corey function (Equation 3.2) at all saturations. However, during main imbibition, much faster response to pressure change is observed, and the k_{rw} values associated with imbibition process are much higher than those calculated from Brooks-Corey function. This observation demonstrates that the k_{rw}-S_e relationship is likely hysteretic for drainage and imbibition. Results further show that the

dynamic water flow is dominated by relative permeability at low saturations and by dynamic capillary effects at high saturations.

Although dynamic capillary coefficient, t, for main imbibition can not be quantified with the method used here, the t-S_e relationships obtained for primary and secondary drainages demonstrate a strong hysteretic nature. While t-S_e curves for both drainages approach zero at low saturations, t for secondary drainage is 3 to 20 times higher than t for primary drainage at any given studied saturation. The result suggests that the P_c-S equilibrium is established faster during secondary drainage than during primary drainage.

Chapter 4

Dependence of Dynamic Effects on Porous Media Properties

4.1. INTRODUCTION

In Chapter 3, it was found that dynamic effects, including both relative permeability effects and dynamic capillary effects, in porous media properties are hysteretic along different drying/wetting paths. The magnitudes of coefficients measuring these dynamic effects, *i.e.*, relative permeability (k_{rw}) for relative permeability effects, dynamic capillary coefficient (t) for dynamic capillary effects, and the apparent dynamic coefficient (t^*) for the combined dynamic effects, depend on both saturation and drying/wetting history. Another factor influencing the magnitude of these dynamic effects is the properties of porous media and fluids.

There are several ways in which porous media properties can influence dynamic effects. To begin with, the relative permeability function of different porous media varies with different pore size distribution index, if the Brooks-Corey function (Equation 3.2) applies. Further, the dynamic capillary coefficient is believed to be a function of the properties of porous media and fluid. It has been proposed that coarser porous media, which have high wetting phase permeabilities, should have small t values because P_c-S equilibrium can be re-established more rapidly after a given dynamic event [Hassanizadeh *et al.*, 2002]. However, an opposite result from experimental measurements has been reported by Wildenschild, *et al.* [2001], who qualitatively observed larger dynamic capillary effects in P_c-S relationships for a coarser sand. As

such, how porous media properties influence dynamic capillary effects, and also the dynamic responses of porous media, remains unclear. More experimental examination is needed for porous media with wide range of properties and for different wetting/drying processes.

As such, the purpose of the work described in this chapter was to investigate the influence of porous media properties on the observed dynamic effects. Various porous media with different grain sizes ranging from fine sand to silt are used for this study.

4.2. MATERIALS AND METHODS

4.2.1. *Materials*

Three porous media obtained from U. S. Silica (Berkeley Springs, WV) were used in this research: fine sand F-95, ultra fine sand F-110 and silica silt SCS-250. Their mean grain sizes and porosities can be found in Table 4.1. Nanopure water was used as the wetting phase for F-95 and F-110 and 0.01 M $CaCl_2$ for SCS-250, as described in Chapter 2. Nitrogen gas was used as the non-wetting phase.

Saturated water conductivity (K_{SAT}, cm/s) of the porous media was measured using the constant head method [Fetter, 2001]. The pressure cell (Figure 2.2) was used as a short column, with porous stainless steel plates (20 µm pore size and 1.6 mm thickness, purchased from Mott Corp., Farmington, CT) and coarse fast flow filter papers (Fisher Scientific, Pittsburgh, PA) at both ends to hold the sample in place. Samples were packed fully saturated (see Chapter 2), and 20 pore volumes of water were pumped through the

cell before the start of experiments. Saturated conductivities of steel plates and filter papers were taken into account in calculating saturated conductivities of porous media. The saturated water conductivities measured for all porous media are listed in Table 4.1.

Table 4.1. Properties of Porous Media.*

Medium	n	d_{50} (μm)	K_{SAT} (cm/s)	l	p^d (cm H_2O)	S_{wr}
F-95	0.349 (±0.007)	140	2.22×10^{-3}	6.15	*Primary drainage*	
					59	0.140
					Main imbibition	
					53	0.136
					Secondary drainage	
					54	0.141
F-110	0.362 (±0.006)	120	1.47×10^{-3}	6.27	*Primary drainage*	
					71	0.142
					Main imbibition	
					61	0.160
					Secondary drainage	
					59	0.178
SCS-250	0.413 (±0.019)	45	1.62×10^{-4}	2.48	*Primary drainage*	
					245	0.188
					Secondary drainage	
					234	0.258

*Note: n: Porosity. Standard errors shown in parentheses.
d_{50}: Mean grain size.
K_{SAT}: Saturated conductivity.
l: Pore size distribution index.
p^d: Displacement pressure.
S_{wr}: Water residual saturation of the measured pseudo-static P_c-S curve.

The pore size distribution index (λ) of each medium and the displacement pressure (p^d) of primary drainage are determined by fitting Brooks-Corey equation [Brooks and Corey, 1966] (Equation 3.3) to the pseudo-static P_c-S curve as mentioned in Chapter 3, and results are shown in Figure 4.1. The good agreement between the measured and predicted P_c-S curves supports the application of Brooks-Corey equations for the porous media used in this research. For main imbibition and secondary drainage, p^d is taken as the capillary pressure where imbibition or drainage starts to occur significantly in the slowest (also pseudo-static) experiment. The obtained λ and p^d values for each drying or wetting process of each porous medium are listed in Table 4.1.

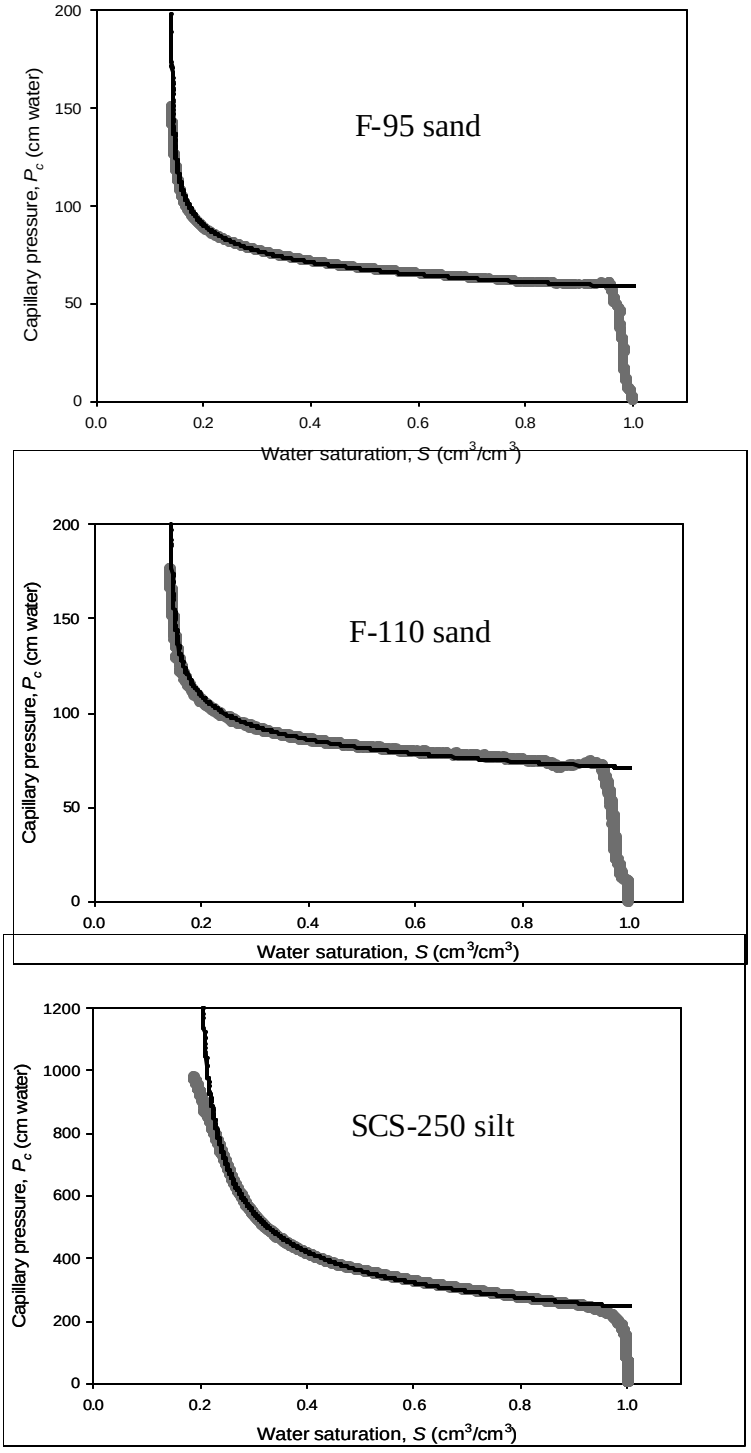


Figure 4.1. Brooks-Corey fit to the measured pseudo-static primary drainage P_c-S curves of different porous media. Gray symbols: measured curves; black lines: fit results. Data for F-95 are re-plotted from Figure 3.1 for comparison. Fit parameters in Brooks-Corey equation are listed in Table 4.1.

4.2.2. *Determination of Dynamic Coefficients*

The apparent dynamic coefficient (t^*), relative permeability (k_{rw}), and dynamic capillary coefficient (t) for F-110 sand and SCS-250 silt were determined using the same methods as described in Chapter 3. Primary drainage, main imbibition and secondary drainage were studied for F-110 sands, but only the two drainages were studied for silica silt SCS-250, since it is difficult to have the silt drain to the same residual saturation every time before the imbibition begins. Data and calculation for F-95 dynamic coefficients are given in Chapter 3.

Apparent dynamic P_c (P_c^{d*})-S relationships with different saturation rates ($\partial S/\partial t$), achieved by applying different gas phase pressure rates (dP_n/dt) were measured using the same method as described in Chapter 3. For each set of P_c^{d*}-S curves, at least one (the slowest) experiment was measured under pseudo-static conditions with dP_n/dt value small enough to produce an apparent dynamic P_c-S curve matching the static curve (0.042 cm water per second for F-110 and 0.070 cm water per second for SCS-250, Chapter 2).

At each saturation, at least four P_c^{d*}-S curves were used in regression to determine apparent dynamic coefficient t^* (Equation 3.13). As in Chapter 3, only the fraction of each P_c^{d*}-S curve with slope (dP_c^{d*}/dS) less than a specified threshold was used in regression to avoid the near vertical region of the curve, a region that is more vulnerable to error and where Equations 3.4 and 3.13 are not valid. For this chapter, slope threshold of 500 cm water was used for F-95 and F-110 and 1000 cm water was used for SCS-250.

The higher threshold was needed for SCS-250 because of higher displacement pressure and higher pressures used for drainage.

4.3. RESULTS AND DISCUSSION

4.3.1. *Primary Drainage Dynamic Coefficients of Different Porous Media*

Apparent Dynamic and Static Primary Drainage P_c-S Curves of F-110 and SCS-250. Six primary drainage P_c^{d*}-S curves of F-110 sand, measured with pressure rates ranging from dP_n/dt = 0.0084 to 0.42 cm water per second, are plotted in Figure 4.2. The corresponding time scales to finish each entire dynamic primary drainage curve is between 500 and 10 minutes. Four to six P_c^{d*}-S curves were used in regression to calculate t^* and static P_c, with fewer curves used at lower saturations, as indicated in Figure 4.2. Static P_c predicted from regression (dark gray symbols in Figure 4.2) exhibit good agreement with both the pseudo-static curves (apparent dynamic curves with $dP_n/dt \leq 0.042$ cm water per second) and P_c^S values independently measured in Chapter 2 (light gray symbols in Figure 4.2, re-plotted from Figure 2.6).

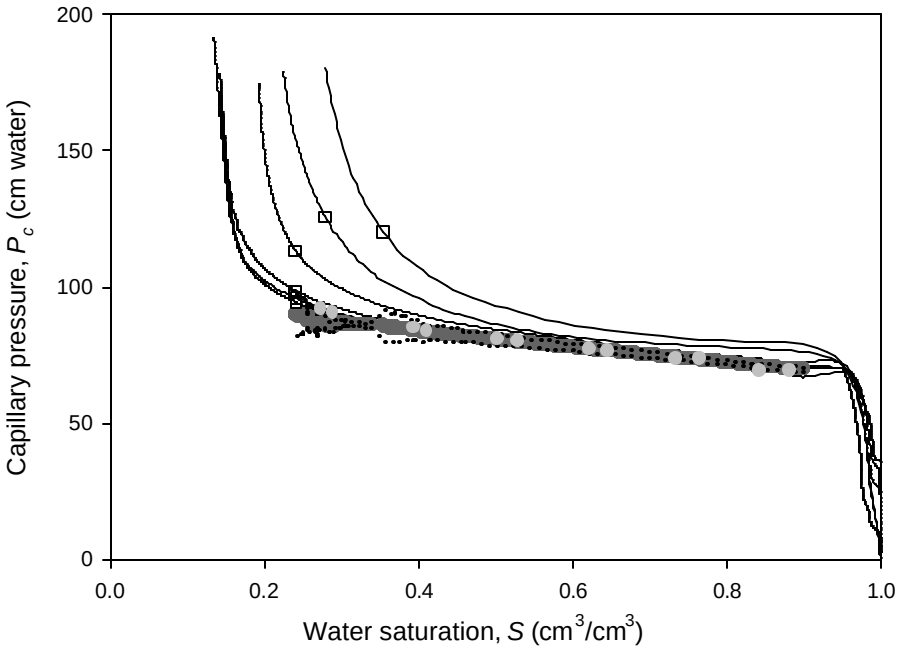


Figure 4.2. Primary drainage P_c-S curves of F-110 sand. Solid black lines: apparent dynamic curves measured at different pressure rates (0.42, 0.21, 0.084, 0.042, 0.0168, and 0.0084 cm water/sec from top to bottom curves, respectively); empty black square on each dynamic curve: lowest saturation used in calculation; dark gray symbols: predicted static curve; dotted black lines: standard error of the predicted static P_c from linear regression; light gray symbols: independently measured static P_c (re-plotted from Figure 2.6).

Eight SCS-250 primary drainage P_c^{d*}-S curves measured at different pressure rates are shown in Figure 4.3. The applied dP_n/dt values were between 0.042 and 0.84 cm water per second, and correspondingly 420 to 21 minutes were taken to finish each dynamic curve. Due to the fine nature of SCS-250 silt, relatively more variability would be expected in packing, leading to more variability in measured primary drainage P_c^{d*}-S curves. As shown in Figure 4.3, primary drainage P_c^{d*}-S curves of SCS-250 are influenced by packing in such a way that curves obtained at different rates cross each other instead of lying from top to bottom in decreasing order of drainage rates. One consequence of curve-crossing is that for the region from where crossing occurs down to

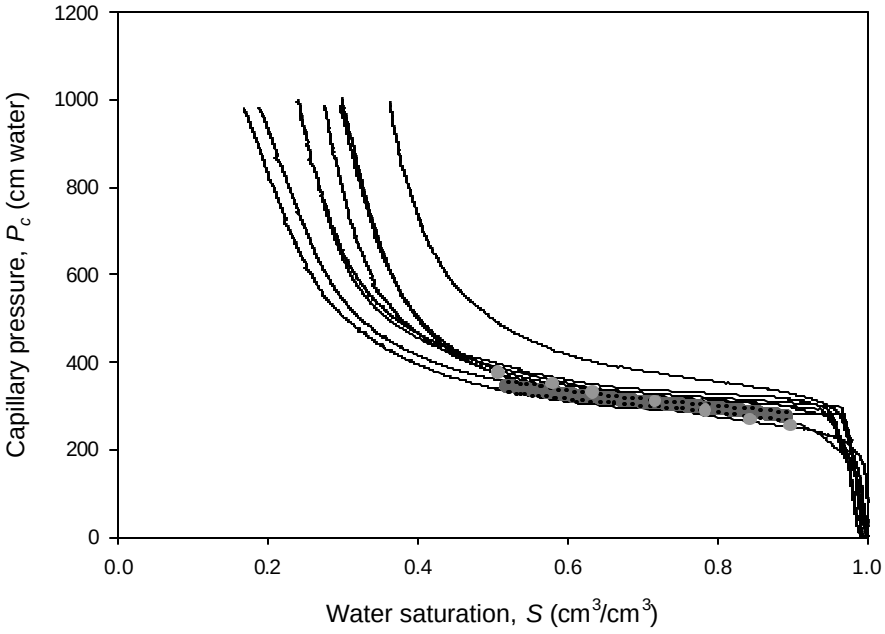


Figure 4.3. Primary drainage P_c-S curves of SCS-250 silt. Solid black lines: apparent dynamic curves measured at different pressure rates (0.84, 0.21, 0.105, 0.088, 0.084, 0.070, 0.052 and 0.042 cm water/sec, respectively); dark gray symbols: predicted static curve; dotted black lines: standard error of the predicted static P_c from linear regression; light gray symbols: independently measured static P_c (re-plotted from Figure 2.8A).

where the curves become too steep (*i.e.*, when $S < 0.5$), data are too scattered to fit a linear relationship between P_c^{d*} and $\partial S/\partial t$ (Equation 3.13). As such, regression was only carried out for higher saturations ($S = 0.5$ to 0.9). Figure 4.3 also shows that the P_c^s-S curve predicted from regression is in good agreement with both pseudo-static apparent dynamic curves and P_c^s values independently measured in Chapter 2 (light gray circles in Figure 4.3, re-plotted from Figure 2.8A).

Primary Drainage Apparent Dynamic Coefficient (t^*) of Different Porous Media. Primary drainage apparent dynamic coefficients (t^*) calculated for F-95, F-110 and SCS 250 are plotted in Figure 4.4, as a function of effective water saturation, S_e. All three t^*-S_e curves can be described by three-parameter power functions with negative exponents. Within the studied saturation range, similar t^* values are obtained for F-95 and F-110 while significantly higher (one to two orders of magnitude) t^* values are found for SCS-250 at the same saturations. This result illustrates that the magnitude of apparent dynamic coefficient is highly related to the properties of porous media, because F-95 and F-110 have similar properties significantly different from SCS-250. The difference in the magnitude of t^* between sand and silt implies that, as would be expected, sand responds much faster than silt to pressure change in the system.

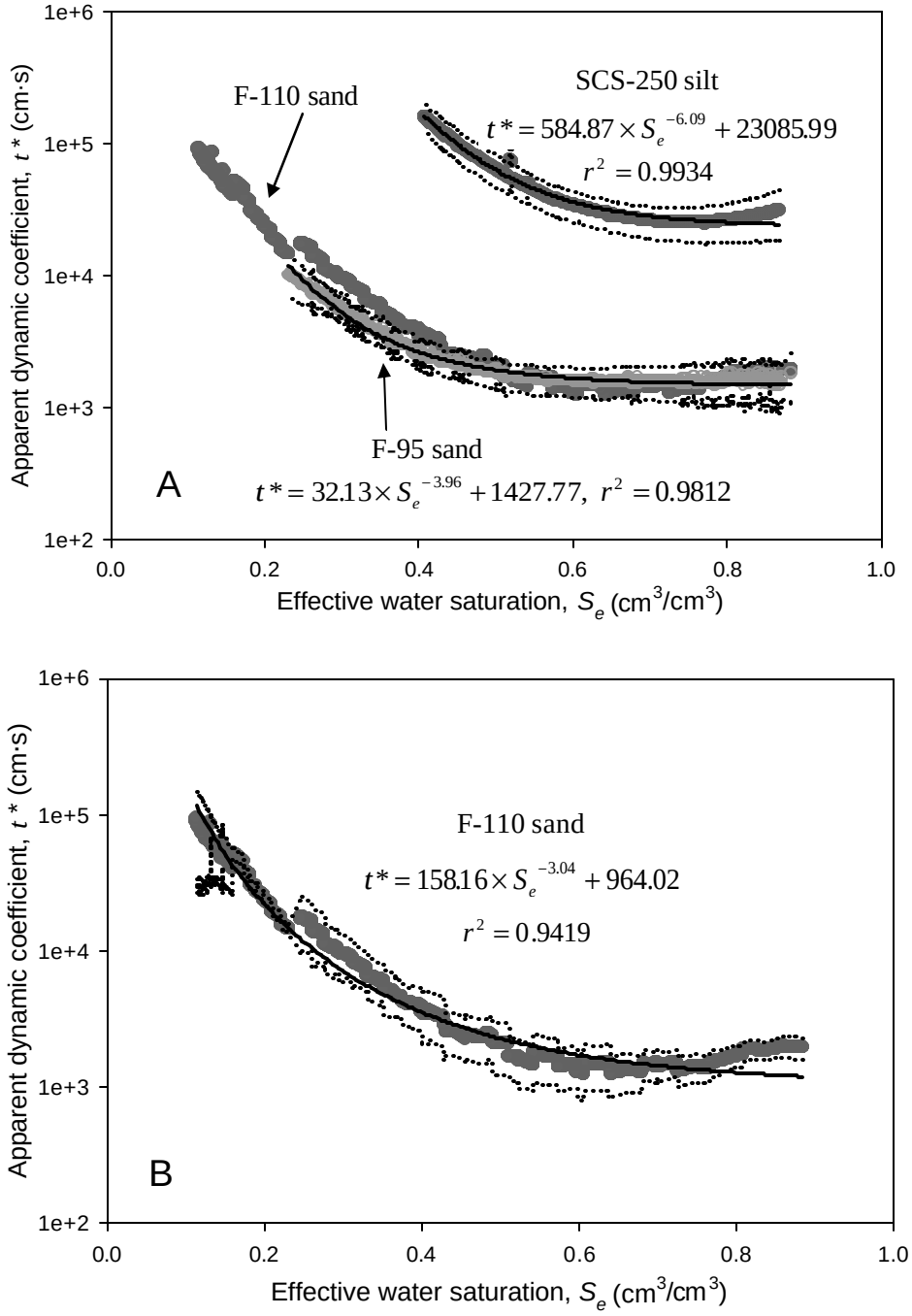


Figure 4.4. The relationship between apparent dynamic coefficient and water effective saturation for primary drainage of different porous media. Gray circles: measured values; solid black lines: power function fit results; dotted black lines: standard error of the measured value from linear regression at each saturation.. For clarity, experimental data for F-110 is re-plotted in Fig. B along with power function fit and standard error.

Primary Drainage Relative Permeability of Different Porous Media. Apparent dynamic coefficient (t^*) values calculated from P_c^{d*}-S curves include both relative permeability and dynamic capillary effects (Equation 3.13). To separate the two effects from each other, k_{rw} was calculated using Equation (3.14) by assuming t = 0 (expressed as $k_{rw}^{t=0}$), to compare with Brooks-Corey relative permeabilities (k_{rw}^{BC}, Equation 3.2). Results are shown in Figures 4.5 for F-110 sand and Figure 4.6 for SCS-250 silt. Figure 4.5 shows that when $S_e \leq 0.510$, the $k_{rw}^{t=0}$-S_e and k_{rw}^{BC}-S_e curves of F-110 sand match each other very well, indicating that in this low saturation region drainage flow of F-110 is mainly controlled by relative permeability. At high saturations ($S_e > 0.510$), the lower $k_{rw}^{t=0}$-S_e compared to the k_{rw}^{BC}-S_e curve indicates that dynamic capillary effect is a major factor influencing unsaturated flow. This finding is similar to the result for F-95 sand reported in Chapter 3 (e.g. Figure 3.9).

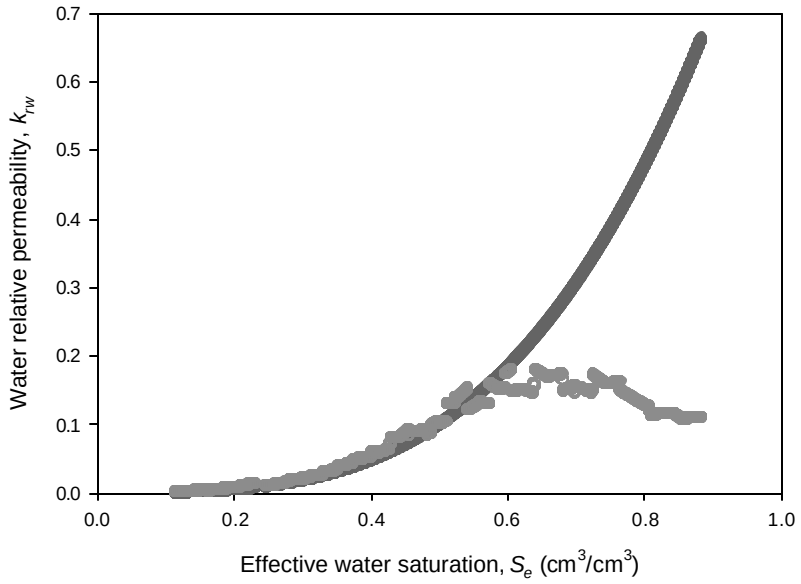


Figure 4.5. Water relative permeability of F-110 as a function of saturation. Dark gray: Brooks-Corey function; light gray: calculated at t = 0 for primary drainage.

Unlike F-95 and F-110, results for SCS-250 (Figure 4.6) show that the $k_{rw}^{t=0}$-S_e curve is lower than the k_{rw}^{BC}-S_e curve over the entire studied saturation range. There are two possible reasons for this observation. First, the study failed to go to a saturation range low enough where the relative permeability controls the flow. Second, the t^* values for SCS-250 primary drainage may have been overestimated at low saturations near where P_c^{d*}-S curves cross due to packing variability, and the overestimated t^* values result in the underestimated $k_{rw}^{t=0}$ (Equation 3.14). Note that similar to F-95 and F-110, the k_{rw}^{BC}-S_e curve for SCS-250 tends to level off at high saturations, indicating that dynamic capillary effects for the silt is also increasingly significant with the increasing saturation.

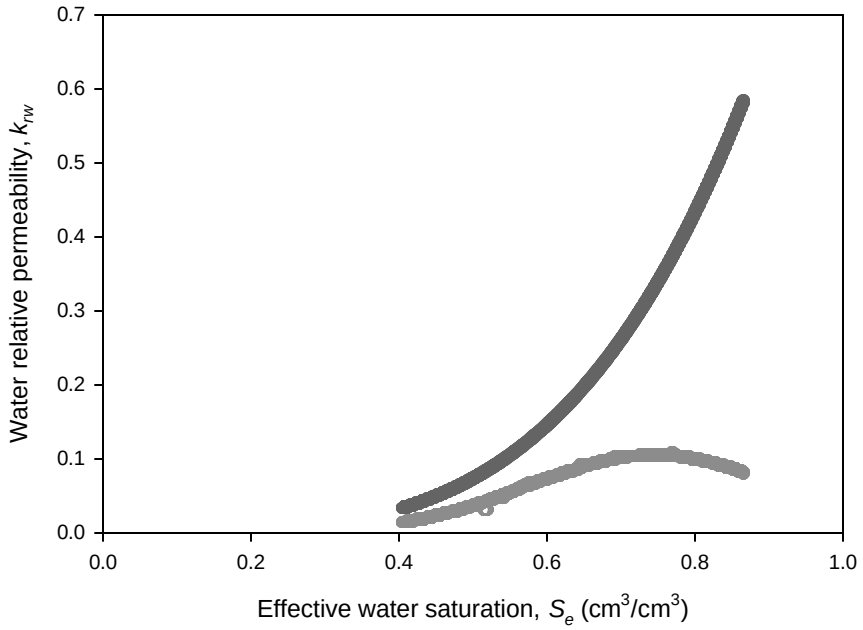


Figure 4.6. Water relative permeability of SCS-250 as a function of saturation. Dark gray: Brooks-Corey function; light gray: calculated at t = 0 for primary drainage.

For comparison, the k_{rw}-S_e curves for F-95, F-110 and SCS-250 are re-plotted in Figure 4.7. Reflecting the difference in the pore size distribution index (l) (Table 4.1), the k_{rw}^{BC}-S_e curves for F-95 and F-110 almost overlay each other while the k_{rw}^{BC}-S_e curve for SCS-250 is lower than the other two. The lower $k_{rw}^{t=0}$-S_e curve observed for F-95 compared to that for F-110 indicates that at the saturation region where dynamic capillary effects are significant, a larger dynamic capillary coefficient (t) should be observed for F-95.

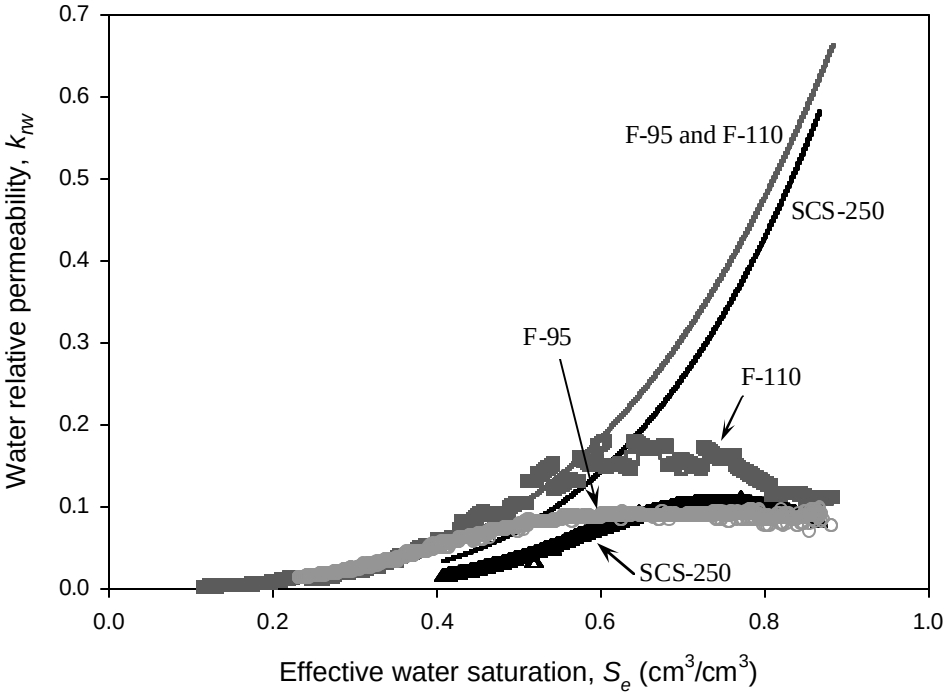


Figure 4.7. Comparison of water relative permeability functions of different porous media. Lines: Brooks-Corey function; symbols: calculated at t = 0 for primary drainage; light gray: F-95 sand; dark gray: F-110 sand; black: SCS-250 silt. Note that Brooks-Corey functions for F-95 and F-110 overlay each other.

Primary Drainage Dynamic Capillary Coefficient (t) for Different Porous Media. Primary drainage dynamic capillary coefficients (t) of F-110 and SCS-250 were calculated using Equation (3.15) for the region where the $k_{rw}^{t=0}$-S_e curve is lower than the corresponding k_{rw}^{BC}-S_e curve. Results are shown in Figure 4.8, along with the data for F-95 originally reported in Chapter 3. Figure 4.8 shows that although the magnitude of t calculated for F-110 jumps with saturation (due to the measured zigzag-shaped t^* at high saturations mainly caused by oscillation in collecting data for fast runs), the t-S_e curve still exhibits a general trend showing the decreasing t with the decreasing saturation, similar to F-95. Although the t values observed for F-110 and F-95 fall in the same

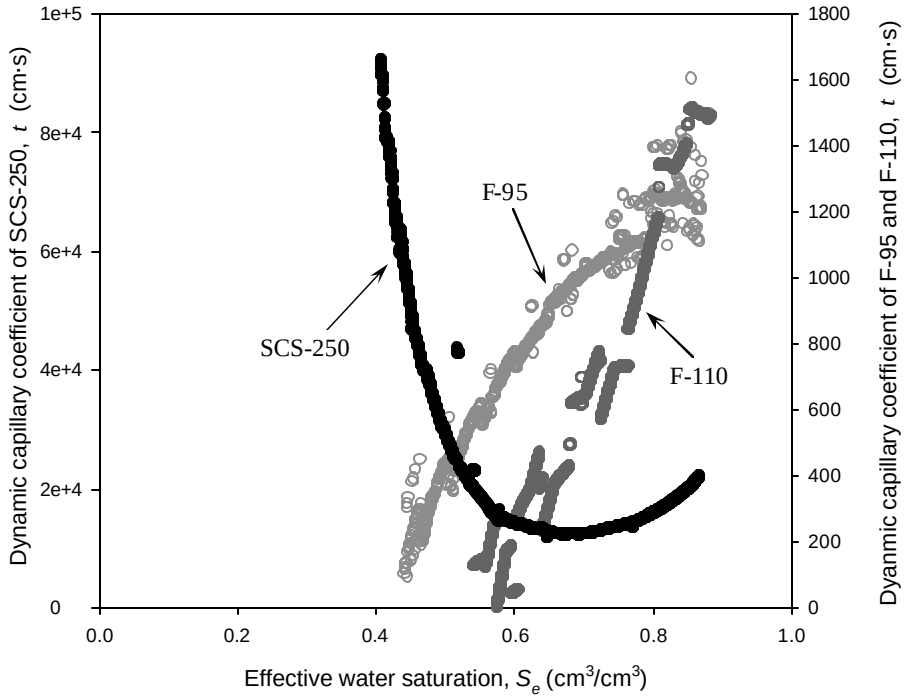


Figure 4.8. Comparison of dynamic capillary coefficients determined for F-95 (light gray), F-110 (dark gray) and SCS-250 (black) during primary drainage.

range, t for F-110 is significantly lower than t for F-95 over most of the saturation region covered in Figure 4.8. In addition, it is interesting to note that for both F-95 and F-110, the values of t at high saturations (where the calculation of t is most reliable) are approximately equal to the intercepts of the corresponding t^*-S_e curves (Figure 4.4) on the t^* axis at high saturation. This result is not surprising since it has been observed that the combined dynamic effects are mainly contributed by dynamic capillary effects at high saturations (Figure 4.7).

In contrast with the F-95 and F-110 t-S_e curves, the t-S_e curve obtained for SCS-250 primary drainage (Figure 4.8) shows a different relationship, with a minimum t observed over the studied saturation range. The overall magnitude of t for SCS-250 is higher than t for F-95 and F-110, for at least one order of magnitude. The steep increase of t with the decrease of saturation at low saturations suggests that t^* may indeed have been overestimated, as discussed earlier in the **Primary Drainage Relative Permeability of Different Porous Media** section, and calls into question the reliability of calculated t values for SCS-250 primary drainage at low saturations. However, at high saturations where the calculation of SCS-250 t is more reliable, t values are equivalent to the intercept of the corresponding t^*-S_e curve (Figure 4.4) on the t^* axis at high saturation, as was observed for F-95 and F-110.

4.3.2. *Main Imbibition Dynamic Coefficients of F-95 and F-110*

Apparent Dynamic and Static Main Imbibition P_c-S Curves of F-110. Figure 4.9 shows a total of nine main imbibition P_c^{d*}-S curves of F-110 sand, along with the corresponding preceding drainage curves. All preceding drainages were conducted under the same pseudo-static conditions, where a dP_n/dt value of 0.035 cm water per second was applied as the speed for the decrease of gas phase pressure, to ensure that the sand was drained to the same water residual saturation prior to the start of each subsequent main imbibition process. Nine imbibition P_c^{d*}-S curves were measured at dP_n/dt rates ranging from 0.035 to 1.05 cm water per second, corresponding to 120 to 4 minutes to complete each dynamic curve. The predicted static P_c-S curve shown in Figure 4.5 exhibits good agreement with the pseudo-static P_c-S curve.

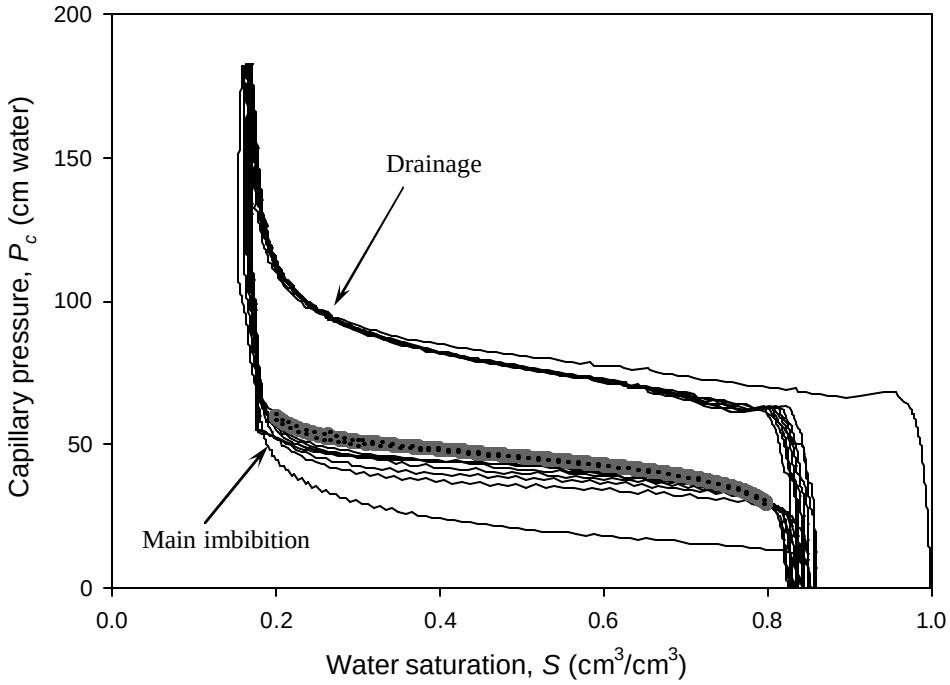


Figure 4.9. Main imbibition P_c-S curves of F-110 sand. Solid black lines: apparent dynamic imbibition curves measured at different pressure rates (0.035, 0.117, 0.131, 0.15, 0.175, 0.21, 0.263, 0.35, 1.05 cm water per second from top to bottom curves, respectively) with preceding drainage curves measured under constant pseudo-static conditions; gray symbols: predicted static curve; dotted black lines: standard error of static P_c when predicted from linear regression at each saturation.

Main Imbibition Apparent Dynamic Coefficients (t^*) of F-95 and F-110. Main imbibition apparent dynamic coefficients (t^*) calculated for F-110 sand are shown in Figure 4.10, along with data for F-95 (re-plotted from Figure 3.6) for comparison. Results show that t^* for both F-95 and F-110 increase gradually as a power function with the decrease of saturation within the most of studied saturation range, but with higher t^* values for F-110 at given saturations (2.1×10^3 to 6.5×10^4 cm·s for F-110 versus 7.9×10^2 to 2.5×10^3 cm·s for F-95). The difference in the magnitude of main imbibition t^* values between F-95 and F-110 indicates that finer porous media exhibit greater dynamic effects, which is consistent with the observation for primary drainage (Figure 4.4).

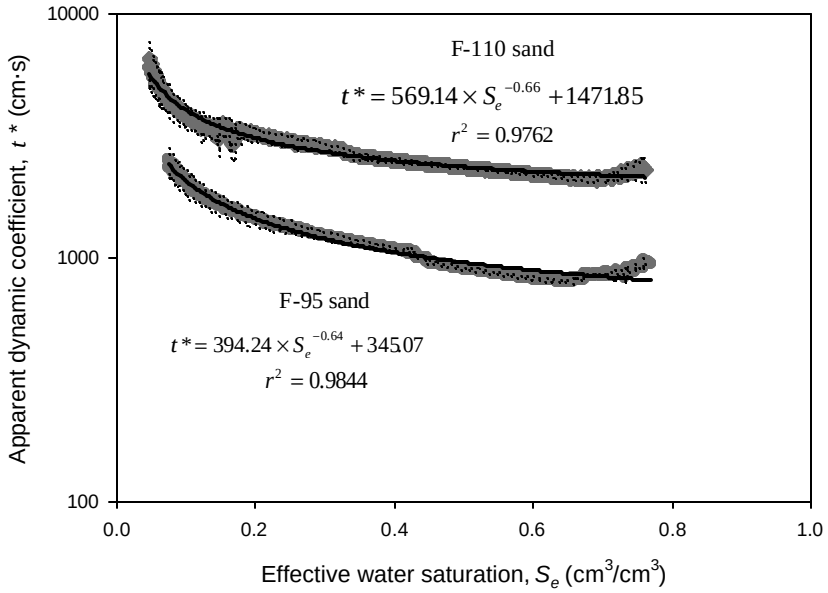


Figure 4.10. The relationship between apparent dynamic coefficient and water effective saturation for main imbibition of F-95 and F-110 sands. Gray symbols: measured values; solid black line: power function fit result; dotted black lines: standard error of the measured dynamic coefficient from linear regression at each saturation.

Main Imbibition Relative Permeability (k_{rw}) of F-95 and F-110. Figure 4.11 illustrates that similar to what was observed for F-95 in Chapter 3, the main imbibition $k_{rw}^{t=0}$-S_e curve of F-110 is also significantly higher than the k_{rw}^{BC}-S_e curve at low saturations. The result once again demonstrates that the relative permeability exhibited during imbibition is likely significantly higher than that exhibited during drainage or under equilibrium conditions. Because the $k_{rw}^{t=0}$-S_e curve of F-110 is lower than that of F-95, it is very likely that the dynamic capillary coefficient (t) of F-110 is higher than that of F-95 during main imbibition, especially at high saturations, assuming the relative permeability functions for the two sand samples are also similar during imbibition, like during drainage. (As in Chapter 3, it is not possible to estimate t during imbibition, because the measured $k_{rw}^{t=0}$ is greater than k_{rw}^{BC}.)

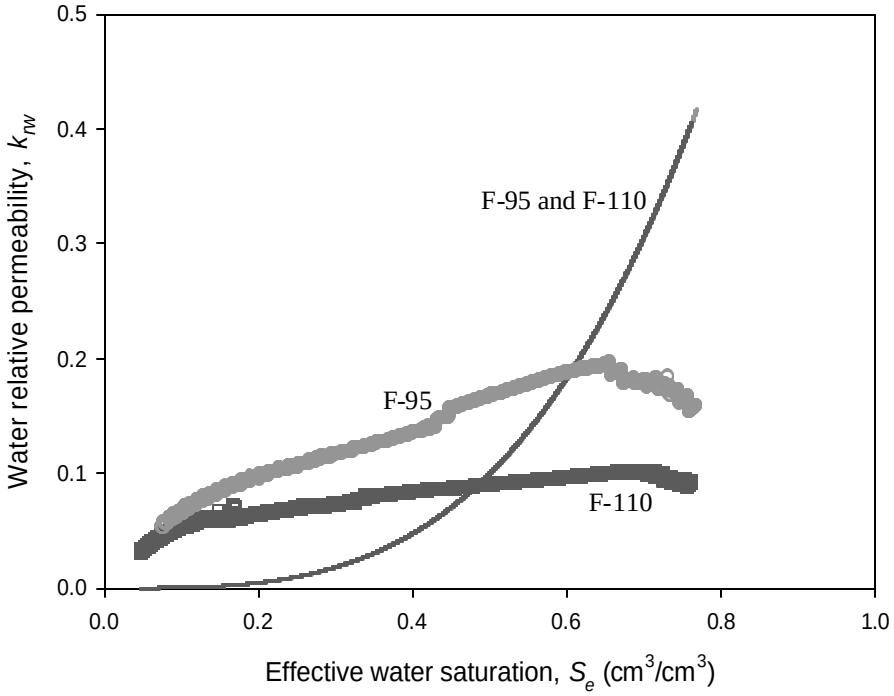


Figure 4.11. Comparison of water relative permeability functions of different porous media. Lines: Brooks-Corey function; symbols: calculated at $t = 0$ for main imbibition; light gray: F-95 sand; dark gray: F-110 sand. Note that Brooks-Corey functions for F-95 and F-110 overlay each other.

4.3.3. *Secondary Drainage Dynamic Coefficients of Different Porous Media*

Apparent Dynamic and Static Secondary Drainage P_c-S Curves of F-110 and SCS-250. Figure 4.12 shows eight secondary drainage P_c^{d*}-S curves of F-110 sand, measured at pressure rates ranging from 0.042 to 0.84 cm water per second (corresponding to 100 to 5 minutes to finish each dynamic P_c-S curve), and also the static P_c-S curve predicted from regression. Results show that P_c^s values were well predicted over most of the covered saturation range, except for the region with $S < 0.35$.

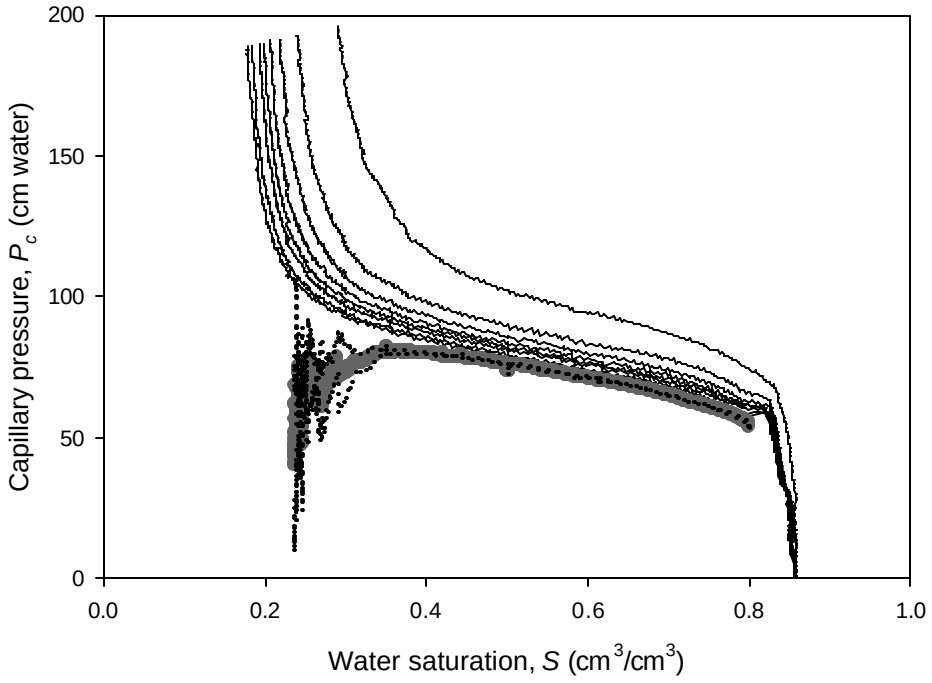


Figure 4.12. Secondary drainage P_c-S curves of F-110 sand. Solid black lines: apparent dynamic curves measured at different pressure rates (0.84, 0.21, 0.105, 0.088, 0.084, 0.070, 0.052 and 0.042 cm water/sec, respectively); dark gray symbols: predicted static curve; dotted black lines: standard error of the predicted static P_c from linear regression.

Figure 4.13 shows four apparent dynamic secondary drainage P_c-S curves of SCS-250 silt measured at dP_n/dt values ranging from 0.070 to 0.21 cm water per second, which correspond to time scales ranging from 200 to 67 minutes to complete each dynamic curve. Figure 4.13 also shows that the static secondary drainage P_c-S curve is well-predicted from regression over the covered saturation range.

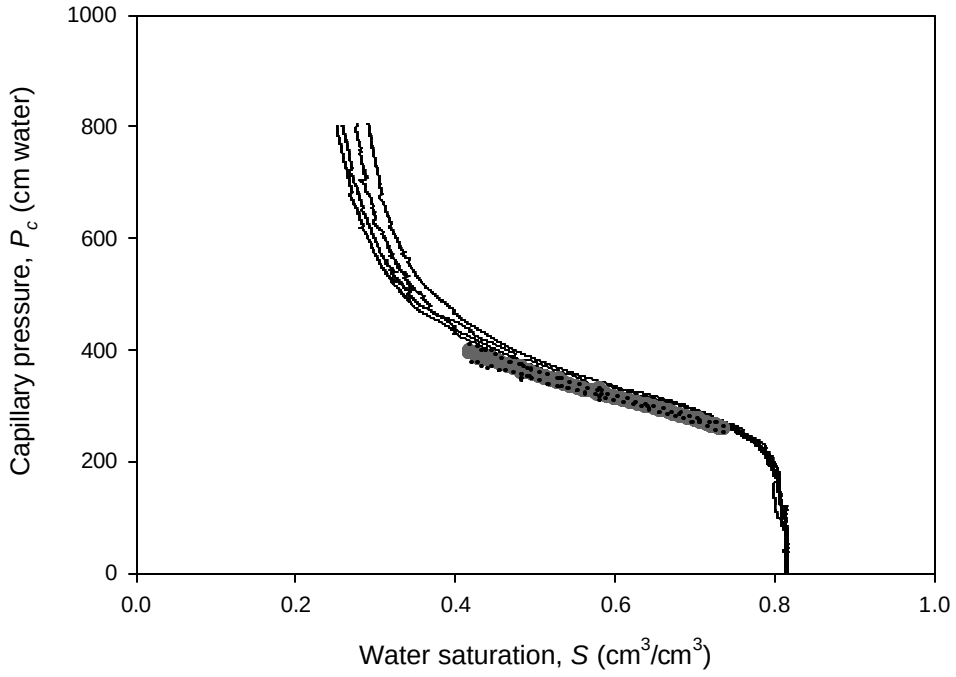


Figure 4.13. Secondary drainage P_c-S curves of SCS-250 silt. Solid black lines: apparent dynamic curves measured at different pressure rates (0.21, 0.14, 0.105, and 0.070 cm water/sec, respectively); dark gray symbols: predicted static curve; dotted black lines: standard error of the predicted static P_c from linear regression.

Secondary Drainage Apparent Dynamic Coefficient (t^*) of Different Porous Media. Secondary drainage apparent dynamic coefficients (t^*) calculated for F-95, F-110 and SCS 250 are plotted as a function of S_e in Figure 4.14. Once again, all of three obtained t^*-S_e curves can be well described by three-parameter power functions with negative exponents. Similar to the observation with primary drainage (Figure 4.4), secondary drainage t^* values for SCS-250 are significantly higher than those obtained for F-95 and F-110 at the same saturations. In addition, higher t^* values are found for F-110 than F-95. In general, Figure 4.14 clearly shows the strong dependence of t^* on porous media properties, with higher t^* values for finer media.

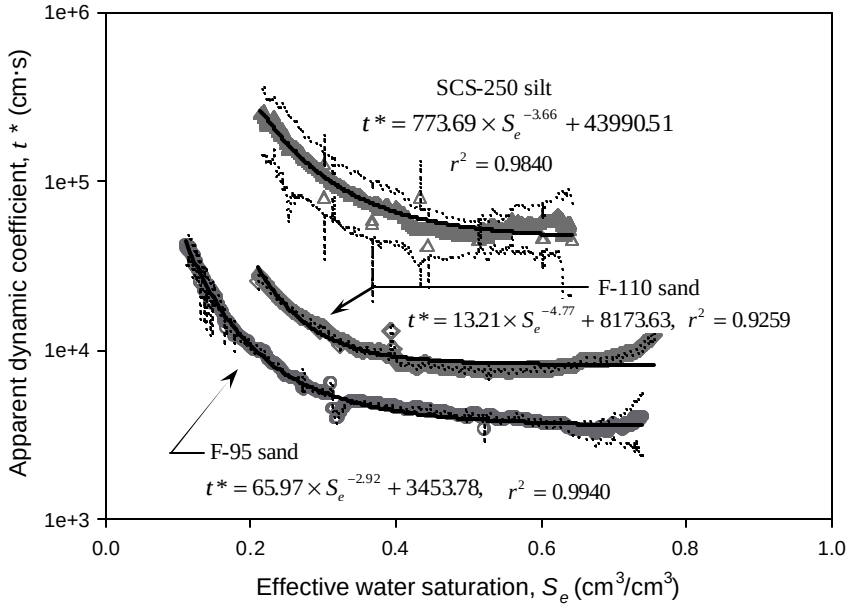


Figure 4.14. The relationship between apparent dynamic coefficient and water effective saturation for secondary drainage of different porous media. Gray symbols: measured values; solid black lines: power function fit results; dotted black lines: standard error of the measured dynamic coefficient from linear regression at each saturation.

Secondary Drainage Relative Permeability of Different Porous Media. To separate relative permeability from dynamic capillary effects, k_{rw} was calculated using Equation (3.14) by assuming $t = 0$. Results are shown in Figures 4.15 and 4.16 for F-110 and SCS-250, respectively. Figure 4.15 shows that the F-110 secondary drainage $k_{rw}^{t=0}$-S_e curve matches the k_{rw}^{BC}-S_e curve only at very low saturations (S_e = 0.270). At higher saturations, $k_{rw}^{t=0}$-S_e curve levels off and is significantly lower than the k_{rw}^{BC}-S_e curve. Similar findings are observed for SCS-250 (Figure 4.16). Although the $k_{rw}^{t=0}$-S_e curve of SCS-250 is slightly higher than the k_{rw}^{BC}-S_e curve, the two k_{rw}-S_e curves are considered to be quite close for the saturation region with $S_e \leq 0.444$, considering the large standard error in t^* for SCS-250 (Figure 4.14).

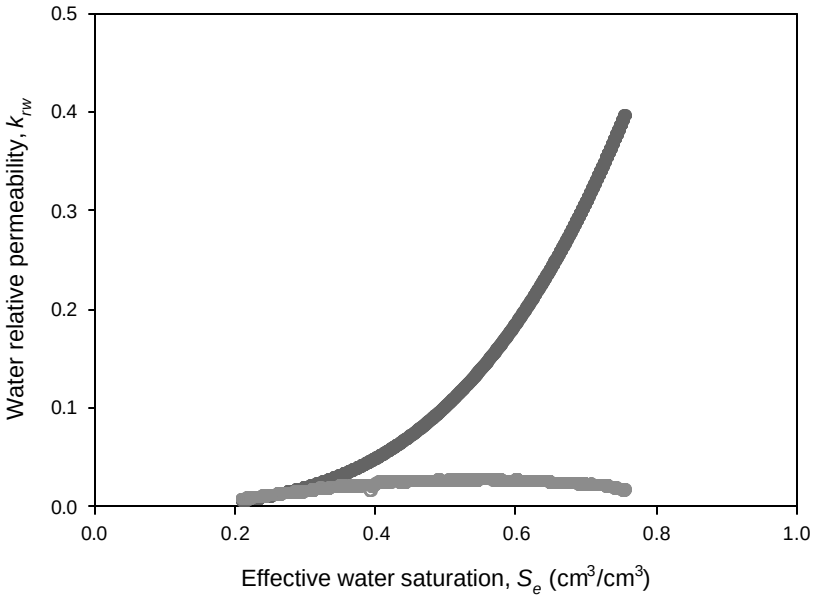


Figure 4.15. Water relative permeability of F-110 sand as a function of saturation. Dark gray: Brooks-Corey function; light gray: calculated at t = 0 for secondary drainage.

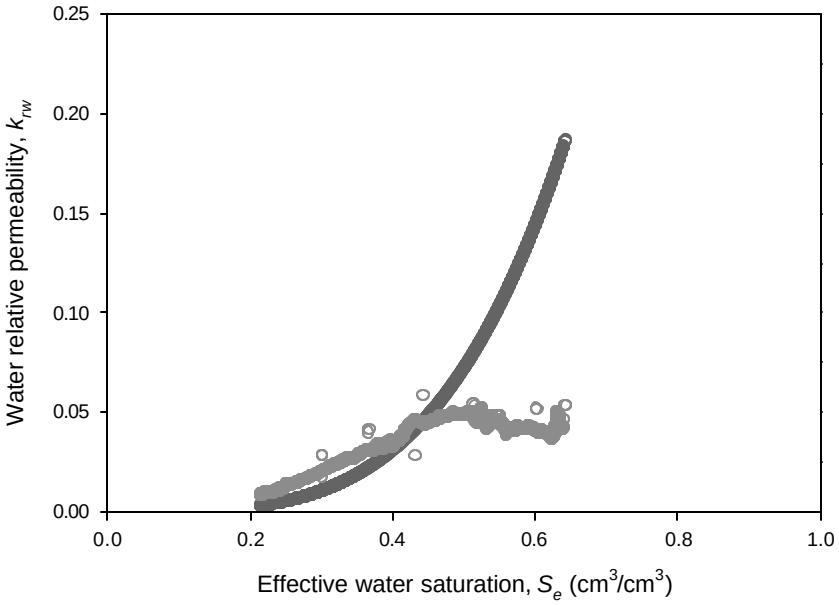


Figure 4.16. Water relative permeability of SCS-250 silt as a function of saturation. Dark gray: Brooks-Corey function; light gray: calculated at t = 0 for secondary drainage.

Figure 4.17 shows the comparison of $k_{rw}^{t=0}$-S_e curves obtained for secondary drainage of F-95, F-110 and SCS-250, and k_{rw}^{BC}-S_e curves for each of porous media. The $k_{rw}^{t=0}$-S_e curve observed for F-110 is lower than that for F-95, indicating higher dynamic capillary coefficients (t) for F-110 than F-95.

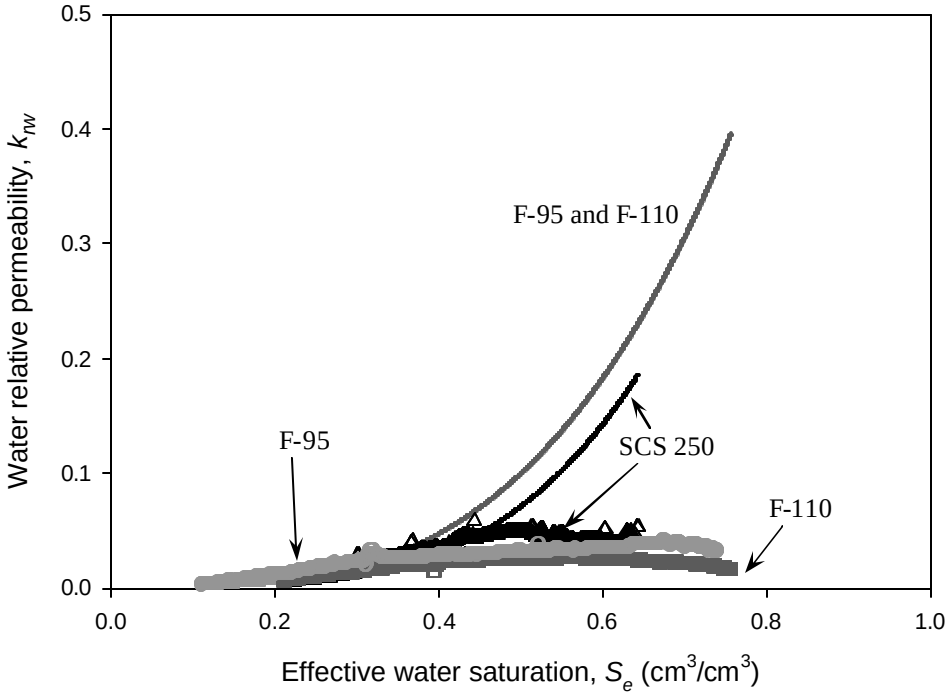


Figure 4.17. Comparison of water relative permeability functions of different porous media. Lines: Brooks-Corey function; symbols: calculated at $\tau = 0$ for secondary drainage; light gray: F-95 sand; dark gray: F-110 sand; black: SCS-250 silt. Note that Brooks-Corey functions for F-95 and F-110 overlay each other.

Secondary Drainage Dynamic Capillary Coefficient (t) for Different Porous Media. Secondary drainage dynamic coefficients (t) of F-110 and SCS-250 were calculated using Equation (3.15) for the saturation region where the $k_{rw}^{t=0}$-S_e curve is lower than the corresponding k_{rw}^{BC}-S_e curve. Results are shown in Figure 4.18, along with the data for F-95 originally reported in Chapter 3. In general, t for each medium decreases as saturation decreases. More specifically speaking, the t-S_e relationship for F-110 is very similar to that for F-95, and t gradually decreases with saturation. In contrast, the decrease of t with saturation for SCS-250 is much steeper. The maximum observed secondary drainage t is approximately 4.4×10^4 cm·s for SCS-250 silt and 1.2×10^4 cm·s for F-110 sand, compared to 3500 cm·s for F-95. Figure 4.18 illustrates the dependence of t on porous media properties, with higher t values observed for finer media in most cases. In addition, the t value observed for each medium at high saturation is approximately equal to the intercept of the corresponding t^*-S_e curve (Figure 4.14) on the axis of t^* at high saturation.

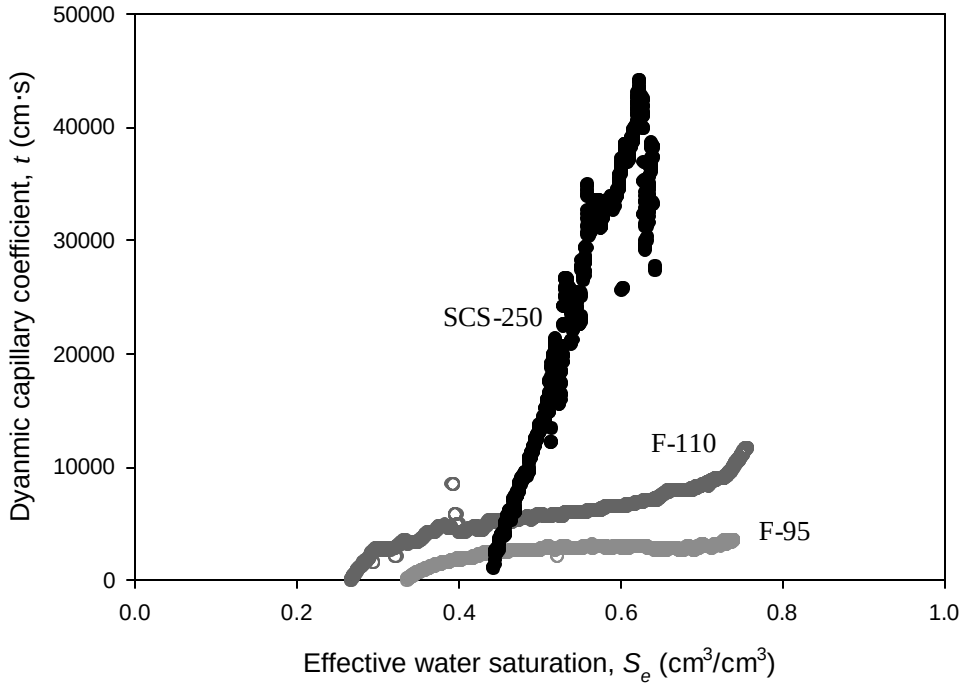


Figure 4.18. Comparison of dynamic capillary coefficients determined for F-95 (light gray), F-110 (dark gray), and SCS-250 (black) during secondary drainage.

4.3.4. *Estimation of Dynamic Capillary Coefficient (τ) from Porous Media Properties*

Through a series of experimental measurements on primary drainage of two similar sand samples, Stauffer [1978] proposed an equation to estimate the dynamic capillary coefficient, τ (cm·s), from the properties of porous media and fluids:

$$\tau = \frac{an}{K_{SAT}\, l}\left(p^d\right)^2 \qquad (4.1)$$

where a equals to 0.1 for all soils, n, l, p^d, and K_{SAT} are porosity, pore-size distribution index, displacement pressure (cm), and wetting phase saturated conductivity (cm/s) of porous media, respectively. Although the saturation dependence of τ is not considered in Equation (4.1), the equation indicates that for a given wetting/nonwetting system, finer porous media should have higher τ values since finer porous media have higher displacement pressure and lower conductivity.

Assuming Equation (4.1) applies for both primary and secondary drainages, τ can be estimated for all three porous media studied here (Table 4.2). Table 4.2 also lists the τ values obtained here to test the applicability of Equation (4.1). Because the τ values calculated herein vary with saturation, the τ value at a specific saturation near the high end of the studied saturation range (S_e = 0.8 for primary drainage and S_e = 0.6 for secondary drainage) was chosen for each experiment. The chosen τ values are also near the calculated maximum τ values. Standard errors for the calculated τ values shown in Table 4.2 are from standard errors in apparent dynamic coefficient (τ^*) from regression. Standard errors for τ are typically within 20 to 40% for F-95 and F-110 primary drainage, 2 to 5% for F-95 and F-110 secondary drainage, and around 50% for SCS-250. In

addition, as it has been discussed, t values at high saturations are approximately equal to the intercepts of the corresponding t^*-S_e curves on the t^* axis at high saturations. These intercepts can be approximated by the constants in the three-parameter power functions describing t^*-S_e relationships. As such, the constants in the t^*-S_e power functions are also listed in Table 4.2 for comparison.

Table 4.2. Comparison of Dynamic Capillary Coefficients estimated from the Stauffer Equation and from the Described Experiments.

	Porous medium	Dynamic capillary coefficient, t (cm·s)		Intercept of t^*-S_e curve (cm·s)
		Estimated from Stauffer equation (Eqn. 4.1)	Calculated from t^* and k_{rw}^{BC} at a specific saturation [a]	
Primary drainage	F-95 sand	8.9×10^3	$1.4\times10^3 \pm 5.7\times10^2$	1.4×10^3
	F-110 sand	2.0×10^4	$1.1\times10^3 \pm 3.1\times10^2$	9.6×10^2
	SCS-250 silt	6.2×10^6	$1.6\times10^4 \pm 8.6\times10^3$	2.3×10^4
Secondary drainage	F-95 sand	7.5×10^3	$2.9\times10^3 \pm 1.5\times10^2$	3.4×10^3
	F-110 sand	1.4×10^4	$6.5\times10^3 \pm 1.6\times10^2$	8.2×10^3
	SCS-250 silt	5.6×10^6	$3.6\times10^4 \pm 1.7\times10^4$	4.4×10^4

a: Values were determined at $S_e = 0.8$ for primary drainage, and $S_e = 0.6$ for secondary drainage. Standard errors are from standard errors in apparent dynamic coefficient (t^*) measurements only.

Results listed in Table 4.2 show that for most F-95 and F-110 experiments, the t values estimated from Equation (4.1) are within approximately an order of magnitude of the values calculated here. But for SCS-250, the t values estimated from Equation (4.1)

are two orders of magnitude higher than the values found in this research. These results indicate that the Equation (4.1), obtained from dimensional analysis based on studies on two similar coarse sand samples ($d_{50} \approx 300$ μm and $\lambda = 4.0$ to 6.5), may provide reasonable estimates of t for similar sand samples but not necessarily for porous media as fine as silt. In contrast, the intercept of the t^*-S_e curve on the t^* axis at high saturation provides a close estimate of t for both sand and silt (Table 4.2), with estimation error typically within 20% of the calculated t value except for SCC-250 primary drainage, where the estimation is about 44%. The error found in t estimation using the intercept of t^*-S_e curve is within the standard error of calculated t listed in Table 4.2.

As such, t for both sand and silt at high saturation can be estimated as the intercept of the t^*-S_e curve on the t^* axis at high saturation. If Equation (4.1) is a good description of the dependence of t on porous media properties, the plot of $t^* \times \frac{K_{SAT}\, l}{n\left(p^d\right)^2}$ versus S_e should have the same intercept for all porous media on the axis of $t^* \times \frac{K_{SAT}\, l}{n\left(p^d\right)^2}$ at high saturations. An example plot for secondary drainage of three porous media used here is shown in Figure 4.19.

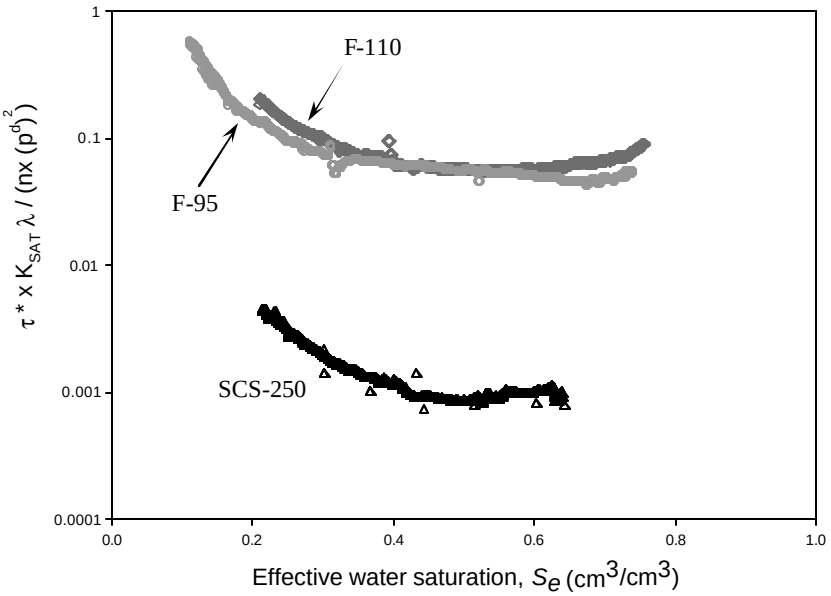


Figure 4.19. Secondary drainage t^*-S_e curves of different porous media scaled to the Stauffer equation. Light gray: F-95 sand; dark gray: F-110 sand; black: SCS-250 silt.

Figure 4.19 shows that F-95 and F-110 have similar intercepts on the axis of $t^* \times \frac{K_{SAT}\, l}{n\left(p^d\right)^2}$ at high saturation, but the intercept for SCS-250 is approximately two orders of magnitude lower. This result once again indicates that Equation (4.1) is not good in describing the dependence of t on the porous media properties, for a wide range of porous media with significantly different properties.

Further analysis of t^* data shows that t^* values for the three porous media are approximately inversely proportional to the saturated conductivity (K_{SAT}) of each medium. That is, when $t^* \times K_{SAT}$ is plotted verses S_e, the three curves are grouped together closely. Figure 4.20 shows the scaling result for primary drainage, main imbibition, and secondary drainage.

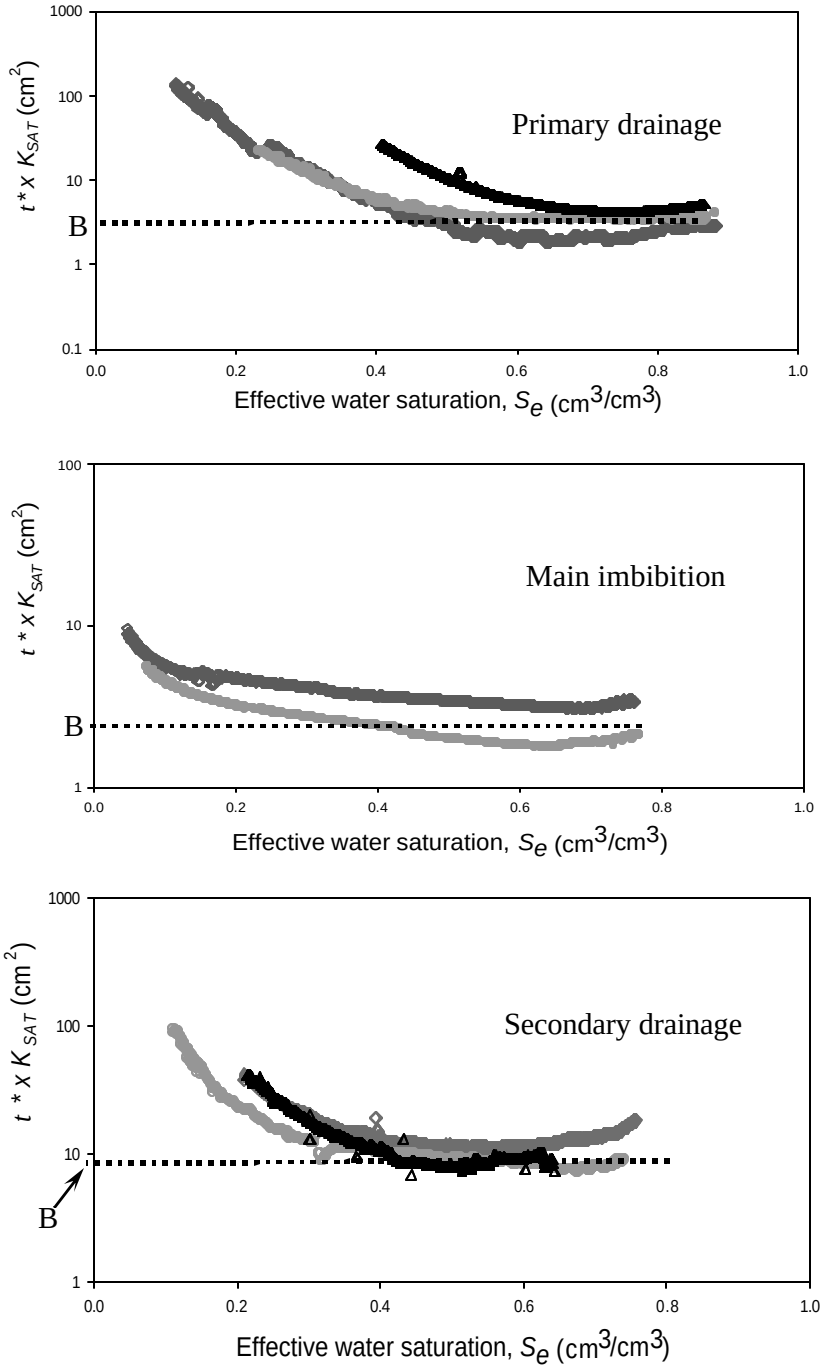


Figure 4.20. The plot of $t^* \times K_{SAT}$ versus S_e showing the similar intercept of the curves for different porous media during a particular drainage or imbibition. The black dotted line in each figure shows the estimated intercept (B) applicable for different porous media during a particular drainage or imbibition. Light gray: F-95; dark gray: F-110; black: SCS-250.

Figure 4.20 shows that for each drying/wetting process, $t^* \times K_{SAT}$ verses S_e curves for three porous media are grouped closely and have similar intercepts (B) on the axis of $t^* \times K_{SAT}$ at high saturation, and B represents an estimate for the value of $t \times K_{SAT}$ at high saturation for different porous media:

$$t \times K_{SAT} = B \qquad (4.2)$$

Equation (4.2) may be valid for various porous media ranging from sands to silts, with B varying with different drying/wetting processes. The estimated B for each drying/wetting process studied here, and t values estimated from Equation (4.2) are listed in Table 4.3. Results show that t values estimated from empirical Equation (4.2) are in good agreement with t values previously calculated from t^* and k_{rw}^{BC} at high saturation. It is further shown that the t values for main imbibition that can not be calculated from t^* and k_{rw}^{BC}, can be estimated from Equation (4.2). The dynamic capillary coefficients (t) estimated for main imbibition are slightly lower than the corresponding t values for primary drainage.

Table 4.3. The Intercepts (B) of $t^* \times K_{SAT}$ versus S_e Plots on the Axis of $t^* \times K_{SAT}$ at High Saturation and t Values Estimated from Equation (4.2).

	Intercept, B (cm^2)	Porous medium	Dynamic capillary coefficient, t (cm·s)	
			Estimated from Equation (4.2)	Calculated from t^* and k_{rw}^{BC} [a]
Primary drainage	3.5	F-95 sand	1.6×10^3	$1.4 \times 10^3 \pm 5.7 \times 10^2$
		F-110 sand	2.4×10^3	$1.1 \times 10^3 \pm 3.1 \times 10^2$
		SCS-250 silt	2.2×10^4	$1.6 \times 10^4 \pm 8.6 \times 10^3$
Main imbibition	2.5	F-95 sand	1.1×10^3	N/A
		F-110 sand	1.7×10^3	N/A
		SCS-250 silt	1.5×10^4	N/A
Secondary drainage	8.5	F-95 sand	3.8×10^3	$2.9 \times 10^3 \pm 1.5 \times 10^2$
		F-110 sand	5.8×10^3	$6.5 \times 10^3 \pm 1.6 \times 10^2$
		SCS-250 silt	5.2×10^4	$3.6 \times 10^4 \pm 1.7 \times 10^4$

a: Values presented here are the same as those shown in Table 4.2. N/A: not available.

4.4. CONCLUSIONS

In this chapter, the influence of porous media properties on the magnitudes of the apparent dynamic coefficient (t^*) and the dynamic capillary coefficient (t) was examined as a function of effective water saturation (S_e). Three porous media ranging from fine sand to silt were used for study during primary drainage, main imbibition, and secondary drainage. In general, higher dynamic coefficients (including both t^* and t) were observed

for finer porous media at a particular saturation. It was observed that the t values calculated at high saturations (where the calculation of t is most reliable) are approximately equal to the intercepts of the t^*-S_e curves on the t^* axis at high saturation, for all three porous media for both primary and secondary drainages. It was further found that for all three porous media studied here, the product of t (at high saturation) and saturated conductivity (K_{SAT}) is approximately a constant, for a particular drying/wetting process. As such, the t for any given porous media can be reasonably estimated with the known K_{SAT} information.

In this chapter, the applicability of the Stauffer equation (Equation 4.1) [Stauffer, 1978], the only equation available in the literature that describes the determination of t from the porous media properties, was also tested. Results show that the Stauffer equation can reasonably estimate t values for sand samples, but that it does not work well for silt.

Chapter 5

Three Dimensional Capillary Pressure-Saturation-Interfacial Area (P_c-S-A) Relationships: Measurement and Hysteresis

5.1. INTRODUCTION

The interface formed between two immiscible fluids in porous media not only plays an important role in many physical and chemical processes, such as multiphase flow, dissolution, volatilization, interfacial adsorption and accumulation [e.g. Miller, *et al*., 1990; Hassanizadeh and Gray, 1993; Imhoff, *et al*., 1993; Brusseau, *et al*., 1997; Kim, *et al*., 1998], but it also determines the feasibility of technologies to remediate the contamination of nonaqueous phase liquid (NAPL) in the subsurface, such as soil vapor extraction [Hoeg, *et al*., 2004] and pump and treat [Rubin, et al., 2004] methods. The air-water interface in the unsaturated zone can retard the transport of surface-active contaminants, such as organic compounds, colloids and microbes [e.g. Wan and Wilson, 1994; Kim, *et al*., 1998; Sim and Chrysikopoulos, 2000]. It is widely recognized that the quantitative determination of interfacial areas is critical in understanding contaminant distribution, transport and mass transfer among immiscible phases. However, before experimental techniques started to become available in the 1990s, the estimation of interfacial areas relied on model simulations [e.g. Hassanizadeh and Gray, 1993; Cary, 1994; Reeves and Celia, 1996; Muccino, *et al*., 1998].

The measurement of interfacial area was first reported by Karkare and Fort [1996], making use of water-insoluble surfactant as an interfacial tracer. Later, aqueous

[Kim, *et al*., 1997; Saripalli, *et al*., 1997; Anwar, *et al*., 2000; Schaefer, *et al*., 2000] and gaseous [Kim, *et al*., 1999b; Costanza-Robinson and Brusseau, 2002; Peng and Brusseau, 2005] interfacial tracer methods, and X-ray microtomography techniques [Culligan, *et al*., 2004; 2006] were proposed and applied to determine air-water or nonaqueous phase liquid-water interfacial areas at various water saturation conditions. In general, different methods have often provided different results due to the different ability of each type of tracer to access the generated interfaces, and different techniques used to control water saturation.

While all of the previously reported methods provide information about interfacial area as a function of saturation, the relationship between interfacial area and saturation is not expected to be unique, since numerous distributions and configurations of pore water can correspond to a particular saturation. In fact, the interfacial area-saturation relationship is complicated by the well-recognized hysteresis in the capillary pressure-saturation (P_c-S) relationship [Reeves and Celia, 1996], a constitutive characteristic of porous media describing the release/retention of pore water during drainage (drying)/imbibition (wetting) processes. How the drying/wetting history influences interfacial area is of theoretical interest to improve the quantitative understanding of the multiphase flow and mass transfer among phases in the unsaturated zone. Although recent studies have examined this question in 2D micro-model [Cheng, *et al*., 2004], experiments using existing methods to examine the effects of drying/wetting history on the interfacial area of natural porous media would be extremely difficult. More detailed review about the application, advantage and disadvantage of published

techniques for interfacial area measurement is given in the ***Experimental Measurements of Interfacial Area*** section (**Section 5.1.2**).

5.1.1. *Relationships between Interfacial Area and Saturation*

While it is known that the fluid-fluid interfacial area (A) is a function of saturation (S), two different types of functional relationships between the two parameters have been presented by researchers through modeling analysis (Figure 5.1). The relationship with an inverted parabolic shape (curve a, Figure 5.1) is observed when thin water films covering soil grains are ignored in modeling analysis [Gvirtzman and Roberts, 1991; Reeves and Celia, 1996; Held and Celia, 2001]. In this situation, interfacial area is only contributed by those fluid-fluid interfaces generated by capillary processes. The observed maximum interfacial area is ascribed to the maximum amount of pendular rings present in the system, which is proposed to be a significant contribution to the interface caused by capillarity [Gvirtzman and Roberts, 1991]. When water films are ignored, water saturation is observed to be zero at the end of drainage, causing a zero interfacial area due to the disappearance of water phase.

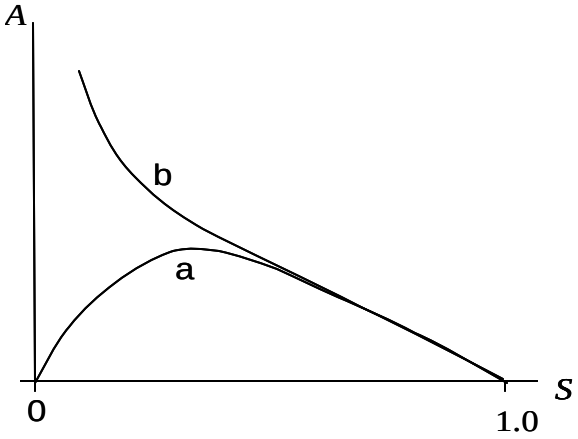


Figure 5.1. Proposed relationships between interfacial area (A) and water saturation (S) when water films adsorbed to grains are ignored (a) or considered (b).

When both capillary interfaces and water films adsorbed to the solid phase are incorporated in modeling simulations, the relationship is characterized by a monotonic

increase of interfacial area with decreasing wetting phase saturation (curve b, Figure 5.1) [Cary, 1994; Silverstein and Fort, 1997; 2000; Or and Tuller, 1999; Tuller, *et al*., 1999]. As water saturation goes lower, the contribution of water films to interfacial area is more significant than that of pendular rings, and accordingly the maximum interfacial area is observed at the lowest water saturation reached by the system, where the surface of water films are believed to be at maximum.

5.1.2. *Experimental Measurements of Interfacial Area*

Laboratory-scale quantitative determination of fluid-fluid interfacial area has received increasing interest in recent years, since measurement techniques started to become available in 1990's [Karkare and Fort, 1996]. Based on the methods used to trace the generated interface, techniques reported in the literature can be basically divided into four groups: water-insoluble surfactant methods, aqueous surfactant methods, gaseous tracer methods, and microtomography methods. Each method will be briefly discussed below.

Water-insoluble surfactant methods, also called water mobilization or static methods by some researchers [Costanza and Brusseau, 2000] were first reported by Karkare and co-workers [Karkare *et al*., 1993; Karkare and Fort, 1993; 1994; 1996]. In this method, water-insoluble surfactant is added to one-half of a horizontal column packed to a desired water saturation, and water moves from the surfactant-containing side to the surfactant-free side, driven by the capillary pressure gradient between the two halves of the column. Air-water interfacial area is then calculated knowing the amount of surfactant needed to initiate water movement and the area occupied by each surfactant

molecule at interface. Since the saturation is achieved by pre-mixing water with porous material, the measured values do not necessarily correspond to a specific point on the P_c-S curve.

Using aqueous surfactant methods, air-water [Kim, *et al*., 1997; Saripalli, *et al*., 1997] and NAPL-water [Kim, *et al*., 1999a; Saripalli, *et al*., 1997; 1998; Jain, *et al*., 2003] interfacial areas have been measured through miscible displacement experiments. Breakthrough curves measured for both interfacial-active and -nonactive tracers passing through a partially saturated column are used to estimate the amount of aqueous surfactant retarded by the fluid-fluid interface. Three limitations associated with miscible displacement methods are: First, the interfacial area can be underestimated due to bypassing of small and/or isolated pores. Second, the method is not feasible at very low water saturations, because unsaturated conductivity decreases exponentially with decreased water content, and measurements at low water saturation require extremely low flow rates and impractically long running times. Third, the addition of surfactant during displacement may induce the change of pore water configuration and the mobilization of air-water interface, causing the measured interfacial area to differ from the area originally present in the system.

Aqueous surfactant has also been used with custom-constructed columns that can be disassembled to overcome, at least to some extent, the limitations listed above [Anwar, *et al*., 2000; Schaefer, *et al*., 2000]. The packed column is initially saturated with surfactant solution, and then allowed to drain by gravity. When equilibrium is reached, the column is disassembled and each section is analyzed for saturation and surfactant concentration in pore water, which are used to calculate interfacial area.

Using gaseous tracer methods, air-water interfacial area has been measured with miscible displacement techniques analogous to the method described above for aqueous surfactant, except that gas is the mobile phase carrying the interfacial tracer [Kim, *et al*., 1999b; Costanza-Robinson and Brusseau, 2002; Peng and Brusseau, 2005]. In contrast to aqueous surfactant methods, gaseous tracer methods are more suitable to measure interfacial area of porous media at low water saturation. At high saturations, gaseous tracers may not be able to access the air-filled pores disconnected from gas flow path, and more disconnected dry pores are expected with the increase of water saturation.

For all the interfacial tracer methods discussed above, a monotonic increase of interfacial area with the decrease of water saturation is observed (curve b, Figure 5.1), implying a significant contribution of water films covering grains. However, results from the different methods do not always agree with each other quantitatively. For example, the interfacial area obtained from gaseous tracer methods is much higher than those obtained from water-insoluble and aqueous surfactant methods. The air-water interfacial areas determined using a gaseous tracer by Kim, *et al*. [1999b] were 2 to 3 times higher than those measured using an aqueous surfactant [Kim, *et al*., 1997] for the same sand over the same water saturation range ($0.29 \leq S \leq 0.55$). As water saturation goes lower, a sharp increase of interfacial area is usually observed in gaseous tracer method results [Brusseau, *et al*., 1997; Costanza-Robinson and Brusseau, 2002; Peng and Brusseau, 2005], and the measured air-water interfacial area can be as much as 2-3 orders of magnitude higher than that obtained from aqueous tracer method [Anwar, *et al*., 2000; Schaefer, *et al*., 2000] for a similar system. Two reasons have been proposed for this discrepancy [Costanza and Brusseau, 2000]. First, the air-water interface is more

accessible for gaseous tracer than for aqueous tracer, especially at low water saturations as discussed earlier. Second, multilayer adsorption observed for organic vapors [Cutting and Jones, 1955; Jones and Ottewill, 1955] might have occurred to gaseous tracers, leading to an overestimation of interfacial area, especially when high tracer concentration is applied [*e.g.*, Brusseau, *et al*., 1997]. If this happens, the gaseous tracer method actually measures the total mass of organic vapor retained by interface, and not the real interfacial area.

Recently, microtomography methods have been reported, making use of three-dimensional X-ray imaging to determine air-water interfacial area [Culligan, *et al*., 2004; 2006]. The method allows the pore-scale observation of the distribution of phases, and of the formation and movement of air-water interfaces when saturation changes. Air-water interfacial area is estimated based on the observed specific surface areas of wetting phase, non-wetting phase, and solid phase. Because the method does not detect water films, the measured interfacial area is found to be an inverted parabolic function of water saturation (curve a, Figure 5.1). The maximum interfacial area obtained from this method is about one order of magnitude smaller than that obtained from aqueous tracer methods for a similar system, possibly due to the inability to measure the contribution of water films.

5.1.3. *General Limitations of Current Experimental Techniques*

While all previously-published techniques can provide an estimate of interfacial area as a function of saturation for a natural porous media, due to practical difficulties, none has been successfully applied to evaluate the influence of drying/wetting history. In the gaseous tracer and water–insoluble surfactant methods, the desired saturation was

achieved by pre-mixing a certain amount of water with porous media, bypassing the natural drying/wetting processes. In some reported interfacial area measurements with aqueous surfactant [Kim, *et al*., 1997; Saripalli, *et al*., 1997; Anwar, *et al*., 2000], drying/wetting history was not considered, although corresponding capillary pressure was able to be determined simultaneously with the measurement of interfacial area. In more recent studies using visualization [Culligan, *et al*., 2004] and aqueous tracer [Jain, *et al*., 2003] methods, the number of collected data points were very limited, although interfacial areas were measured to several drainage and imbibition cycles. To examine the hysteresis of interfacial area measured along different drying/wetting processes, however, intensive and detailed data are necessary to provide conclusive information.

In addition, most commonly used miscible displacement techniques with the application of interfacial tracers (aqueous or gaseous) often involve significant interfacial tension variations during area measurements. It has been found that interfacial tension gradients present in the porous media system induce transient flow from low interfacial tension regions to high interfacial tension regions [Henry and Smith, 2003]. As a consequent, significant variation in interfacial tension may result in the redistribution of pore water and the mobilization of interface, causing the interfacial area measured using displacement techniques to differ from the area originally present in the system. As such, experiments with relatively constant interfacial tension are needed to evaluate the influence of interfacial tension variations on the magnitude of interfacial area, providing the useful information for the design of surfactant-based environmental remediation applications.

5.1.4. *Objectives*

There are two objectives in this chapter. The first is to experimentally investigate the possible hysteresis in three dimensional P_c-S-A relationships of natural porous media. The second is to experimentally evaluate the influence of surfactant-induced interfacial tension variations on fluid-fluid interfacial areas. For these two objectives, a new and rapid experimental method was developed to measure interfacial areas simultaneously with the measurement of the corresponding hysteretic P_c-S relationships. The method makes use of the automated P_c-S device described in Chapter 2, in combination with real-time detection of an aqueous surfactant interfacial tracer. Air-water interfacial areas were measured under different conditions to explore influences of drying/wetting history, surfactant concentration, surfactant-induced variation in interfacial tension, and porous media properties. Implications of results for environmental systems are discussed.

5.2. MATERIALS AND EXPERIMENTAL METHODS

5.2.1. *Materials*

In this chapter, four different porous media received from U. S. Silica (Berkeley Springs, WV) were used for air-water interfacial area measurements: medium sand F-45, fine sand F-95, ultra-fine sand F-110, and silt SIL-CO-SIL 250 (SCS-250). Prior to use, the media were rinsed with Nanopure water (Nanopure Infinity, Barnstead International, Dubuque, Iowa) to remove impurities and some ultra fines. Mean grain sizes, porosities, gravities, and specific geometric surface areas of different media are listed in Table 5.1.

The specific geometric surface area was estimated from a log-normal fit to particle size distributions by assuming each grain to be spherical.

Table 5.1. Properties of Porous Media Used in Air-Water Interfacial Area Measurements.

Porous medium	F-45	F-95	F-110	SCS-250
Type [a]	Medium sand	Fine sand	Ultra fine sand	Silt
Mean grain size, d_{50} (μm) [b]	323	140	120	45
Packed porosity [c]	0.349 ± 0.026	0.349 ± 0.007	0.362 ± 0.006	0.413 ± 0.019
Specific geometric surface area (cm^2/g) [d]	76	172	200	793
Gravity (g/cm^3) [e]	2.65			

a: Based on the classification frequently used by sedimentologists. Source: Friedman and Sanders [1978].
b: Obtained from log-normal fit to the grain size distribution provided by the manufacturer.
c: Standard error is calculated from duplicate measurements.
d: Estimated from log-normal fit to the grain size distribution by assuming each grain to be spherical.
e: Data provided by the manufacturer.

An anionic surfactant, sodium octylbenzene sulfonate (SOBS, MW = 292.4, 97% purity, Sigma-Aldrich Corp., St. Louis, MO) was selected as interfacial tracer. Advantages of using an anionic surfactant, such as negligible volatility and negligible adsorption to quartz sand surfaces, were described by Saripalli, *et al*. [1997]. SOBS was selected in part because it is one of the few commercially-available isomerically-pure alkyl-benzene sulfonate surfactants, which can avoid complications in area measurements caused by complex mixed adsorption behavior [Kibbey and Hayes, 1997]. For all SOBS

solutions used, sodium chloride (NaCl) was maintained at 0.1 M to ensure a constant and excess counter ion (Na^+), simplifying application of the Gibbs adsorption equation [Adamson, 1997] and reducing required surfactant concentration. SOBS concentrations of 50, 100, 200, 400, and 500 mg/L were used in air-water interfacial area measurements to study effects of concentration. A 500 mg/L SOBS solution was chosen to study the influences of drying/wetting history and surfactant-induced interfacial tension variations.

5.2.2. Experimental Measurement of Interfacial Area

In this chapter, a new method was developed for the simultaneous measurement of fluid-fluid interfacial area and hysteretic P_c-S relationships, making use of the custom-designed, automated P_c-S device described in Chapter 2, with two major modifications involved for area measurements. The first modification is the placement underneath the pressure cell of an additional flow-through fiber optic ultra-violet (UV) spectrometer (Model: SD2000, Ocean Optics, Inc., Dunedin, FL) equipped with a custom 4 mm-path length flow-through optical cell to detect the concentration of SOBS solution (wetting fluid) draining out of or imbibing into the porous medium. The second modified part is the pressure cell holding the testing porous medium. While the dimension and structure of the pressure cell used here are almost the same as previously described in Chapter 2, the bottom cap was modified for ultra-low dead volume. A # 80 mesh stainless steel screen (Small Parts Inc., Miami Lakes, FL) is used at the bottom cap instead of a porous plate to support the capillary barrier and further reduce dead volume. The total dead volume of the system below the soil chamber is approximately 75 μL, which is equivalent to approximately 3% of the pore volume of the packed porous medium. For clarity, the entire device setup for area measurements is shown in Figure 5.2. The method

for fully-saturated packing, the procedure for operating the system, and the method for control and calculation of capillary pressure and saturation values are described briefly below. More detailed information was described in Chapter 2.

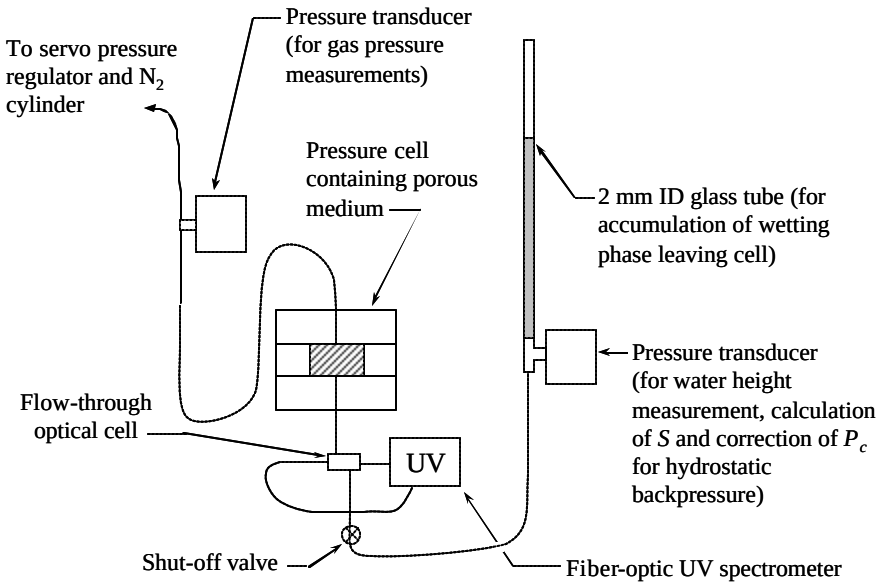


Figure 5.2. Schematic diagram of the experimental apparatus used for the simultaneous measurement of capillary pressure (P_c), saturation (S), and air-water interfacial area (A). For organic liquid-water interfacial area measurements, an organic liquid reservoir is placed in line before the pressure cell.

Briefly, for the area measurement performed in this research, the porous medium soaked in 0.1 M NaCl solution is packed tightly in the pressure cell with hydrophilic nylon membranes of 20 μm pore size (Osmonics Inc., Minnetonka, MN) sealed at both the bottom and top caps. The bottom of the pressure cell is connected to the flow-through optical cell of UV spectrometer, and 0.1 M NaCl solution is flushed from the top. When the UV spectrum of the effluent has stabilized (due to dispersal of fines and dissolved

silica), the flushing liquid is changed to SOBS solution and flushing is continued for at least 30 additional pore volumes. Before flushing is stopped, the UV spectrum of SOBS effluent is recorded. The difference between spectra of SOBS standard solution and SOBS effluent provides the spectrum of suspended fines needed in area calculation (as described later in the **Section 5.3.3. UV Spectrum Fitting**). Finally, the glass capillary tube is connected, a hydrophobic Teflon membrane (wetting phase capillary barrier, Osmonics Inc., Minnetonka, MN) is applied at the top of the SOBS-saturated medium to replace the hydrophilic nylon membrane, and the non-wetting phase tubing is connected to the top of the cell.

Non-wetting phase pressure is computer-controlled to automatically increase or decrease step by step at a pre-determined rate to produce drainage and imbibition respectively. When non-wetting phase pressure is increased high enough to initiate primary drainage, the non-wetting phase penetrates into the previously fully-saturated medium, SOBS solution drains out (and is collected in the glass tube), and fluid-fluid interface is generated. SOBS molecules adsorb to the newly-created fluid-fluid interface, resulting in a decreased bulk concentration in the pore solution. The decreased concentration is detected by the UV spectrometer when SOBS solution flows out of the medium. When the medium stops draining with the further increase of the non-wetting phase pressure, the residual wetting phase saturation is reached. The main imbibition is then initiated by decreasing non-wetting phase pressure step by step. SOBS solution collected in the glass capillary tube flows back into pressure cell, with concentration being detected by UV spectrometer, and integrated to determine the moles of SOBS returning to the cell prior to the next drainage. As such, hysteretic P_c-S relationships

containing multiple drainage/imbibition cycles are obtained by controlling the non-wetting phase pressure, and corresponding interfacial areas can be measured simultaneously. Capillary pressure and saturation are calculated as described in Chapter 2, and the fluid-fluid interfacial area corresponding to each specific point along each drainage curve is determined as described later in the **Area Calculation** section (**Section 5.3**).

In this chapter, air-water interfacial areas were measured using high purity nitrogen gas as non-wetting phase. In all experiments discussed here except those specifically designed to examine rate effects (e.g. Figure 5.4), interfacial area and hysteretic P_c-S relationships were measured under slow-dynamic (pseudo-static) conditions, where the rate of gas phase pressure change (dP_n/dt) was carefully selected to eliminate dynamic effects on P_c-S relationships and to ensure equilibrated interfacial adsorption. The decision to use a slow-dynamic approach was based in part on an observation that the big pressure jumps between steps and the long equilibration time at each step in static methods often caused bubbles to come out of solution and become trapped in the optical cell or tubing, especially over the course of multiple drainage/imbibition cycles where flow direction changes, interfering with both the measurement of P_c-S relationships and the detection of SOBS concentration. The more gradual pressure and flow changes of the dynamic approach are much less likely to cause this problem. In addition, the slow-dynamic approach can provide much more detailed information than static methods. Note that using the described device, interfacial area can be measured in either static or dynamic mode.

5.3. AREA CALCULATION

5.3.1. *Surface Excess at the Fluid-Fluid Interface*

To calculate fluid-fluid interfacial area, the area occupied by each SOBS molecule at the interface has to be known. At a given temperature, the amount of surfactant adsorbed to interface is related to interfacial tension and bulk activity as expressed by the Gibbs adsorption equation [Adamson, 1997]. For example, the adsorption of ionic surfactant at an interface in the presence of swamping counter ion (as applied in this research) can be described by:

$$\Gamma = -\frac{a}{RT}\left(\frac{dg}{da}\right) \tag{5.1}$$

where Γ is the surface excess (mol/m^2), R is the ideal gas constant (8.314 J/mol K), T is the temperature (298 K), g is the interfacial tension (N/m), and a ($a=C\times f$) is the SOBS bulk activity (M), where C and f are the concentration and activity coefficient of SOBS, respectively. The activity coefficient, f, is estimated using Davies equation (Equation 5.2), which is valid for total ion strength (I) smaller than 0.5 M [Stumm and Morgan, 1988].

$$\log f_i = -0.5\, Z_i^2 \left(\frac{\sqrt{I}}{1+\sqrt{I}} - 0.2\, I\right) \tag{5.2}$$

$$I = \frac{1}{2}\sum_i C_i Z_i^2 \tag{5.2a}$$

where C_i and Z_i are the concentration and charge of ion species i, respectively.

In addition, surfactant adsorption at fluid-fluid interfaces is often described by the Langmuir equation at concentrations below the critical micelle concentration (CMC) [Rosen, 1988]:

$$\Gamma = \Gamma_{max} \frac{K \times a}{1 + K \times a} \qquad (5.3)$$

where Γ_{max} is the surface excess at interface saturation (the maximum surface excess, mol/m^2) and K is a constant (L/mol). Combining Equations (5.1) and (5.3) gives the Szyszkowski equation [Clint, 1975; Rosen, 1988], which describes interfacial tension as a function of activity:

$$g_0 - g = RT\ \Gamma_{max} \ln(1 + K \times a) \qquad (5.4)$$

where g_0 is the interfacial tension of the solution without surfactant. The constants Γ_{max} and K are determined by fitting Equation (5.4) to the $g \sim a$ plot obtained from interfacial tension measurements. With this information, the surface excess, Γ, at any given solution activity can be determined from the Langmuir equation (Equation 5.3). The reciprocal of Γ gives the fluid-fluid interfacial area occupied by each mole of surfactant.

5.3.2. *Air-Water Interfacial Tension Measurement*

Air-water interfacial tensions (γ) of SOBS solutions, with concentrations ranging from 3.5 mg/L (0.012 mM) to 1960 mg/L (6.70 mM), were measured using the pendant drop method [Del Rio and Neumann, 1997]. The measuring system and operation were described in detail by Mohammad and Kibbey [2005].

The measured SOBS air-water interfacial tension in 0.1M NaCl solution, as well as the fit from the Szyszkowski equation (Equation 5.4) and the resulting Langmuir isotherm is shown in Figure 5.3 as a function of SOBS activity. The measured CMC of SOBS in 0.1 M NaCl solution is 700 mg/L (2.39 mM, corresponding to an activity of 1.85 mM). The saturation surface excess Γ_{max} and constant K in Langmuir equation determined from the fit are 4.260×10^{-6} mol/m^2 and 9637.3 L/mol respectively.

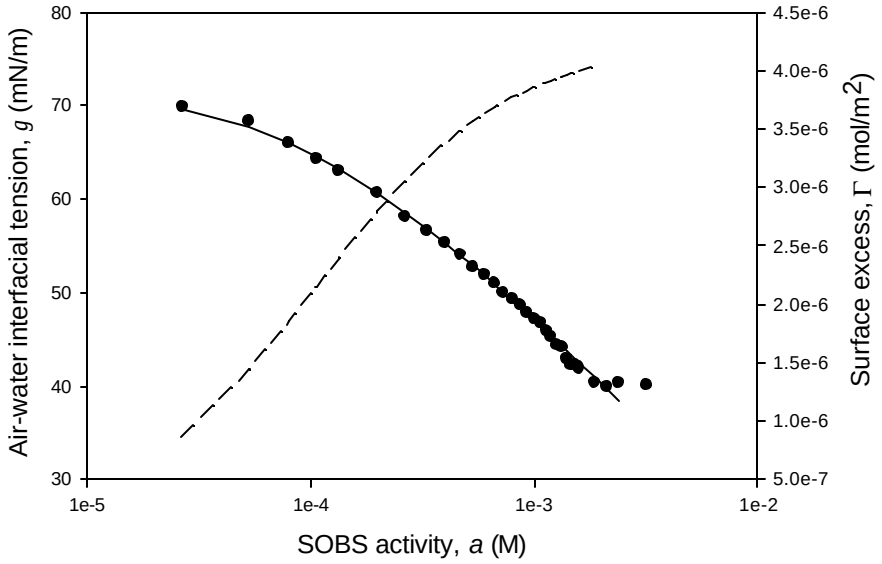


Figure 5.3. Air-water interfacial tension (solid circle: experimental data; solid line: fit from the Szyszkowski equation) and surface excess (dashed line) of SOBS in 0.1 M NaCl solution as a function of SOBS activity.

5.3.3. *UV Spectrum Fitting*

Concentrations of SOBS are measured using a fit to the full absorbance spectrum of the surfactant leaving or entering the cell. This approach is necessary because of the high sensitivity of measurements to small changes in dispersed fines which occur when flow rates change and flow is reversed, particularly when surfactant solutions are used. Early tests using a single variable wavelength UV detector were not successful, due to changing absorbance from background fines. The entire spectrum was fit based on the spectra of SOBS standard and of suspended fines (determined as a difference spectrum between the SOBS standard and the SOBS saturation effluent of the cell), by adjusting the concentration of the unknowns (in this case, SOBS and fines) to minimize the error between a predicted spectrum and the experimentally measured spectrum. The method is highly insensitive to the presence of fines, and is actually capable of simultaneous detection of multiple compounds with different absorbance spectra [Hari, *et al*., 2005].

For this work, a wavelength range of 219-300 nm (475 wavelengths, at approximately 0.17 nm wavelength increments) was used for 50 and 100 mg/L SOBS solutions, while a range of 240-300 nm (356 wavelengths, at approximately 0.17 nm wavelength increments) was used for higher concentration solutions. The larger range improved detection for the low concentration solutions, due to the large SOBS absorbance peak near 232 nm, but could not be used for the high concentration solutions because of detector saturation.

5.3.4. *Calculation of Interfacial Area*

The amount of SOBS adsorbed at the fluid-fluid interface is determined from a continuous mole balance (Equations 5.5 to 5.7), updated at each drainage or imbibition step throughout the experiment (typically 30 second intervals or less):

$$M_{IF}^{i} = M_{T}^{i} - C^{i} \times V_{P}^{i} \tag{5.5}$$

$$M_{T}^{i} = M_{T}^{i-1} - C^{i} \times \Delta V_{D}^{i} \tag{5.6}$$

$$V_{P}^{i} = V_{P}^{i-1} - \Delta V_{D}^{i} \tag{5.7}$$

The superscript i is the step number, M_{IF} is the moles of SOBS adsorbed at the interface (mol), M_T is the total moles of SOBS present in the pressure cell (mol), C is the concentration of SOBS solution draining out or imbibing into the porous material (M), V_P is the remaining volume of the pore solution in the pressure cell (L), and DV_D is the volume of SOBS solution draining out (positive) or imbibing into (negative) the pressure cell at the step (L), determined from changes in the hydrostatic pressure of wetting fluid collected in the glass capillary tube.

Prior to primary drainage (step 0), the porous medium is fully saturated with SOBS solution with known concentration (C^0), so the volume of pore solution (V_P^0) and the total moles of SOBS initially present in the pressure cell (M_T^0) are known ($M_T^0 = C^0 \times V_p^0$). The moles of adsorbed SOBS (M_{IF}^i) can be calculated stepwise during drainage. Although Equation (5.5) cannot be applied to imbibition because the concentration in the pore solution is not the same as that of the imbibing solution,

Equations (5.6) and (5.7) are still valid to track the moles of SOBS and the volume of the pore solution present in the pressure cell at each step during imbibition, providing the boundary information (M_T and V_P) needed to calculate M_{IF} for secondary and scanning drainages.

Knowing SOBS activity in the pore solution at step *i* during drainage, surface excess at the same step, Γ^i, can be calculated using Equation (5.3). The corresponding fluid-fluid interfacial area, A^i (m^2), is then calculated as:

$$A^i = \frac{M_{IF}^i}{\Gamma^i} \tag{5.8}$$

An inherent assumption of the method is that the SOBS concentration leaving the cell during drainage is equal to the concentration throughout the cell (*i.e.*, concentration gradients within the cell and tubing are minimal). This assumption is likely to be most valid at lower saturations, where draining water comes from throughout the porous medium, and the saturated volume separating the newly-formed interface from the UV detector is minimal. Implications of this assumption are discussed in the **Results and Discussion** section.

5.4. RESULTS AND DISCUSSION

5.4.1. *Influence of the Rate of Pressure Change on the Measured Air-Water Interfacial Area*

In this study, air-water interfacial area was measured under slow-dynamic (pseudo-static) conditions. The conditions used have been demonstrated previously to produce P_c-S curves that duplicate static measurements (Chapter 2). However, for this work, it is also necessary to determine if rates are sufficiently slow to allow equilibrium surfactant adsorption and interface formation. Figure 5.4 shows air-water interfacial area (reported as cm^2 per gram dry medium) as a function of water saturation for the sand F-110, measured during primary drainage at gas phase pressure rates (dP_n/dt) ranging from 0.052 to 0.010 cm water per second. From the figure, it is apparent that the concentrated SOBS solution (500 mg/L) equilibrates much faster than the dilute SOBS solution (50 mg/L). As such, the rate of 0.020 cm water per second was used for the measurements with 500 mg/L SOBS, while the rate of 0.010 cm water per second was used for the experiments using solutions with lower SOBS concentrations.

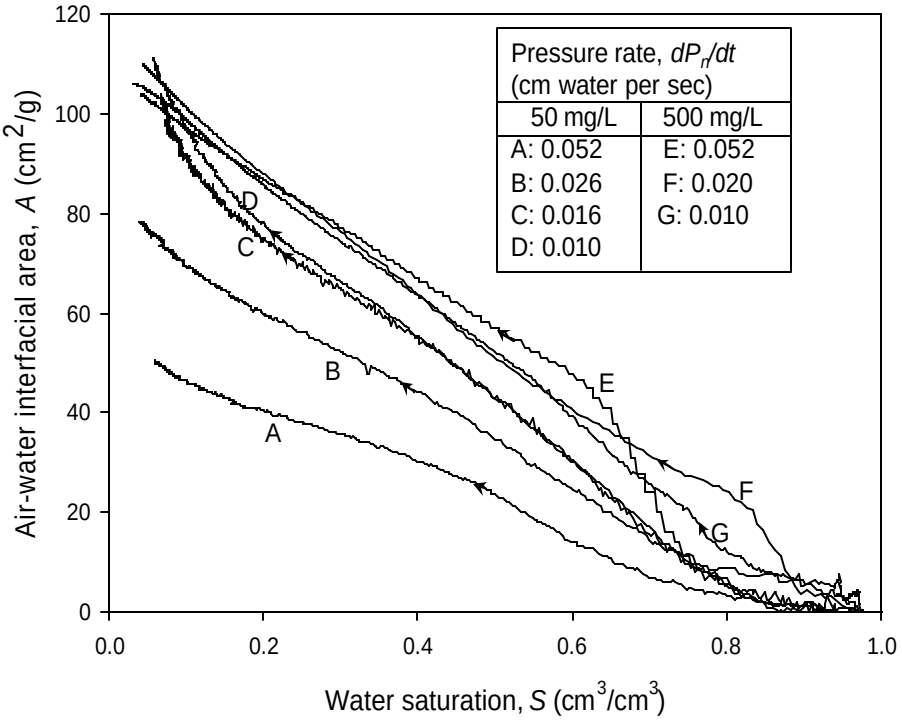


Figure 5.4. Influence of the rate of pressure change on the interfacial area measured for F-110 sand during primary drainage at two different SOBS concentrations (50 and 500 mg/L).

5.4.2. *Capillary Pressure, Saturation and Air-Water Interfacial Area Relationships Measured During Primary Drainage: Influence of SOBS Concentration*

SOBS solutions with concentrations of 50, 100, 200, 400 and 500 mg/L were used to study the influence of surfactant concentration on the measured capillary pressure, saturation, and interfacial area relationships. Initial interfacial tensions of the solutions used range from 63 to 44 mN/m. Concentrations below the CMC (700 mg/L) were chosen to avoid SOBS precipitation. Ultra-fine sand F-110 was used as a representative porous medium in this study. The capillary pressure-saturation (P_c-S), interfacial area-saturation (A-S), and interfacial area-capillary pressure (A-P_c) relationships measured for F-110 sand during primary drainage with different SOBS concentration are shown in Figure 5.5.

P_c-S curves shown in Figure 5.5a illustrate that, as would be expected from Leverett scaling [Leverett, 1941], capillary pressure decreases with increasing SOBS concentration at a given saturation. Figure 5.5a also shows the decreased wetting phase residual saturation with increasing SOBS concentration, indicating that the low interfacial tension facilitates the drainage process.

Figure 5.5b plots the measured A-S relationships of F-110 sand corresponding to P_c-S curves shown in Figure 5.5a. In general, slightly higher interfacial areas are observed in experiments with higher concentrations, with the difference ranging from 8 cm^2/g at low saturations to approximately 20 cm^2/g at high saturations. The differences likely result from the fact that as in systems where less adsorption occurs (as in the case of low concentration SOBS), calculation of interfacial area is more sensitive to small

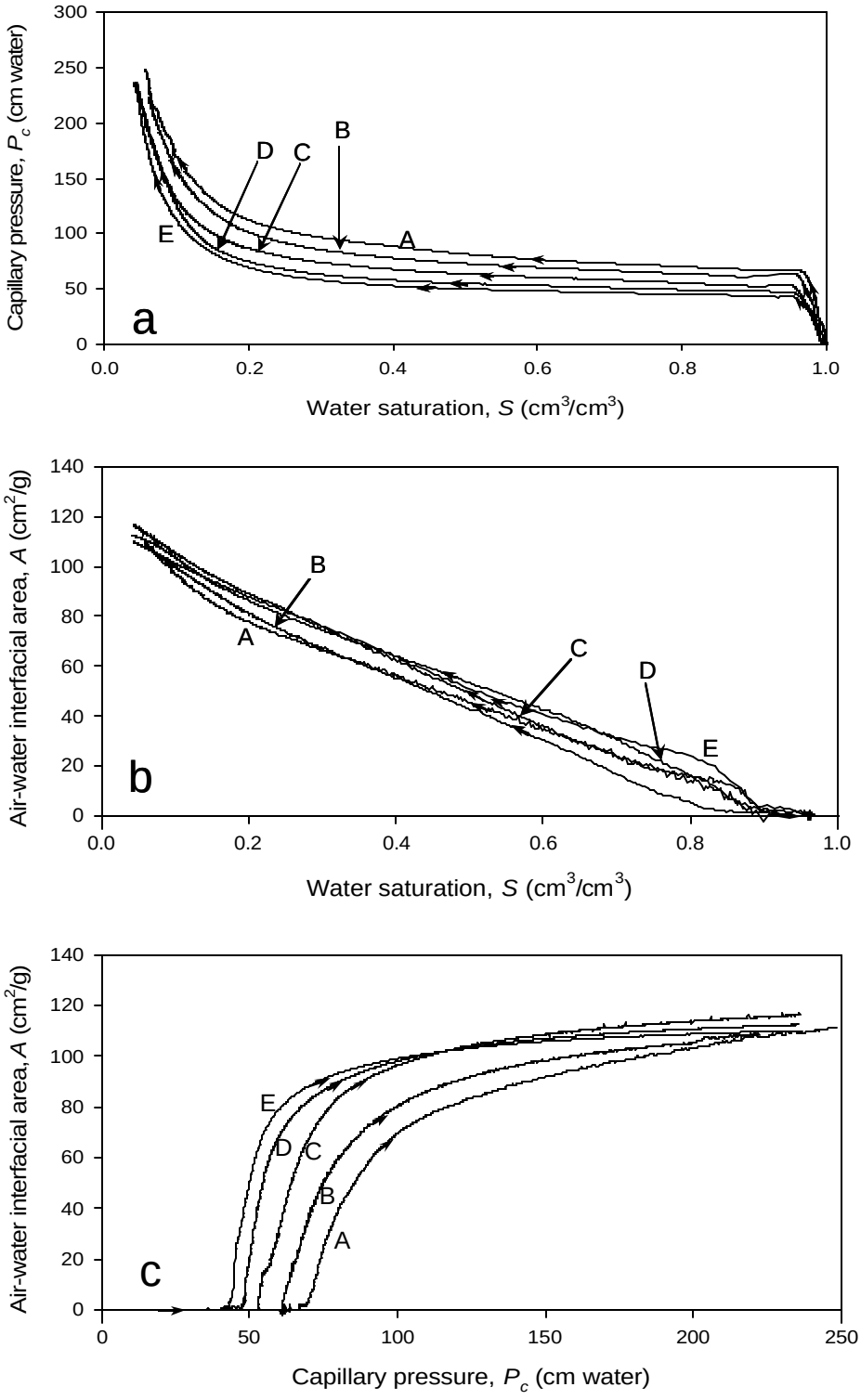


Figure 5.5. Influence of SOBS concentration (A: 50; B: 100; C: 200; D: 400; and E: 500 mg/L) on P_c-S (a), A-S (b), and A-P_c (c) relationships of F-110 sand measured during primary drainage.

errors in concentration measurement and the surface tension vs. concentration curve. That is, a certain amount of adsorption is necessary for accurate measurement of interfacial area, and the less adsorption that takes place, the more difficult accurate measurement becomes. Nevertheless, the similarity of the low and high concentration curves in Figure 5.5b indicates that the surfactant concentrations used do not cause appreciably different interfacial areas to be generated. This result further suggests that the interfacial area measured by the described method is likely a reasonably good indication of interfacial area in the absence of surfactant.

It should be noted that the greater interfacial area variation observed at high saturations regardless of concentration (see also curves E to G in Figure 5.4) may result from subtle differences in packing, since interface formation during initial drainage is likely to be most sensitive to differences in flow paths. At lower saturations (below $S \approx 0.6$), experiment-to-experiment variability in interfacial area measured using a particular concentration of SOBS tends to be quite small, typically within a few cm^2/g over the range of saturations.

In general, for all of the applied SOBS concentrations, *A*-*S* relationships of F-110 sand reveal a monotonic increase of area with the decrease of water saturation. The largest experimentally measured interfacial area varies from 109 to 116 cm^2/g dry sand corresponding to the residual water saturation, which varies between 0.04 and 0.06 depending on SOBS concentrations (Figure 5.5a). The surface area of F-110 sand estimated by extrapolating *A*-*S* curves to zero saturation (e.g. infinitely thin water films covering the grains) is between 120 to 140 cm^2/g, which is approximately 60-70% of the specific surface area estimated geometrically for the material (200 cm^2/g, Table 5.1) and

approximately 10% of the surface area obtained from BET-N_2 adsorption to the dry sand (1336 cm^2/g). The magnitude of measured interfacial areas is consistent with published studies using aqueous interfacial tracers [Kim, *et al.*, 1997; Saripalli, *et al*., 1997; Anwar, *et al*., 2000; Schaefer, *et al*., 2000].

It should be noted that the measured interfacial area remains quite low down to saturations of approximately 0.9 for all curves shown in Fig. 5.5b. This is likely due to the concentration gradients in both the porous medium and the tubing. As mentioned in the **Experimental Measurement of Interfacial Area** section (**section 5.2.2**), dead volume in the tubing is responsible for a shift in saturation of approximately 0.03, an error which should be constant throughout the saturation range. The continued low interfacial area down to $S \approx 0.9$ (an additional 0.07 from what would be expected from tubing dead volume alone) is likely due to concentration gradients in the porous medium, which in particular are expected to be most pronounced during the initial portion of the primary drainage curve, where drainage occurs from the top of the cell rather than uniformly throughout the cell. The effect of concentration gradients would be expected to decrease to zero with decreasing saturation.

Interfacial area as a function of capillary pressure is shown in Figure 5.5c. It is clear that capillary pressure influences interfacial area by influencing water saturation. Interfacial areas increase with the increase of capillary pressure and tend to level off at high capillary pressures where residual water saturation is approached.

5.4.3. *Air-Water Interfacial Areas Measured for Different Porous Media during Primary Drainage*

Air-water interfacial areas of different porous media were measured as a function of saturation during primary drainage, using 500 mg/L SOBS solution and 0.020 cm water per second gas pressure rate (Figure 5.6). For all the porous media, interfacial areas monotonically increase with decreasing saturation. In general, the magnitudes of the interfacial areas measured for different porous media at a given saturation strongly depend on the grain sizes, with higher interfacial areas observed for finer porous media. This observation is consistent with the knowledge that the finer the porous medium, the higher the specific surface area, demonstrating the stability and reliability of the developed method.

The specific surface areas of porous media estimated by extrapolating the *A-S* curves to zero saturation are listed in Table 5.2, in comparison with the values obtained from log-normal fit to grain size distributions by assuming each grain is spherical. Results show that the areas estimated from extrapolation are about 50 to 80% of the corresponding areas estimated mathematically, which indicates that the interfacial areas measured for different porous media at low saturations are approaching the surface areas of the media themselves.

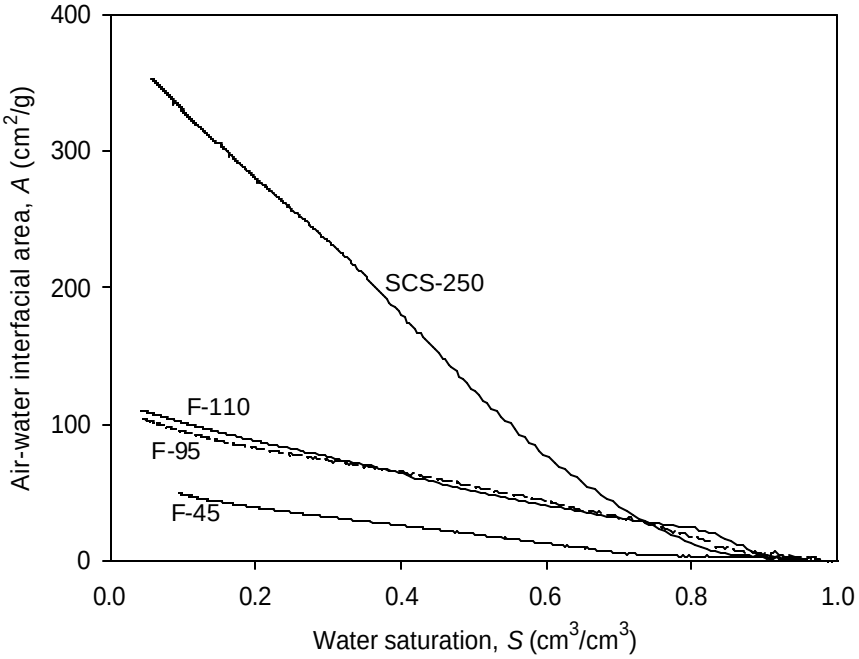


Figure 5.6. Air-water interfacial areas measured for different porous media during primary drainage.

Table 5.2. Comparison of Specific Surface Areas (cm^2/g) of Different Porous Media between the Values Estimated from Extrapolating *A*-*S* Curves and the Values Estimated from Log-Norman Fit to Grain Size Distributions.

Medium	Estimated from extrapolation (cm^2/g)	Estimated from Log-Normal fit (cm^2/g)
F-45	60	76
F-95	112	172
F-110	120	200
SCS-250	400	793

5.4.4. *Capillary Pressure, Saturation and Air-Water Interfacial Area Relationships: Influence of Drying/Wetting History*

To study the influence of drying/wetting history on air-water interfacial area, interfacial area measurements were conducted for primary, secondary and one scanning drainages of F-110 sand initially saturated with 500 mg/L SOBS solution. The minimum SOBS concentration of pore water was observed as 313 mg/L at the end of primary drainage. As a result, the interfacial tension over the entire experiment remained relatively constant, varying between 44 and 49 mN/m. Experimental results are shown in Figure 5.7, showing 3D P_c-S-A curves and also P_c-S, A-P_c and A-S curves in corresponding 2D projection planes. (Because the method does not measure interfacial area during imbibition, curves corresponding to imbibition are only shown in the P_c-S plane.)

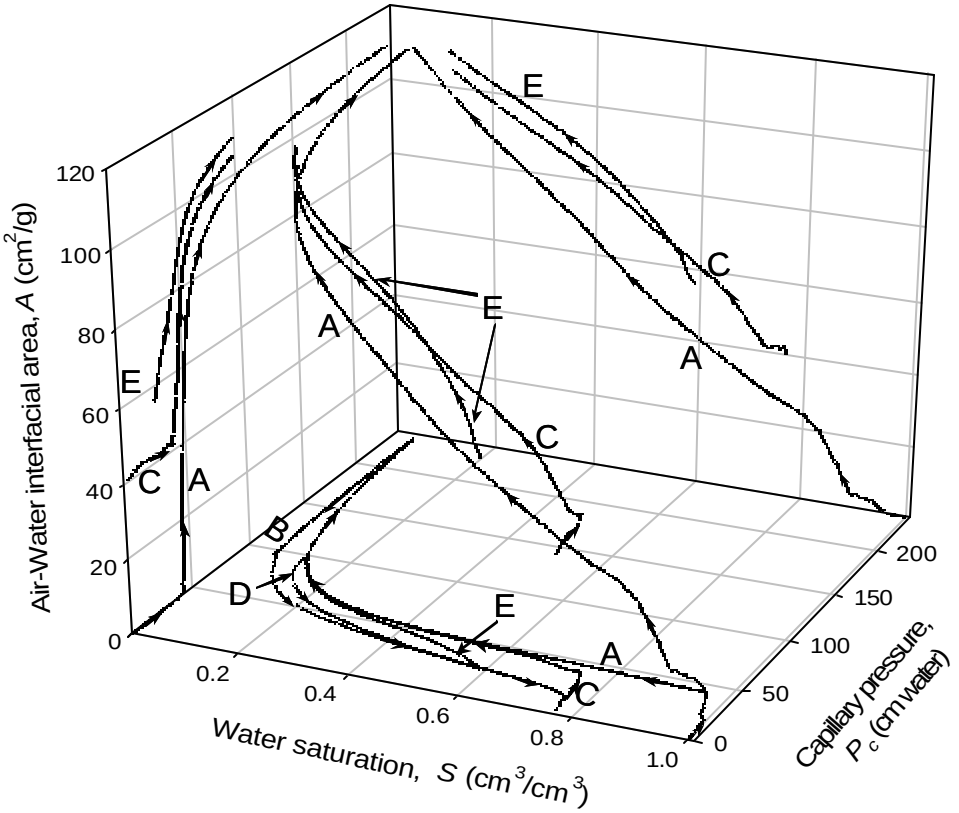


Figure 5.7. P_c-*S*-*A* relationships of F-110 sand showing the influence of drying/wetting history under conditions of minimal interfacial tension variation (5 mN/m over the course of the experiment). A: primary drainage; B: main imbibition; C: secondary drainage; D: scanning imbibition; E: scanning drainage. Note that interfacial areas are only measured during drainage.

During primary drainage, the largest experimentally-measured interfacial area is 115 cm^2/g dry sand, corresponding to a residual water saturation of 0.04. Within the saturation range studied, the measured interfacial areas for secondary and scanning drainages are 8 to 20 and 12 to 22 cm^2/g higher, respectively, than those for primary drainage, with the magnitude of the difference depending on saturation. In general, the *A*-*S* curves for the secondary and scanning drainages are quite similar to one another.

Although the scanning *A-S* curve may be slightly higher than the secondary drainage *A-S* curve over much of the saturation range, and this difference is reproducible, the differences between the secondary and scanning *A-S* curves are within the typical experiment-to-experiment variability of the method, so that it would be difficult to conclusively say that they are different. However, both curves exhibit higher interfacial areas than the primary drainage *A-S* curve, indicating that more interfaces may be created during secondary and subsequent drainages than during primary drainage at a particular saturation. There are two possible reasons for this result. First, the imbibition process re-arranges the pore water geometry and water distribution, which may cause higher interfacial areas for secondary and later drainages. Second, the existence of the air phase entrapped after imbibition causes more pendular rings in the system at a particular saturation (compared with primary drainage), and pendular rings are thought to be a significant contribution to the interface caused by capillarity [Gvirtzman and Roberts, 1991]. The influence of imbibition-induced re-arrangement and re-distribution on interfacial area is minimized between secondary and subsequent drainages since air phase is originally present prior to the start of these drainages.

The influence of drying/wetting history on interfacial area values observed in this research is consistent with previously published network model simulations [Reeves and Celia, 1996; Held and Celia, 2001], which found higher interfacial area for secondary and scanning drainages in comparison with primary drainage, as well as the crossing between secondary and scanning drainages. (It should be noted that because the models ignored water films, the shapes of predicted curves differed from those measured here in that the model-predicted interfacial area decreases to zero as zero saturation is approached.)

Recently published experimental studies using aqueous tracer displacement [Jain, *et al*., 2003] and X-ray imaging [Culligan, *et al*., 2004; 2006] methods found subtly higher interfacial area for secondary and subsequent drainages than for primary drainage, although the magnitude of the effect was smaller than was observed in this work.

An interesting observation can be made from the results in Figure 5.7 regarding interfacial area hysteresis. Theories of multi-phase flow developed by Hassanizadeh and Gray [1993] suggest that the hysteretic P_c-S relationship may be a projection of a non-hysteretic three-dimensional P_c-S-A relationship. The results in Figure 5.7 do not support this. To begin with, the primary and secondary drainage P_c-S curves are nearly identical below a saturation of 0.6, and also overlap the scanning drainage curve below a saturation of 0.35, yet interfacial area is considerably different between primary and subsequent drainages over those saturation ranges. This result is consistent with the network model results reported by Held and Celia [2001], who found considerably different interfacial areas for overlapping regions of the P_c-S relationship between primary and subsequent drainages. Further, the secondary and scanning drainage A-S curves in Figure 5.7 are quite similar over their entire range (and appear to cross at a saturation just below 0.6), and yet they exhibit capillary pressures that differ by nearly a factor of two at high saturation. This result is also consistent with the network model results of Held and Celia [2001], who found that P_c was likely not a single-valued function of S and A for secondary and subsequent drainages.

Taken together, these results indicate that it is unlikely a unique non-hysteretic P_c-S-A relationship exists for the system studied, particularly when primary drainage is included. Note that the result of this work differ from the results reported by Cheng, *et*

al. [2004], who found a P_c-*S*-*A* relationship that was non-hysteretic to within 5 % in a 2D micro-model using decane and nitrogen as the wetting and nonwetting phases, respectively. The difference between their results and this work may stem from the much stronger wettability in the system studied here, the fact that the method used here accounts for interfacial areas of wetting films, which are difficult to track in micro-model methods, or simply differences between the drainage behavior of 2D and 3D porous media.

5.4.5. *Capillary Pressure, Saturation and Air-Water Interfacial Area Relationships: Influence of Surfactant-Induced Interfacial Tension Variations*

The application of *any* interfacial tracer in the measurement of interfacial area modifies the interface due to adsorption and corresponding change in interfacial tension. In our method, interfacial tension remains relatively constant over the entire experiment, typically varying by 5 mN/m or less. This means that creation and measurement of interfacial area take place under similar conditions. In contrast, published measurements using miscible displacement techniques have typically relied on interfacial tension variations of 15 to 40 mN/m [Kim, *et al*., 1997; 1999; Saripalli, *et al*., 1997; 1998; Jain, *et al*., 2003;]. Significant variation in interfacial tension may result in the redistribution of pore water and the mobilization of interface, causing the measured interfacial area to differ from the area originally present in the system. It has been shown that capillary pressure gradients caused by interfacial tension gradients induce transient flow from low interfacial tension (high pressure) regions to high interfacial tension (low pressure) regions [Karkare and Fort, 1996; Henry *et al*., 1999; Henry and Smith, 2003].

In this research, a specific experimental procedure was designed to study the influence of surfactant-induced interfacial tension variations on the magnitude of interfacial area. The procedure involves performing primary drainage in the absence of surfactant and then introducing surfactant during main imbibition for area measurement for subsequent drainages, producing a substantial interfacial tension reduction during the entire experiment. To produce this effect, the pressure cell packed with F-110 sand is flushed only with 0.1 M NaCl prior to the start of the experiment. When primary drainage is finished, the program is paused briefly, and the tubing is disconnected from the bottom of both the pressure cell and glass capillary tube, flushed and filled with 500 mg/L SOBS solution, and re-connected to the pressure cell and another capillary glass tube filled with SOBS solution to the height that the NaCl solution has reached in the original glass tube after primary drainage. As SOBS solution imbibes into the sand, the interfacial tension variation occurs in the pore solution, and the surfactant needed in measuring the air-water interfacial area during secondary and scanning drainages is introduced to the cell. Air-water interfacial areas for secondary and scanning drainages measured in this way (Figure 5.8) are compared to those measured when interfacial tension is relatively constant during the entire experiment (Figure 5.7) to evaluate the influence of surfactant-induced interfacial tension variations. For the experiment shown in Figure 5.8, at the end of main imbibition, SOBS concentration in pore solution was approximately 400 mg/L, corresponding to a decrease of interfacial tension from 72 mN/m to 47 mN/m (a 25 mN/m change) over the entire main imbibition process.

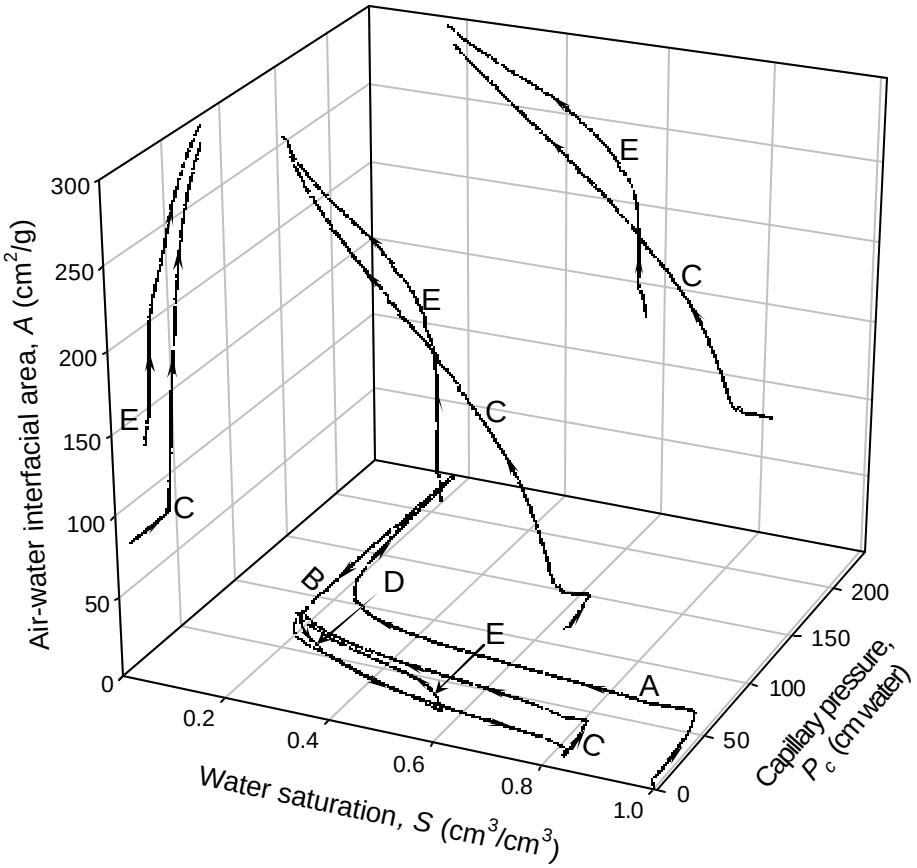


Figure 5.8. P_c-*S*-*A* relationships of F-110 sand corresponding to a 25 mN/m variation in interfacial tension during main imbibition. 0.1 M NaCl was used for primary drainage and 500 mg/L SOBS for main imbibition. A: primary drainage; B: main imbibition; C: secondary drainage; D: scanning imbibition; E: scanning drainage. Note that interfacial areas are only measured during secondary and scanning drainages.

To better illustrate the influence of interfacial tension variations on the measured interfacial area, Figure 5.9 re-plots 2D *A*-*S* relationships for secondary and scanning drainages measured under the conditions with and without significant interfacial tension variations. For a particular drainage, although the trends in *A*-*S* curves are similar under both conditions, much higher interfacial area is observed at a given saturation in the experiment where interfacial tension varies significantly (25 mN/m). For example, the

largest interfacial areas for secondary and scanning drainages measured in the experiment with significant interfacial tension variations are 283 cm^2/g (S = 0.17) and 295 cm^2/g (S = 0.16) respectively, which are approximately 2.8 times of those obtained from the experiment with relatively constant interfacial tension (100 cm^2/g for secondary drainage and 106 cm^2/g for the scanning drainage) at the same water saturations. The result suggests that the surfactant-induced flow caused by interfacial tension variations during main imbibition has the tendency to create new air-water interfaces. As such, methods that rely on substantial changes in interfacial tension may actually overestimate interfacial area under some conditions. Furthermore, the results of this work suggest that any practical application that substantially changes the interfacial tension of an interface (e.g., surfactant-based subsurface remediation) is likely to create substantial new interfacial area.

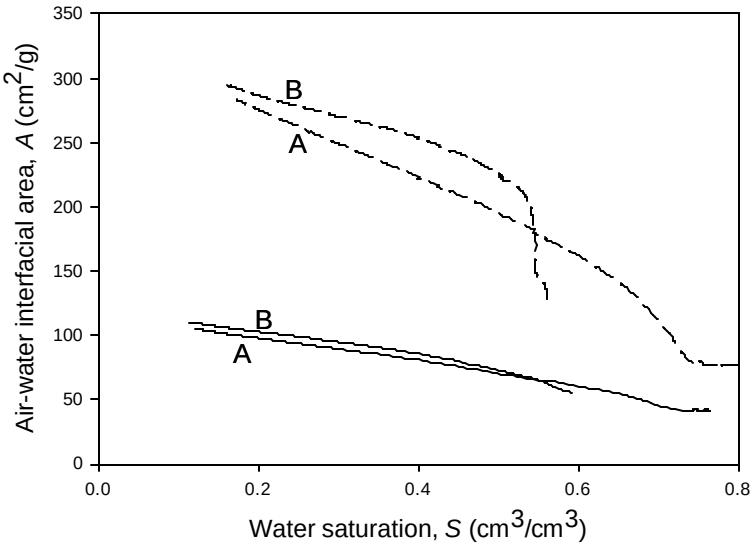


Figure 5.9. Effect of interfacial tension variations on A-S curves for secondary (A) and scanning (B) drainages. Solid lines: 5 mN/m variation; dashed lines: 25 mN/m variation.

5.5. CONCLUSIONS

Fluid-fluid interfacial area is an important factor in controlling contaminant transport and mass transfer among phases in subsurface, but experimental measurement of interfacial area as a function of saturation and wetting/drying history is difficult. The new method described here represents a technique to measure interfacial area for a full saturation range (from fully saturated to residual saturation) over multiple drainages reflecting natural wetting/drying processes, and to provide essential information which can be used in theoretical and modeling analyses of mass transfer in environmental applications. An advantage of the method is that interfacial tension variations from the method itself are relatively small, typically on the order of 5 mN/m, so measured areas are not skewed by surface-tension-induced changes in interfacial area.

Air-water interfacial areas measured for an ultra fine sand during three hysteretic drainage processes show that more air-water interface was generated in secondary and scanning drainages than in primary drainage, with the magnitude of the difference varying as a function of saturation. Results further demonstrate that, like 2D P_c-S relationship itself, the 3D P_c-S-A relationship is also hysteretic, supported by the observation that neither P_c is a unique function of S and A, nor A is a unique function of S and P_c.

In a measurement specifically designed to study the influence of surfactant-induced interfacial tension variations, approximately two times more interfacial area was observed for a 25 mN/m interfacial tension change, in comparison with a system with relatively constant interfacial tension. This result implies that when surfactant is involved in the remediation of nonaqueous phase liquid (NAPL) contamination, substantial new

NAPL-water interfacial area is likely to be formed by the surfactant solution -- a potentially beneficial result which may accelerate remediation.

Chapter 6

Conclusions

6.1. CONCLUSIONS

The work presented here experimentally examines two unsaturated phenomena of porous media that influence the transport and distribution of contaminants in subsurface. The first is dynamic effects in the response of porous media to pressure changes. Dynamic effects discussed in this work include both relative permeability effects which control the speed of unsaturated flow, and dynamic capillary effects which influence the hysteretic capillary pressure-saturation (P_c-S) relationship under dynamic conditions. The second unsaturated phenomenon studied here is the influence of hysteretic P_c-S relationships on the magnitude of interfacial area (A) between two immiscible fluids, a critical parameter controlling contaminant distribution, transport and mass transfer in unsaturated environments. For this research, an automated device was specifically designed for the rapid and simultaneous measurement of detailed hysteretic P_c-S relationships and corresponding fluid-fluid interfacial area of various porous media under static, pseudo-static or dynamic conditions.

6.1.1. *Hysteresis in Dynamic Effects and the Influence of Porous Media Properties*

In this work, relative permeability (k_{rw}) and the dynamic capillary coefficient (t) were studied parameters measuring relative permeability effects and dynamic capillary effects, respectively. A newly-developed parameter called apparent dynamic coefficient (t^*), a measure of combined dynamic effects, was measured for various porous media

ranging from sand to silt during different drying/wetting paths, including primary drainage, main imbibition, and secondary drainage. The magnitudes of k_{rw} and t were calculated from t^* with the application of Darcy's law and Brooks-Corey equations for unsaturated flow. In general, it was found that t^*, t, and k_{rw} are hysteretic along the hysteretic P_c-S relationship, and vary as a function of effective water saturation (S_e). Major findings include:

- For each drainage or imbibition process, the unsaturated flow is dominated by relative permeability effects at low saturations, and by dynamic capillary effects at high saturations.
- The apparent dynamic coefficient, t^*, is hysteretic along hysteretic P_c-S curves. As t^* increases with decreasing saturation, the highest t^* value at a given saturation was found for secondary drainage, and the lowest was found for main imbibition.
- Relative permeability was found to be hysteretic between drainage and imbibition. While the relative permeability during drainage is likely to follow the Brooks-Corey function, much higher relative permeability appears to exist during imbibition.
- The dynamic capillary coefficient, t, determined for drainages also shows a hysteretic nature. As t decreases with saturation, t values were found to be up to 20 times higher for secondary drainage than primary drainage at given saturation. The magnitude of t indirectly determined here is in the same range of literature data obtained from direct measurements.

- It was found that the intercept of the t^*-S_e curve is a good estimate of the t value at high saturation, the region where the t calculation is most reliable.

In addition, t^* and t were found to be a function of porous media properties for a given wetting/nonwetting system:

- In general, higher t^* and t values were observed for finer porous media at a particular saturation.
- It was found that the product of t (at high saturation) and saturated conductivity is a constant for different porous media, with the magnitude of the constant varying for different drainage or imbibition processes. As such, the magnitude of t values can be estimated for various porous media with known saturated conductivity.

6.1.2. *Hysteresis in the Measured Capillary Pressure-Saturation-Interfacial Area Relationships*

In this work, air-water interfacial areas (A) were measured for multiple drainages using a newly developed method, along hysteretic P_c-S curves representing natural drying/wetting processes. The measurement was conducted under a condition with relatively constant interfacial tension throughout experiments, making use of an isomerically pure anionic surfactant as interfacial tracer. Langmuir and Gibbs adsorption equations were applied in area calculations. A 3D P_c-S-A relationship established for a

fine sand using the described method shows a hysteretic nature. Several specific conclusions can be made based on this study:

- Interfacial area increases monotonically with decreasing saturation for every drainage process studied here, including primary, secondary and one scanning drainages.

- The measured interfacial areas for different porous media at a given saturation strongly depend on the grain size, with higher interfacial areas observed for finer media.

- The *A*-*S* relationship is hysteretic for different drainages studied here. At the same saturation, up to 20 cm^2/g more interfacial area was found for secondary and scanning drainages than primary drainage. And in most cases, scanning drainage has slightly higher interfacial area than secondary drainage.

- Interfacial area is not a unique function of P_c and *S*. With the same P_c and *S* values, higher interfacial area was found for secondary and scanning drainages than primary drainage.

- Capillary pressure is also not a unique function of *S* and *A*. With the same *S* and *A* values, higher P_c was observed for secondary drainage than scanning drainage.

In an interfacial area measurement specifically designed to study the influence of surfactant-induced interfacial tension variations, approximately two times more interfacial area was observed for a 25 mN/m interfacial tension change, in comparison with a system with relatively constant interfacial tension. This result implies any practical application that substantially changes the interfacial tension of an interface (e.g., surfactant-based subsurface remediation) is likely to create substantial new interfacial area.

6.2. RECOMMENDATIONS FOR FUTURE WORK

Additional related studies which could help to strengthen and widen the findings of the work presented here include:

1. Measure the P_c-S-A relationships of different porous media in different wetting/nonwetting systems along hysteretic P_c-S curves to test the applicability of the findings reported here (i.e., 3D P_c-S-A relationship is also hysteretic) to the other porous media systems including gas-liquid or liquid-liquid.

2. Modeling simulation of the observed hysteretic P_c-S-A relationships to better understand the fluid behavior and contaminant transport in unsaturated environments.

3. Since relative permeability and dynamic capillary coefficients reported here were based on indirect determination, direct experimental

measurement of dynamic capillary coefficient (t) is needed to confirm the magnitudes of reported values. Direct measurements could be conducted by modifying the P_c-S measurement device by installing tensiometers inside the pressure cell to directly measure the average phase pressures.

References:

Adamson, A. W., and A. P. Gast (1997), *Physical Chemistry of Surfaces*, 6th ed.; John-Wiley & Sons: New York,; Chapter III.

Anderson, W. G. (1987), Wettability literature survey ---- part 4: effects of wettability on capillary pressure, *J. Petrol. Technol., 39,* 1283-1300.

Anwar, A. H. M. F., M. Bettahar, and U. Matsubayashi (2000), A method for determining air-water interfacial area in variably saturated porous media, *J. Contam. Hydrol., 43,* 129-146.

Barenblatt, G. I., T. W. Patzek, and D. B. Silin (2003), The mathematical model of nonequilibrium effects in water-oil displacement, *SPE J., 8*(4), 409-416.

Bear, J. (1972), *Dynamics of Fluids in Porous Media*, Elsevier, New York.

Beliaev, A. Y. (2003), Homogenization of two-phase flows in porous media with hysteresis in the capillary relation, *Euro. J. Appl. Math., 14(1),* 61-84.

Beliaev, A. Y., and S.M. Hassanizadeh (2001), A theoretical model of hysteresis and dynamic effects in the capillary relation for two-phase flow in porous media, *Transp. Porous Media, 43,* 487-510.

Beliaev, A. Y., and R. J. Schotting (2001), Analysis of a new model for unsaturated flow in porous media including hysteresis and dynamic effects, *Comput. Geosci., 5,* 345-368.

Bohne, K., D. Radcliffe, G. Wessolek, and S. Zacharias (1999), Inverse method to estimate soil hydraulic parameters form field measurements of ponded infliltration, in *Proceedings of the International Workshop on Characterization and Measurement of the Hydraulic Properties of Unsaturated Porous Media,* Riverside, CA, Oct. 22-24, 1997. Edited by M. Th. van Genuchten, F. J. Leij, and L. Wu. Part 2, p 799-815.

Bradford, S. A., and F. J. Leij (1997), Estimating interfacial areas for multi-fluid soil systems, *J. contam. Hydrol., 27,* 83-105.

Brooks, R. H., and A. T. Corey (1966), Properties of porous media affecting fluid flow, *Proc. Am. Soc. Civ. Eng., J. Irrigation Drainage Div.* IR2, 61-68.

Brusseau, M. L., J. Popovicova, and J. A. K. Silva (1997), Characterizing gas-water interfacial and bulk-water partitioning for gas-phase transport of organic contaminanta in unsaturated porous media, *Environ. Sci.* Technol., *31,* 1645-1649.

Butters, G. L., and P. Duchateau (2002), Continuous flow method for rapid measurement of soil hydraulic properties: I. Experimental considerations, *Vadose Zone J.*, *1*, 239-251.

Cary, J. W. (1994), Estimating the surface area of fluid phase interfaces in porous media, *J. Contam. Hydrol., 15,* 243-248.

Celia, M. A., H. K. Dahle, and S. M. Hassanizadeh (2004), Dynamic effects in capillary pressure relationships for two-phase flow in porous media: insights from bundle-of-tubes models and their implications, *in* proceedings of the XV international conference on computational methods in water resources, Chapel Hill, NC., *Vol. 1,* 127-138.

Cheng, J.-T., L. J. Pyrak-Nolte, D. D. Nolte, and N. J. Giordano (2004), Linking pressure and saturation through interfacial areas in porous media, *Geophys. Res. Lett., 31*(8), L08502, doi: 10.1029/2003GL019282.

Clint, J. H. (1975), Micellization of mixed nonionic surface active agents, *J. Chem. Soc., Faraday Trans.1: Phys. Chem. Condensed Phases, 71*(6), 1327-1334.

Coleman, J. D., and A. D.Marsh (1961), An investigation of the pressure-membrane method for measuring the suction properties of soil, *J. Soil Sci., 12(2),* 343-362.

Corey, A. T., and R. H. Brooks (1975), Drainage characteristics of soils, *Soil Sci. Soc. Am. Proc., 39(2),* 251-255.

Costanza, M. S., and M. L. Brusseau (2000), Contaminant vapor adsorption at the gas-water interface in soils, *Environ. Sci. Technol., 34,* 1-11.

Costanza-Robinson, M. S., and M. L. Brusseau (2002), Air-water interfacial areas in unsaturated soils: evaluation of interfacial domains, *Water Resour. Res., 38(10),* 1195, doi: 10.1029/2001WR000738.

Culligan, K. A., D. Wildenschild, B. S. B. Christensen, W. G. Gray, M. L. Rivers, and A. F. B. Tompson (2004), Interfacial area measurements for unsaturated flow through a porous medium, *Water Resour. Res.***,** *40,* W12413, doi: 10.1029/2004WR003278.

Culligan, K. A., D. Wildenschild, B. S. B. Christensen, W. G. Gray, and M. L. Rivers (2006), Pore-scale characteristics of multiphase flow in porous media: a comparison of air-water and oil-water experiments, *Adv. Water Resour., 29,* 227-238

Cutting, C. L., and D. C. Jones (1955), Adsorption of insoluble vapours on water surfaces. Part I., *J. Chem. Soc., Abstracts,* 4067-4075.

Del Rio, O. I., and A. W. Neumann (1997), Axismmetric drop shape analysis: Computational methods for the measurement of interfacial properties from the shape and dimensions of pendant and sessile drops, *J. Colloid Interface Sci., 196,* 136-147.

Demond, A. H., F. N. Desai, and K. F. Hayes (1994), Effect of cationic surfactants on organic liquid-water capillary pressure-saturation relationships, *Water Resour. Res., 30,* 333-342.

Demond, A. H., and P. V. Roberts (1991), Effect of interfacial forces on two-phase capillary pressure-saturation relationships, *Water Resour. Res., 27,* 423-437.

Desai, F. N., A. H. Demond, and K. F. Hayes (1992), Influence of surfactant sorption on capillary pressure-saturation relationships, in *Transport and Remediation of Subsurface Contaminants: Colloidal, Interfacial, and Surfactant Phenomena,* edited by R. Knox and D. Sabatini, pp. 133-148, American Chemical Society, Washington, D. C.

Dirksen, C. (1990), Unsaturated hydraulic conductivity, in *Soil Analysis: Modern Instrumental Techniques,* 2nd ed. Edited by K. Smith and C. Mullins, Marcel Dekker, NY, p. 209-269.

Eching, S. O., and J. W. Hopmans (1993), Optimization of hydraulic functions from transient outflow and soil water pressure data, *Soil Sci. Soc. Am. J.,* 58, 687-695.

Eching, S. O., J. W. Hopmans, and O. Wendroth (1994), Unsaturated hydraulic conductivity from transient multistep outflow and soil water pressure data, *Soil Sci. Soc. Am. J.,* 57, 1167-1175.

Elrick, D. E., and D. H. Bowman (1964), Note on an improved apparatus for soil moisture flow measurements, *Soil Sci. Soc. Proc., 28,* 450-453.

Fetter, C. W. (2001), *Applied Hydrogeology,* 4th ed., 598 pp., Prentice-Hall, Upper Saddle River, NJ.

Fredlund, D. G., and H. Rahardjo (1993), *Soil Mechanics for Unsaturated Soils,* 517 pp., John Wiley & Sons, New York, NY.

Friedman G. M., and J. E. Sanders (1978), *Principles of Sedimentology,* 792 pp., John Wiley, New York, NY.

Gardner, W., O. W. Israelsen, N. E. Edlefsen, and H. Clyde (1922), The capillary potential function and its relation to irrigation practice, *Physic. Rev., Series 2,* 196.

Gielen, T., S. M. Hassanizadeh, M. A. Celia, H. K. Dahle, and A. Leijnse (2004), A pore-scale network approach to investigate dynamic effects in multiphase flow, *in* proceedings of the XV international conference on computational methods in water resources, Chapel Hill, NC., *Vol. 1*, 83-94.

Gvirtzman, H., and P. V. Roberts (1991), Pore scale spatial analysis of two immiscible fluids in porous media, *Water Resour. Res., 27*, 1165-1176.

Hari, A. C., R. A. Paruchuri, D. A. Sabatini, and T. C. G. Kibbey (2005), Effects of pH and cationic and anionic surfactants on the adsorption of pharmaceuticals to a natural aquifer material, *Environ. Sci. Technol., 39*, 2592-2598.

Hassanizadeh, A. M., and W. G. Gray (1993), Thermodynamic basis of capillary pressure in porous media, *Water Resour. Res., 29*, 3389-3405.

Hassanizadeh, A. M., M. A. Celia, and H. K. Dahle (2002), Dynamic effect in the capillary pressure-saturation relationship and its impacts on unsaturated flow, *Vadose Zone J., 1*, 38-57.

Held, R. J., and M. A. Celia (2001), Modeling support of functional relationships between capillary pressure, saturation, interfacial area and common lines, *Adv. Water Resour., 24*, 325-343.

Henry, E. J., and J. E. Smith (2003), Surfactant-induced flow phenomena in the vadose zone: a review of data and numerical modeling, *Vadose Zone J., 2*, 154-167.

Henry, E. J., J. E. Smith, and A. W. Warrick (1999), Solubility effects on surfactant-induced unsaturated flow through porous media, *J. Hydrol., 223*, 164-174.

Hoeg, S.; H. F. Scholer, and J. Warnatz (2004), Assessment of interfacial mass transfer in water-unsaturated soils during vapor extraction, *J. Contam. Hydrol., 74*, 163-195.

Hopmans, J. W, and J. Simunek (1999), Review of inverse estimation of soil hydraulic properties, in *Proceedings of the International Workshop on Characterization and Measurement of the Hydraulic Properties of Unsaturated Porous Media*, Riverside, CA, Oct. 22-24, 1997. Edited by M. Th. van Genuchten, F. J. Leij, and L. Wu. Part 2, p 643-659.

Imhoff, P. T.; P. R. Jaffé, and G. F. Pinder (1993), An experimental study of complete dissolution of a nonaqueous phase liquid in saturated porous media, *Water Resour. Res.***,** *30*, 307-320.

Jain, V.; S. Bryant, and M. Sharma (2003), Influence of wettability and saturation on liquid-liquid interfacial area in porous media, *Environ. Sci. Technol., 37*, 584-591.

Jamison, V. C. and I. F. Reed (1949), Durable asbestos tension tables, *Soil Sci., 67,* 311-318.

Jauhiainen, M., and T. Karvonen (1999), Andersson's and van Genuchten's equations for predicting the hydraulic conductivity of unsaturated soils, in *Proceedings of the International Workshop on Characterization and Measurement of the Hydraulic Properties of Unsaturated Porous Media,* Riverside, CA, Oct. 22-24, 1997. Edited by M. Th. van Genuchten, F. J. Leij, and L. Wu. Part 2, p 1061-1070.

Jones D. C., and R. H. Ottewill (1955), Adsorption of insoluble vapours on water surfaces. Part II., *J. Chem. Soc., Abstracts,* 4076-4088.

Karkare, M. V., and T. Fort (1993), Water movement in "unsaturated" porous media due to pore size and surface tension induced capillary pressure gradients, *Langmuir***,** *9,* 2398-2403.

Karkare, M. V., and T. Fort (1994), Flow in "unsaturated" porous media due to water-insoluble surfactants: role of momentum transfer from a spreading monolayer, *Langmuir***,** *10,* 3701-3704.

Karkare, M. V., and T. Fort (1996), Determination of the air-water interfacial area in wet "unsaturated" porous media, *Langmuir***,** *12,* 2041-2044.

Karkare, M. V., H. T. La, and T. Fort (1993), Criteria for effectiveness of surfactants as water-moving agents in "unsaturated" wet sand, *Langmuir***,** *9,* 1684-1690.

Kibbey, T. C. G., and K. F. Hayes (1997), Multicomponent analysis of the sorption of polydisperse ethoxylated nonionic surfactants to aquifer materials: equilibrium sorption behavior, *Environ. Sci. Technol., 31,* 1171-1177

Kim, H., M. D. Annable; and P. S. Rao (1998), Influence of air-water interfacial adsorption and gas-phase partitioning on the transport of organic chemicals in unsaturated porous media, *Environ. Sci. Technol., 32,* 1253-1259.

Kim, H. P. S. C. Rao, and M. D. Annable (1997), Determination of effective air-water interfacial area in partially saturated porous media using surfactant adsorption, *Water Resour. Res., 33,* 2705-2711.

Kim, H., P. S. C. Rao, and M. D. Annable (1999a), Consistency of the interfacial tracer technique: experimental evaluation, *J. Contam. Hydrol., 40,* 79-94.

Kim., H. P. S. C. Rao, and M. D. Annable (1999b), Gaseous tracer technique for estimating air-water interfacial areas and interface mobility, *Soil Sci. Soc. Am. J.***,** *63,* 1554-1560.

Klute, A. (1986), Water retention: laboratory methods, in *Methods of Soil Analysis, Part 1. Physical and Mineralogical Methods, 2nd Ed.,* edited by A. Klute, pp. 635-662, American Society of Agronomy, Madison, Wis.

Klute, A., and C. Dirksen (1986), Hydraulic conductivity and diffusivity: laboratory methods, in *Methods of Soil Analysis, Part 1. Physical and Mineralogical Methods, 2nd Ed.,* edited by A. Klute, pp. 687-734, American Society of Agronomy, Madison, Wis.

Kneafsey, T. J., and J. R. Hunt (2004), Non-aqueous phase liquid spreading during soil vapor extraction, *J. Contam. Hydrol., 68,* 143-164.

Kravchenko, A., and R. Zhang (1999), Estimating soil hydraulic conductivity from soil particle-size distribution, in *Proceedings of the International Workshop on Characterization and Measurement of the Hydraulic Properties of Unsaturated Porous Media,* Riverside, CA, Oct. 22-24, 1997. Edited by M. Th. van Genuchten, F. J. Leij, and L. Wu. Part 2, p 959-966.

Leamer, R. W., and B. Shaw (1941), A simple apparatus for measuring noncapillary porosity on an extensive scale, *J. Am. Soc. Agron., 33,* 1003-1008.

Leonard, R. A., and P. F. Low (1962), A self-adjusting, null-point tensiometer, *Soil. Sci. Soc. Am. Proc., 26,* 123-125.

Leverett, M. C. (1941), Capillary behavior in porous solids, *Trans. Am. Inst. Min. Metall. Eng., 142,* 152-169.

Lord, D. L., A. H. Demond, A. Salehzadeh, and K. F. Hayes (1997), Influence of organic acid solution chemistry on subsurface transport properties. 2. capillary pressure-saturation, *Environ. Sci. Technol., 31,* 2052-2058.

Manthey, S., S. M. Hassanizadeh, and R. Helmig (2005), Macro-scale dynamic effects in homogeneous and heterogeneous porous media, *Transp. Porous Media, 58,* 121-145.

Manthey, S., S. M. Hassanizadeh, O. Oung, and R. Helmig (2004), Dynamic capillary pressure effects in two-phase flow through heterogeneous porous media, *in* proceedings of the XV international conference on computational methods in water resources, Chapel Hill, NC., *Vol. 1,* 631-644.

Miller, R. D. (1951), A technique for measuring soil-moisture tensions in rapidly changing systems, *Soil Sci., 72,* 291-301.

Miller, C. T., M. M. Poirier-McNeill, and A. S. Mayer (1990), Dissolution of trapped nonaqueous phase liquids: mass transfer characteristics, *Water Resour. Res., 26,* 2783-2796.

Mohammad, O. I., and T. C. G. Kibbey (2005), Dissolution-induced contact angle modification in dense nonaqueous phase liquid/water systems, *Environ. Sci. Technol., 39,* 1698-1706.

Morrow, N. R. (1976), Capillary pressure correlations for uniformly wetted porous media, *J. Can. Petrol. Technol., 15* (4), 49-69.

Morrow, N. R., and C. C. Harris (1965), Capillary equilibrium in porous materials, *Soc. Petrol. Engr. J., 5,* 15-24.

Muccino, J. C., W. G. Gary, and L. A. Ferrand (1998), Toward an improved understanding of multiphase flow in porous media, *Rev. Geophy.,* 36, 401-422.

Nimmo, J. R. (1999), Predicting soil-water retention and hydraulic conductivity from textural and structural information, in *Proceedings of the International Workshop on Characterization and Measurement of the Hydraulic Properties of Unsaturated Porous Media,* Riverside, CA, Oct. 22-24, 1997. Edited by M. Th. van Genuchten, F. J. Leij, and L. Wu. Part 2, p 923-930.

O'Carroll, D. M., T. J. Phelan, and L. M. Abriola (2005), Exploring dynamic effects n capillary pressure in multistep outflow experiments, *Water Resour. Res., 41*(11), W11419, doi: 10.1029/2005WR004010.

Oliviera, I. B., A. H. Demond, and A. Salehzadeh (1996), Packing of sands for the production of homogeneous porous media, *Soil Sci. Am. J., 60,* 49-53.

Or, D., and M. Tuller (1999), Liquid retention and interfacial area in variably saturated porous media: upscaling from single-pore to sample-scale model, *Water Resour. Res., 35,* 3591-3605.

Oung, O., S. M. Hassanizadeh, and A. Bezuijen (2005), Two-phase flow experiments in a geocentrifuge and the significance of dynamic capillary pressure effect, *J. Porous Media,* 8(3), 247-257.

Peng, S., and M. L. Brusseau (2005), Impact of soil texture on air-water interfacial areas in unsaturated sandy porous media, *Water Resour. Res., 41,* W03021, doi:10.1029/2004WR003233.

Perroux, K. M., P. A. C. Raats, and D. E. Smiles (1982), Wetting moisture characteristic curves derived from constant-rate infiltration into thin soil samples, *Soil Sci. Soc. Am. J., 46,* 231-234.

Plagge, R, P. Haupl, and M. Renger (1999), Transient effects on the hydraulic properties of porous media, in *Proceedings of the International Workshop on Characterization and Measurement of the Hydraulic Properties of Unsaturated*

Porous Media, Riverside, CA, Oct. 22-24, 1997. Edited by M. Th. van Genuchten, F. J. Leij, and L. Wu. Part 2, p 905-912.

Powers, A. E., and M. E. Tamblin (1995), Wettability of porous media after exposure to synthetic gasolines, *J. Contam. Hydrol., 19*, 105-125.

Puri, A. N. (1949), *Soil, Their Physics and Chemistry*, 550 pp., Reinhold Publishing Corp., New York.

Reeves, P. C., and M. A. Celia (1996), A functional relationship between capillary pressure, saturation, and interfacial area as revealed by a pore-scale network model, *Water Resour. Res., 32*, 2345-2358.

Reginato, R. J., and C. H. M. van Bavel (1962), Pressure cell for soil cores, *Soil Sci. Soc. Am. J., 26*(1), 1-3.

Reitemeier, R. F., and L. A. Richards (1944), Reliability of the pressure-membrane method for extraction of soil solution, *Soil Sci., 57*, 119-135.

Richards, L. A. (1928), The usefulness of capillary potential to soil-moisture and plant investigators, *J. Agric. Res., 37*, 719-742.

Richards, L. A (1941), A pressure-membrane extraction apparatus for soil solution, *Soil Sci., 51*, 377-386.

Richards, L. A., and M. Fireman (1943), Pressure-plate apparatus for measuring moisture sorption and transmission by soils, *Soil Sci., 56*, 395-404.

Richards, L. A., and L. R. Weaver (1944), Moisture retention by some irrigated soils as related to soil-moisture tension, *J. Agric. Res., 69 (6)*, 215-235.

Rogers, J. S., and A. Klute (1971), The hydraulic conductivity-water content relationship during nonsteady flow through a sand column, *Soil Sci. Soc. Am. Proc., 35*, 695-700.

Rosen, M. J. (1988), *Surfactants and Interfacial Phenomena*, 2nd ed.; John-Wiley & Sons: New York, Chapter 2.

Rubin, H., K. Rathfelder, L. M. Abriola, M. Spiller, and J. Kongeter (2004), Using continuum approach ot quantify the remediation of nonaqueous phase liquid contaminated fractured permeable formations, *J. Environ. Eng., 130*, 1345-1356.

Salehzadeh, A., and A. H. Demond (1999), Pressure cell for measuring capillary pressure relationships of contaminated sands, *J. Environ. Eng., 125*, 385-388.

Saripalli, K. P., H. Kim, P. S. C. Rao, and M. D. Annable (1997), Measurement of specific fluid-fluid interfacial areas of immiscible fluids in porous media, *Environ. Sci. Technol., 31,* 932-936.

Saripalli, K. P., P. S. C. Rao, and M. D. Annable (1998), Determination of specific NAPL-water interfacial areas of residual NAPLs in porous media using the interfacial tracers technique, *J. Contam. Hydrol., 30,* 375-391.

Schaefer, C. E., D. A. DiCarlo, and M. J. Blunt (2000), Experimental measurement of air-water interfacial area during gravity drainage and secondary imbibition in porous media, *Water Resour. Res., 36,* 885-890.

Schultze B., O. Ippisch, B. Huwe, and W. Duiner (1999), Dynamic nonequilibrium during unsaturated water flow, in *Proceedings of the International Workshop on Characterization and Measurement of the Hydraulic Properties of Unsaturated Porous Media,* Riverside, CA, Oct. 22-24, 1997. Edited by M. Th. van Genuchten, F. J. Leij, and L. Wu. Part 2, p 877-892.

She, H. Y., and B. E. Sleep (1998), The effect of temperature on capillary pressure-saturation relationships for air-water and perchloroethylene-water systems, *Water Resour. Res., 34,* 2587-2597.

Silverstein, D. L., and T. Fort (1997), Studies in air-water interfacial area for wet unsaturated particulate porous media systems, *Langmuir, 13,* 4758-4761.

Silverstein, D. L., and T. Fort (2000), Prediction of air-water interfacial area in wet unsaturated porous media, *Langmuir, 16,* 829-834.

Sim, Y, and C. V. Chrysikopoulos (2000), Virus transport in unsaturated porous media, *Water Resour. Res., 36,* 173-179.

Simunek, J., O. Wendroth, and M. Th. van Genuchten (1999), Soil hydraulic properties from laboratory evaporation experiments by parameter estimation, in *Proceedings of the International Workshop on Characterization and Measurement of the Hydraulic Properties of Unsaturated Porous Media,* Riverside, CA, Oct. 22-24, 1997. Edited by M. Th. van Genuchten, F. J. Leij, and L. Wu. Part 2, p 713-724.

Smiles, D. E., G. Vachaud, and M. Vauclin (1971), A test of the uniqueness of the soil moisture characteristic during transient nonhysteretic flow of water in a rigid soil, *Soil Sci. Soc. Am. Proc., 35,* 534-539.

Stauffer, F. (1978), Time dependence of the relations between capillary pressure, water content and conductivity during drainage of porous media, *IAHR Symp. On Scale Effects in Porous Media,* Thessaloniki, Greece, Aug. 29 to Sept. 1, 1978. IAHR, Madrid, Spain.

Stumm, W., and J. J. Morgan (1995), *Aquatic Chemistry: Chemical Equilibria and Rates in Natural Waters*, 3rd ed.; John-Wiley & Sons: New York. Chapter 3.

Su, C., and R. H. Brooks (1980), Water retention measurement for soils, *J. Irrig. Drain. Div., Proc. Am. Soc. Civ. Engr., 106,* 105-112.

Timlin, D. J., L. R. Ahuja, Ya. A. Pachepsky, R.D. Williams, D. Gimenez, and W. J. Rawls (1999), Brooks-Corey pore size distribution index to estimate saturated conductivity from effective porosity, in *Proceedings of the International Workshop on Characterization and Measurement of the Hydraulic Properties of Unsaturated Porous Media,* Riverside, CA, Oct. 22-24, 1997. Edited by M. Th. van Genuchten, F. J. Leij, and L. Wu. Part 2, p 1029-1036.

Tanner, C. B., and D. E. Elrick (1958), Volumetric porous (pressure) plate apparatus for moisture hysteresis measurements, *Soil Sci. Soc. Am. Proc., 22,* 575-576.

Topp, G. C., A. Klute, and D. B. Peters (1967), Comparison of water content-pressure head data obtained by equilibrium, steady-state, and unsteady-state methods, *Soil Sci. Soc. Am. Proc., 31,* 312-314.

Tuller, M., D. Or, and L. M. Dudley (1999), Adsorption and capillary condensation in porous media: liquid retention and interfacial configurations in angular pores, *Water Resour. Res., 35,* 1949-1964.

Vachaud, G., and J.-L. Thony (1971), Hysteresis during infiltration and redistribution in a soil column at different initial water contents, *Water Resour. Res., 7*(1), 111-127.

Vachaud, G., M. Vauclin, and M. Wakil (1972), A study of the uniqueness of the soil moisture characteristic during desorption by vertical drainage, *Soil Sci. Soc. Am. Proc., 36,* 531-532.

van Genuchten, M. Th. (1980), A closed-form equation for predicting the hydraulic conductivity of unsaturated soils, *Soil Sci. Soc. Am. J., 44,* 892-898.

Vogel, T., M. Nakhaei, and M. Cislerova (1999), Description of soil hydraulic properties near saturation form the point of view of inverse modeling, in *Proceedings of the International Workshop on Characterization and Measurement of the Hydraulic Properties of Unsaturated Porous Media,* Riverside, CA, Oct. 22-24, 1997. Edited by M. Th. van Genuchten, F. J. Leij, and L. Wu. Part 2, p 693-703.

Wan, J., and J. L. Wilson (1994), Colloid transport in unsaturated porous media, *Water Resour. Res., 30,* 857-864.

White, N. F., D. K. Sunada, H. R. Duke, and A. T. Corey (1972), Boundary effects in desaturation of porous media, *Soil Sci., 113 (1),* 7-12.

Wildenschild, D., J. W. Hopmans, and J. Simunek (2001), Flow rate dependence of soil hydraulic characteristics, *Soil Sci. Soc. Am. J., 65,* 35-48.

Wildenschild, D., K. H. Jensen, K. J. Hollenbeck, T. H. Illangasekare, D. Znidarcic, T. Sonnenbor, and M. B. Butts (1997), A two-stage procedure for determining unsaturated hydraulic characteristics using a syringe pump and outflow observations, *Soil Sci. Soc. Am. J., 61,* 347-359.

Woodruff, C. M. (1940), Soil moisture and plant growth in relation to pF, *Soil Sci. Soc. Am. Proc., 5,* 38-41.